

## REPORT DOCUMENTATION PAGE

AD-A212 182

ELECTE

SEP 11 1989

SCHEDULE

1b. RESTRICTIVE MARKING

3. DISTRIBUTION / AVAILABILITY OF REPORT  
Approved for Public Release;  
Distribution Unlimited

4. PERFORMING ORGANIZATION REPORT NUMBER(S)

5. MONITORING ORGANIZATION REPORT NUMBER(S)

AFOSR-TR. 89-1229

6a. NAME OF PERFORMING ORGANIZATION

Rensselaer Polytechnic  
Institute6b. OFFICE SYMBOL  
(if applicable)

N/A

7a. NAME OF MONITORING ORGANIZATION

AFOSR/NA

6c. ADDRESS (City, State, and ZIP Code)

Department of Civil Engineering  
R.P.I.  
Troy, NY 12180-3590

7b. ADDRESS (City, State, and ZIP Code)

Bldg 410  
Bolling AFB, DC 20332-64488a. NAME OF FUNDING / SPONSORING  
ORGANIZATION

AFOSR

8b. OFFICE SYMBOL  
(if applicable)

N/A

9. PROCUREMENT INSTRUMENT IDENTIFICATION NUMBER

AFOSR- 86-0135

8c. ADDRESS (City, State, and ZIP Code)

Bldg. 410  
Bolling AFB, DC 20332-6448

10. SOURCE OF FUNDING NUMBERS

PROGRAM ELEMENT NO.	PROJECT NO.	TASK NO.	WORK UNIT ACCESSION NO.
6.1102F	2302	C1	

11. TITLE (Include Security Classification) (U)

Micromechanical Behavior and Modelling of Granular ~~Media~~ SOIL

12. PERSONAL AUTHOR(S)

Emmanuel Petrakis and Ricardo Dobry

13a. TYPE OF REPORT  
Final13b. TIME COVERED  
FROM 86/05/06 TO 89/05/0514. DATE OF REPORT (Year, Month, Day)  
July 198915. PAGE COUNT  
156

16. SUPPLEMENTARY NOTATION

→ The goal of this study was to develop

17. COSATI CODES

FIELD	GROUP	SUB-GROUP

18. SUBJECT TERMS (Continue on reverse if necessary and identify by block number)

Self-Consistent Methods	Contact Mechanics
Granular Media	Arrays of Spheres
Soil Mechanics	Numerical Simulations
Constitutive Relations	Hollow-Cylinder Experiments

19. ABSTRACT (Continue on reverse if necessary and identify by block number)

A 3-year (1986-89) micromechanical research at Rensselaer Polytechnic Institute (RPI) on the behavior and modelling of granular media is summarized. The final objective is to develop a constitutive law for granular soil based on the particulate nature of the material.

This is accomplished by a systematic, mostly analytical approach to the problem, starting from the response of the contact between two elastic rough spheres subjected to arbitrary normal and tangential forces, and continuing with the response of regular and random arrays of spheres. The following tasks were completed: a) study and compilation of the differential stress-strain relationships of several regular arrays of identical quartz spheres; b) use of the Self Consistent and Nonlinear Finite Element methods to calculate the small strain, monotonic and cyclic stress-strain behavior of random/regular arrays of identical quartz spheres loaded isotropically and anisotropically, including wave velocity predictions; and c) use of Nonlinear Distinct Element simulations of two-dimensional random arrays of quartz.

20. DISTRIBUTION / AVAILABILITY OF ABSTRACT

☒ UNCLASSIFIED/UNLIMITED ☐ SAME AS RPT. ☐ DTIC USERS

21. ABSTRACT SECURITY CLASSIFICATION

UNCLASSIFIED

22a. NAME OF RESPONSIBLE INDIVIDUAL

Major Steven C. Boyce

22b. TELEPHONE (Include Area Code)

(202) 767-6963

22c. OFFICE SYMBOL

AFOSR/NA

UNCLASSIFIED

spheres to determine their small and large strain response, including the initial position and subsequent translation and distortion of yield surfaces. The main features of the procedure

Throughout the research, comparisons were made between analytical predictions and experimental measurements on sands and other granular media reported in the literature. In addition, several computer controlled, hollow-cylinder, monotonic and cyclic axial-torsional tests were conducted on glass bead specimens, along stress paths similar to those used in the Distinct Element simulations, to verify and supplement the results of the calculations.

Finally, a constitutive law for granular media is proposed and its main features are discussed. The law is basically the stress-strain equivalent of the force-deformation model for the contact between two spheres, developed at RPI, enhanced to incorporate dilation and the distortion of yield surfaces due to prestrain which has been observed in granular media. The proposed stress-strain law includes an infinite number of yield surfaces of conical shape initially parallel to each other, as well as modified normality and kinematic strain hardening rules.

(ADC)

**AFOSR-TR. 89-1229**

**MICROMECHANICAL BEHAVIOR  
AND MODELLING OF GRANULAR SOIL**

by

**Emmanuel Petrakis and Ricardo Dobry**

Prepared under Grant No. AFOSR-86-0135

United States Air Force  
Office of Scientific Research  
Bolling Air Force Base

Department of Civil Engineering  
Rensselaer Polytechnic Institute  
Troy, NY 12180-3590

July 1989

AFOSR-TR-89-1229 (AFSC)  
MICROMECHANICAL BEHAVIOR  
AND MODELLING OF GRANULAR SOIL  
EMMANUEL PETRAKIS AND RICARDO DOBRY  
JULY 1989  
CHIEF, TECHNICAL INFORMATION DIVISION

## TABLE OF CONTENTS

	<u>Page</u>
ABSTRACT . . . . .	i
LIST OF TABLES . . . . .	iii
LIST OF FIGURES . . . . .	iv
LIST OF SYMBOLS . . . . .	x
ACKNOWLEDGEMENTS . . . . .	xvi
 1. INTRODUCTION . . . . .	 1
1.1 Brief Review of Constitutive Relations in Soils . . . . .	2
1.2 Micromechanical Interpretation of the Deformation Mechanism in Polycrystalline Aggregates. . . . .	 7
1.3 Micromechanical Behavior of Granular Soil . . . . .	10
 2. THE MICROMECHANICAL APPROACH . . . . .	 13
2.1 Problem of Contact Between two Elastic Rough Spheres . . . . .	13
2.1.1 Verification of the Model . . . . .	17
2.2 Differential Stress-Strain Relationships for Regular Arrays of Spheres. . . . .	 18
2.3 The Self Consistent Method . . . . .	24
2.4 A Model of a Random Array of Equal Spheres . . . . .	28
2.5 Application of the Self Consistent Method to Uniform Rounded Sand . . . . .	 32
2.6 A Two-Dimensional Numerical Model of Granular Soil at Small Strains . . . . .	 35
2.6.1 Nonlinear Finite Element Simulations . . . . .	36

	<u>Page</u>
2.6.2 Monotonic Finite Element Loading Simulations . . . . .	38
2.6.3 Cyclic Finite Element Loading Simulations . . . . .	40
2.6.4 Computation of Dynamic Properties and Wave Propagation Velocities . . . . .	41
2.7 Two-Dimensional Nonlinear Distinct Element Simulations . . . . .	43
2.7.1 Small Strain Moduli of Isotropically Compressed Random Arrays of Equal Spheres . . . . .	45
2.7.2 Small Strain Moduli of Anisotropically Compressed Random Arrays. . . . .	47
3. EXPERIMENTAL STUDY . . . . .	53
3.1 Laboratory Equipment . . . . .	54
3.2 Specimen Preparation . . . . .	56
3.3 Testing Program . . . . .	57
3.4 Experimentally Obtained Yield Surfaces . . . . .	59
4. NUMERICAL SIMULATIONS . . . . .	64
5. PROPOSED CONSTITUTIVE LAW FOR GRANULAR MEDIA . . . . .	67
6. CONCLUSIONS . . . . .	75
REFERENCES . . . . .	79
TABLES	
FIGURES	



Accession For	
NTIS ADRI	<input checked="" type="checkbox"/>
DTIC TAB	<input type="checkbox"/>
Unannounced	<input type="checkbox"/>
Justification	
For	
Distribution/	
Availability Codes	
Avail and/or	
Dist.	Special
A-1	

## ABSTRACT

A 3-year (1986-89) micromechanical research at Rensselaer Polytechnic Institute (RPI) on the behavior and modelling of granular media is summarized. The final objective is to develop a constitutive law for granular soil based on the particulate nature of the material.

This is accomplished by a systematic, mostly analytical approach to the problem, starting from the response of the contact between two elastic rough spheres subjected to arbitrary normal and tangential forces, and continuing with the response of regular and random arrays of spheres. The following tasks were completed: a) study and compilation of the differential stress-strain relationships of several regular arrays of identical quartz spheres; b) use of the Self Consistent and Nonlinear Finite Element methods to calculate the small strain, monotonic and cyclic stress-strain behavior of random/regular arrays of identical quartz spheres loaded isotropically and anisotropically, including wave velocity predictions; and c) use of Nonlinear Distinct Element simulations of two-dimensional random arrays of quartz spheres to determine their small and large strain response, including the initial position and subsequent translation and distortion of yield surfaces.

Throughout the research, comparisons were made between analytical predictions and experimental measurements on sands and other granular media reported in the literature. In addition, several computer controlled, hollow-cylinder, monotonic and cyclic axial-torsional tests were conducted on glass bead specimens, along stress paths similar to those used in the Distinct Element simulations, to verify and supplement the results of the calculations.

Finally, a constitutive law for granular media is proposed and its main features are discussed. The law is basically the stress-strain equivalent of the force-deformation model for the contact between two spheres developed at RPI, enhanced to incorporate dilation and the distortion of yield surfaces due to prestrain which has been observed in granular media. The proposed stress-strain law includes an infinite number of yield surfaces of conical shape initial parallel to each other, as well as modified normality and kinematic strain hardening rules.

## LIST OF TABLES

- Table 1: AFOSR Micromechanical Research at RPI.
- Table 2: RPI Computer Program CONBAL--2.
- Table 3: Properties of Glass Beads.
- Table 4: Summary of Monotonic Radial Shear Tests on Glass Bead Specimens.
- Table 5: Summary of Reversible Tests on Glass Bead Specimens.



## LIST OF FIGURES

- Figure 1.      Effect of stress induced anisotropy on compressional wave velocity for triaxial confinement (Kopperman et al. 1982).
- Figure 2.      Small Strain Shear Modulus,  $G_{max}$ , versus Cycles of Shear Prestrain – Hollow Cylindrical Samples (Drnevich 1967).
- Figure 3.      Experimentally obtained yield surface of sand from cubical triaxial experiments (Peters 1988).
- Figure 4.      The repeating six crystal aggregate in the infinite plane (angle of sliding shown in each crystal) (a), yield loci of the aggregate at different stages of tensile loading with an observed vertex (b), (Lin and Ito 1965).
- Figure 5.      Loading paths for (a) initial, and (b) subsequent yield surfaces (Phillips 1968).
- Figure 6.      Experimentally obtained initial and subsequent yield surfaces for aluminum at 70°F temperature (Phillips and Tang 1972).
- Figure 7.      Simple cubic array of spheres.
- Figure 8a.      Elastic Spheres Under Normal and Tangential Loads.
- Figure 8b.      Tangential Force–Displacement Relation for  $N$  Constant,  $T$  increasing (Dobry et al. 1982).
- Figure 9.      Contact Force Space and Conical Yield Surfaces, Elastic–Plastic Incremental Solution of Mindlin's Problem (Seridi and Dobry 1984).
- Figure 10.      Force–deformation Behavior of Two Elastic Rough Spheres in Contact: Analytical Solution for Oscillating Oblique Forces with (a)  $dT/dN > f$  and (b)  $dT/dN < f$ ; (c)  $N$  Increasing,  $T$  Increasing; (d)  $N$  Decreasing,  $T$  Increasing; (e)  $N$  Increasing,  $T$  Decreasing; (f)  $N$  Decreasing,  $T$  Decreasing; (Mindlin and Deresiewicz 1953).
- Figure 11.      Numerical Simulation of the Force–Deformation Behavior for Two Equal, Elastic, Rough Spheres in Contact: Load–Displacement Relation for an Oscillating Oblique Force with  $dT/dN > f$ .
- Figure 12.      Numerical Simulation of the Force–Deformation Behavior for Two Equal, Elastic, Rough Spheres in Contact: Load–Displacement Relation for an Oscillating Oblique Force with  $dT/dN < f$ .

- Figure 13. Numerical Simulation of the Force-Deformation Behavior for Two Equal, Elastic, Rough Spheres in Contact: Load-Displacement Relation for the Case in which  $N$  Increases and  $T$  Increases.
- Figure 14. Numerical Simulation of the Force-Deformation Behavior for Two Equal, Elastic, Rough Spheres in Contact: Load-Displacement Relation for the Case in which  $N$  Decreases and  $T$  Increases.
- Figure 15. Numerical Simulation of the Force-Deformation Behavior for Two Equal, Elastic, Rough Spheres in Contact: Load-Displacement Relation for the Case in which  $N$  Increases and  $T$  Decreases.
- Figure 16. Numerical Simulation of the Force-Deformation Behavior for Two Equal, Elastic, Rough Spheres in Contact: Load-Displacement Relation for the Case in which  $N$  Decreases and  $T$  Decreases.
- Figure 17. Three Regular Arrays of Equal Spheres.
- Figure 18. Small Strain Modulus,  $G_{\max}$ , versus Coordination Number (= number of contacts per sphere) for Regular Cubic Arrays of Quartz Spheres.
- Figure 19. Shear Wave Velocity versus Void Ratio: Comparison between Predictions from Regular Cubic Arrays of Quartz Spheres and Measurements in Quartz Sand.
- Figure 20. Rod Wave Velocity Measurements in Regular Dense Array of Steel Spheres Loaded Isotropically (Duffy and Mindlin 1957).
- Figure 21. (a) Cut-Away Artistic View of a Space Filling Configuration of Voronoi Polyhedra Containing Regular Arrays of Spheres (Finney 1983) and (b) Random Two-Dimensional Packing of Equal Sized Spherical Steel Balls (Shahinpoor and Shahrpass 1982).
- Figure 22. Small Strain Shear Modulus,  $G_{\max}$ , versus Isotropic Confining Pressure: Analytical and Experimental Results for (a)  $e = 0.46$ , (b)  $e = 0.54$  and (c)  $e = 0.58$ .
- Figure 23. Isotropic Confining Pressure versus Volumetric Strain: Analytical and Experimental Results for  $e = 0.54$ .
- Figure 24. (a) Small Strain Shear Modulus,  $G_{\max}$ , and (b) Void Ratio, versus Number of Cycles of Prestrain - Solid Cylindrical Samples (Song and Stokoe 1987).

- Figure 25. Shear Modulus,  $G_{\max}$ , versus Coordination Number for: (a) Regular Arrays and (b) Random Arrays of a Given Porosity by the Self-Consistent Method and the Analytical Expressions of Walton (1987). All Spheres have been Assigned the Properties of Quartz.
- Figure 26. Stress State on a Simple Cubic Array of Identical Spheres.
- Figure 27. Stress-Strain Behavior, (c), of a simple Cubic Array of Quartz Spheres Subjected to Biaxial Stress,  $\sigma_{11} = 161$ ,  $\sigma_{22} = 200$  KPa, Followed by Pure Shear,  $\sigma_{12}$ , to failure. (a) and (b) Portray the Corresponding Force-Deformation Behavior of the "weak" and "strong" contact, respectively.
- Figure 28. 16 and 64 Element Media Used in the Simulations.
- Figure 29. (a) Orientation of the Applied Principal Stresses During Pure Shear Loading with Mean Stress Constant,  $\sigma_m^0 = 0.5(\sigma_1^0 + \sigma_2^0) = \text{constant}$ , and (b) orientation of an element.
- Figure 30. Difference in Applied Principal Stresses,  $\sigma_1^0 - \sigma_2^0$ , versus Shear Strain,  $\gamma = \epsilon_1 - \epsilon_2$ , Calculated for all Media (16 and 64 elements), and for Values of  $\alpha = 0^\circ, 22.5^\circ, 45^\circ, 67.5^\circ$ , and  $90^\circ$  (MX = medium X, AYY = inclination of  $\sigma_1$  is YY degrees).
- Figure 31. Medium 1: Stress-Strain Behavior for Hydrostatic Compression Loading Starting from  $\sigma_0^0 = 300$  KPa.
- Figure 32. Medium 1: Stress-Strain Behavior for Cyclic Isotropic Loading,  $\sigma_0^0 \pm \Delta\sigma_0^0$ , with  $\sigma_0^0 = 300$  KPa and  $\Delta\sigma_0^0 = 200$  KPa.
- Figure 33. Medium 1: Stress-Strain Behavior for Cyclic Pure Shear Loading Following Isotropic Compression,  $\sigma_0^0 = 100$  KPa. (a)  $\gamma_c = 40$  KPa and, (b)  $\gamma_c = 43$  KPa.
- Figure 34. Normalized Shear Modulus,  $G/G_{\max}$ , (a), and Damping ratio  $\xi$ , (b), versus Shear Strain,  $\gamma$ . Comparison Between Values Measured in Sand, the Simulated Aggregate and Simple Cubic Array in Pure Shear.
- Figure 35. Normalized Constrained Moduli,  $D_{11}^{(K)}/D_{11}^{(I)}$  versus Stress Ratio,  $K = \sigma_1^0/\sigma_2^0$ . Comparison Between Analytical and Experimental Results (a) in the Direction of  $\sigma_1^0$ , and (b) in the Direction of  $\sigma_2^0$  ( $\sigma_2^0$  is kept constant).

- Figure 36. 2-D Random Array of 477 Equal, Elastic, Rough, Quartz Spheres Subjected to Isotropic Compression,  $\sigma = 91$  KPa. Note that this Figure Represents the "Window" with the Representative Random Pattern.
- Figure 37. Statistical Information Regarding the isotropic Compression at  $\sigma_0 = 91$  KPa of the 477-sphere medium of Figure 36.
- Figure 38. Shear Modulus,  $G_{max}$ , vs Coordination Number for : i) Two Random Arrays of 477 Equal Spheres, ii) Regular Arrays, and iii) Random Arrays of a given porosity by the Self Consistent Method and the analytical expressions of Walton (1987).
- Figure 39. 2-D Random Array of 531 Elastic, Quartz Spheres of Two Radii ( $R_1/R_2 = 1.5$ ) Subjected to Isotropic Compression  $\sigma_0 = 132$  KPa.
- Figure 40. Statistical Information for the isotropic loading of Fig. 39.
- Figure 41. 2-D Random Array of 531 Elastic, Quartz Spheres of Two Radii ( $R_1/R_2 = 1.5$ ) Subjected to Biaxial Compression Loading.
- Figure 42. Statistical information for the biaxial compression loading in Fig. 41.
- Figure 43. Normalized constrained moduli,  $D_{11}^{(K)} / D_{11}^{(1)}$ , vs stress ratio,  $K = \sigma_1 / \sigma_2$ , for all Distinct Element, Finite Element and Experimental results: (a) in the direction of  $\sigma_1$  and (b) in the direction of  $\sigma_2$  ( $\sigma_2$  is kept constant).
- Figure 44. Normalized constrained moduli,  $D_{11}^{(K)} / D_{11}^{(1)}$  versus stress ratio,  $K = \sigma_{11} / \sigma_0$ , for the case of biaxial compression-extension loading with constant mean stress,  $\sigma_0 = 91$  KPa.
- Figure 45. The RPI Soil Mechanics Laboratory MTS Servohydraulic Axial/Torsional and Computer control System Configuration.
- Figure 46. Sketch of Hollow Cylindrical Specimen Used in this Study.
- Figure 47. Grain Size Distribution Curve for Mixture of Glass Beads Used in this Study.
- Figure 48.  $\tau_{oct}/\sigma_m$  Ratio versus Octahedral Shear Strain  $\gamma_{oct}$  Curves from Monotonic Radial Shear Tests ( $\theta = 0^\circ, 15^\circ, 30^\circ$ ) on assemblies of different sizes of spherical particles consolidated at  $\sigma_m \approx 140$  KPa.

- Figure 49. Volumetric Strain versus Octahedral Shear Strain for Monotonic Radial Shear Tests ( $\theta = 0^\circ, 30^\circ, \text{ and } 60^\circ$ ) on Assemblies of Different Sizes of Spheres. ( $\sigma_m \approx 140 \text{ KPa}$ ).
- Figure 50.  $q/p$  Ratio versus Maximum Shear Strain for Monotonic Radial Shear Tests Having  $\theta = 0^\circ$ .
- Figure 51. Volumetric Strain versus Octahedral Shear Strain from Monotonic Radial Shear Tests ( $\theta = 0^\circ$ ) on Mixtures of Different Sizes of Glass Beads Consolidated at Different Confining Stresses.
- Figure 52. Octahedral Stress versus Volumetric Strain for Monotonic Radial Shear Tests on Assemblies of Different Sizes of Spherical Particles.
- Figure 53. Sequences of Loading for the Determination of the "initial" and "subsequent" Yield Surfaces.
- Figure 54. Flowchart of the program controlling the experiments.
- Figure 55. Experimentally Obtained Initial and Subsequent Yield Surfaces in Glass Beads ( $\gamma_{oct} = 0.1\%$ ).
- Figure 56. Experimentally Obtained Initial and Subsequent Yield Surfaces in Glass Beads ( $\gamma_{oct} = 0.05\%$ ).
- Figure 57. Stress Paths from Monotonic Radial Shear Tests on Glass Beads Plotted on  $p$ - $q$  Diagram.
- Figure 58. Initial and Subsequent yield surfaces of the 531-Sphere Medium in the  $\tau_{vh} \ 1/2 (\sigma_v - \sigma_h)$  Space calculated Using Distinct Element Program CONBAL-2. Yield Surfaces Defined as the Set of all Points with  $\gamma_{oct} = 0.05\%$ .
- Figure 59. Experimentally Obtained Yield Loci for Engineering Materials after Shear Prestrain (a) 1100-0 Aluminum, (b) Overaged 2024-T7 Aluminum Alloy (Helling et al. 1986), (c) 70:30 Brass, and (d) Textured Magnesium (Kelley and Hosford, 1968).
- Figure 60. Initial and Subsequent Yield Surfaces of the 531-Sphere Medium in the  $\tau_{vh} \ 1/2 (\sigma_v - \sigma_h)$  Space calculated Using Distinct Element Program CONBAL-2. Yield Surfaces Defined as the Locus of all Points with  $\gamma_{oct} = 0.05\%$ .
- Figure 61. Conical Yield Surfaces and Current  $\pi$ -plane for Constitutive Law of Granular Soil of Eqs. 1-7. Position of Yield Cones Correspond to Loading from O to A followed by Stress increment AB. Point B is on the  $\pi$ -plane. The Value of  $p$  at the Apex of Any Cone (e.g., A, B) is  $p_i$ .

- Figure 62. Schematic Representation of (a) Translation and (b) Distortion of a Yield Surface (Yen 1979).
- Figure 63. Predicted and Measured Yield Surfaces in Aluminum (Yen and Eisenberg 1987).
- Figure 64. Yield Surface in principal Stress Space. Note the Rotation of the Surface Around its Apex (Prevost 1985).
- Figure 65. Proposed Modification of the Hardening Rule to Allow Limited Rotation Around the Yield Surface Apex in Order to Account for Dilation.

## LIST OF SYMBOLS

### Greek Letters

$\alpha$ :	normal displacement between the centers of two spheres
$\alpha^*$ :	constant; value of the Eshelby S-tensor
$\alpha_{ij}$ :	location of the center the yield surface
$\beta^*$ :	constant; value of the Eshelby S-tensor
$\bar{\gamma}$ :	average macroscopic engineering shear strain
$\bar{\gamma}_i$ :	average shear strain experienced by constituent $i$ ( $i = 1, N$ )
$\gamma_{ij}$ :	engineering shear strain
$\gamma_{oct}$ :	octahedral engineering shear strain
$\gamma_t$ :	threshold (engineering) shear strain
$\gamma_{\theta x}$ :	engineering shear strain amplitude in torsional resonant column test
$\delta_x$ :	tangential displacement component in the x-direction
$\delta_y$ :	tangential displacement component in the y-direction
$\delta_{kl}$ :	Kronecker delta
$\epsilon_{ij}^e$ :	elastic strain tensor
$\epsilon_{ij}^p$ :	plastic strain tensor
$\bar{\epsilon}_v$ :	average macroscopic volumetric strain
$\bar{\epsilon}_{vi}$ :	average volumetric strain in constituent $i$ ( $i = 1, N$ )
$\epsilon_i$ :	principal strain ( $i=1,3$ )
$\eta$ :	stress ratio
$\bar{\eta}$ :	material parameter

$\theta$ :	angle of shear direction
$\lambda$ :	scalar defining the magnitude of the hardening mechanism
$\lambda^*$ :	Lame constant of the macroscopic medium
$d\lambda$ :	proportionality constant
$\mu^*$ :	Lame constant (shear modulus) of the macroscopic medium ( $\mu^* = G^*$ )
$\mu$ :	scalar defining the magnitude of the hardening mechanism
$\nu_s$ :	Poisson's Ratio of the material of the spheres
$\nu^*$ :	Poisson's Ratio of the macroscopic (composite) material
$\rho$ :	density
$\sigma_{ij}$ :	stress tensor
$\sigma_c$ :	cell pressure in hollow cylinder experiments
$\sigma_0^o$ :	applied (macroscopic) hydrostatic stress
$\sigma_i$ :	principal stress ( $i=1,3$ )
$\bar{\sigma}_i$ :	effective principal stress ( $i = 1,3$ )
$\sigma_i^o$ :	hydrostatic stress experienced by inclusion $i$
$\sigma_i^o$ :	applied principal stress ( $i=1,3$ )
$\bar{\sigma}_o$ :	mean effective stress
$\sigma_o$ :	hydrostatic confining pressure
$\tau_{ij}$ :	shear stress tensor
$\tau_c$ :	amplitude of cyclic shear stress
$\tau^o$ :	applied (macroscopic) uniform shear stress
$\tau_{oct}$ :	octahedral shear stress
$\varphi$ :	$1-n$ ( $n$ =porosity)
$\omega$ :	inclination of principal stress with respect to the direction of specimen deposition (vertical)



### Latin Letters

A:	constant
a:	radius of contact
B:	constant
B:	parameter B of soil mechanics
B(e):	experimental determined function of the void ratio, e
C:	constant
$c_i$ :	volume fraction ( $i = 1, N$ )
$C_{ijkl}$ :	compliance Tensor
CN:	coordination Number
D:	Constrained modulus
D:	displacement
$D_o$ :	outside diameter of hollow cylinder specimen
$D_i$ :	inside diameter of hollow cylinder specimen
$D_r$ :	relative density
$D_{ij}$ :	constrained stiffness tensor
$D_{ij}^{(K)}$ :	constrained stiffness tensor at a given value of anisotropic stress ratio $K = \sigma_1 / \sigma_2$
$E_{max}$ :	small strain Young's modulus
$E_s$ :	Young's modulus of the spheres
e:	void ratio
$\bar{e}$ :	mean value of $p(e)$
$e_{min}$ :	minimum microscopic void ratio
$e_{max}$ :	maximum microscopic void ratio
F:	yield function

$F$ :	force
$f$ :	coefficient of intergranular friction
$f(\sigma_{ij})$ :	yield function
$f(e)$ :	experimentally determined function of the void ratio
$G$ :	shear modulus
$G^*$ :	macroscopic shear modulus
$G_i$ :	shear modulus of constituent $i$ ( $i = 1, N$ )
$G_s$ :	shear modulus of the material of the spheres
$G_{\max}$ :	small strain shear modulus
$g$ :	plastic potential ( $g=g(\sigma_{ij})$ )
$H$ :	Elastoplastic modulus
$H$ :	height of hollow cylindrical specimen
$H_o$ :	elastic modulus
$H_p$ :	tangential elastoplastic modulus
$H_{ijkl}$ :	tensor which depends on the material symmetry and plastic strain
$K$ :	radius of the yield surface
$K$ :	anisotropic stress ratio, $K = \sigma_1/\sigma_2$
$K^*$ :	macroscopic bulk modulus
$K_i$ :	Bulk modulus of constituent $i$ ( $i = 1, N$ )
$k$ :	yield stress
$m$ :	material constant
$\hat{n}$ :	normal unit vector
$n$ :	porosity
$\bar{n}$ :	mean value of $p(n)$
$n_{ij}$ :	normal vector

$n'_{ij}$ :	deviatoric part of the vector normal to the yield surface
$N$ :	integer (= number of constituents)
$\bar{N}$ :	normal force
$p$ :	hydrostatic stress; $p = \frac{1}{3} \sigma_{ii}$
$p_i$ :	hydrostatic stress at the apex of a yield cone
pdf:	probability density function
$p(e)$ :	probability density function of void ratio
$p(n)$ :	probability density function of porosity
$R$ :	radius of sphere
$R_i$ :	inside radius of hollow cylindrical specimen
$R_e$ :	equivalent radius of spheres of different diameters
$R_{ij}$ :	tensor defining the distortion of the yield surface
$R_o$ :	outside radius of hollow cylindrical specimen
$R_x$ :	reference point in stress space from where yield surface probes start ( $x=a, t$ )
$S_{ij}$ :	initial deviatoric stress state
$s_{ij}$ :	subsequent deviatoric stress state
$S_{ijkl}$ :	stiffness tensor
$\bar{T}$ :	tangential force
$\bar{T}_n$ :	tangential force component normal to the yield surface
$\bar{T}_t$ :	tangential force component tangent to the yield surface
$T_x$ :	tangential force component in the x-direction
$T_y$ :	tangential force component in the y-direction
$\hat{t}$ :	tangential unit vector

$u_{kl}''$	spherical part of a vector normal to the yield surface <b>only</b> on the deviatoric plane
$u_{ij}$	tensor defining the direction of hardening
$V$	total volume of the material
$V_i$	volume of constituent $i$ ( $i = 1, N$ )
$V_p$	compressional (P-wave) wave velocity
$V_s$	shear wave (S-wave) velocity
$V_r$	Rod wave velocity
$v_{ij}$	vector defining the direction of hardening
$\vec{X}$	translation of the center of the yield surface
$\vec{x}$	position vector of the apex of the conical yield surface

## ACKNOWLEDGEMENTS

The authors wish to acknowledge the following people and organizations for their valuable assistance in this project.

The Air Force Office of Scientific Research (AFOSR), Bolling Air Force Base, Washington, D.C. which sponsored the research. Colonel Lawrence Hokanson, Dr. Spencer Wu and Major Steven Boyce, program managers, for their warm support and encouragement.

The Cornell National Supercomputer Facility at Cornell University, for their help and support in some of the numerical simulations reported in Section 2.7 and 4.

The Department of Civil Engineering at the University of Texas at Austin, for their warm hospitality and support provided during the stay of the authors in Austin during academic year 1984-85.

Professor Kenneth H. Stokoe II of the University of Texas at Austin, for his wholehearted support, hospitality stimulating discussions, and for sharing with us some of his valuable experimental data.

Doctor J.F. Peters of the U.S. Army Waterways Experiment Station, for sharing his experimental data with us.

Doctor Gilles Pijaudier-Cabot of Laboratoire de Mecanique et Technologie, E.N.S. Cachar, France, for his stimulating discussions while at RPI regarding the experiments of Section 3.

Professor George Dvorak of Rensselaer Polytechnic Institute (RPI), for his valuable suggestions while developing the analytical model of Section 2.3, as well as for his advice in setting up the experimental procedure of Section 3.

Professor Yehia Bahei-El-Din of RPI, for his suggestions and stimulating discussions which led to the development of the numerical model of Section 2.6, and the development of the experimental procedure of Section 3.

Professor Erhard Krempl of RPI, for his discussions on the experiments of Section 3.

Professor Mark Shephard, also of RPI, and the staff of RPI's Interactive Computer Graphics Center for their ideas and work related to the use of computer graphics in modelling granular arrays, and for permitting the use of computer code ABAQUS.

Professor E.H. Lee of RPI, for his suggestions and stimulating discussions.

Doctort Tang-Tat Ng of RPI, currently working on a related project, for his help in using program CONBAL-2.

Mr. Panos Kotsanopoulos, working on this project, for performing the laboratory experiments in Section 3. Mr. Kotsanopoulos also developed the software used for the data acquisition of the experiments.

Mr. Paul Van Laak, Research Instrumentation Engineer at the RPI Class of 1933 Cyclic Soils Loading Laboratory, for his help in setting up the laboratory hardware used for the experiments of Section 3.

Mr. Li Liu, Research Assistant at RPI, for conducting the numerical simulations in Section 4.

Finally, Miss Jamie Pond, of RPI's Instructional Media, for creating many of the figures, and Mrs. Stella Greener for her help in typing the text of the report.

## 1. INTRODUCTION

This final report presents a summary of the work conducted by the authors in a three year (1986-89) AFOSR sponsored micromechanical research at RPI on the behavior and modelling of granular media. Four progress reports were submitted to AFOSR for years 1986-87 and 1987-88 and are included in the list of references (Petrakis and Dobry 1987, 1987a, 1988, and Petrakis, Dobry and Ng 1988). The final objective of the research is to develop a constitutive model for granular soils expressed in traditional continuum mechanics terms, but grounded on the particulate micromechanical behavior of the material. As sketched in the flow chart of Table 1, this is accomplished by a systematic, mostly analytical, approach to the problem, starting from the response of the contact between two elastic, rough spheres subjected to arbitrary normal and tangential forces, and continuing with the response of regular and random arrays of spheres. Hollow-cylindrical axial-torsional tests on glass beads are also performed to supplement the analytical calculations. These analytical and experimental results are then used to formulate the desired constitutive model for granular media.

The problem of the contact between two identical spheres, originally solved by Mindlin and Deresiewicz for some special cases, had been solved at RPI in 1984 for arbitrary loading through an incremental elastic-plastic model. This general solution was then approximately adapted for unequal spheres, and implemented and used in this research to study a number of regular and random arrays of quartz spheres utilizing several analytical and numerical techniques. These techniques include the pressure dependent Self-Consistent method, the nonlinear Finite Element Method, and the nonlinear Distinct Element Method. The results obtained

ranged from small to large strains and included both monotonic and cyclic loading response.

Definite results and conclusions are presented in this report for most of the tasks included in Table 1. This includes the two-sphere problem, the study of regular arrays, and the use of the Self-Consistent and Finite Element methods to study random arrays of spheres.

The purpose of the experimental effort was to verify the analytical and numerical predictions. This experimental task, also included in Table 1, consisted of eight hollow-cylinder axial torsional tests on glass beads to observe the shape and evolution of yield surfaces of granular media in stress space. Distinct Element numerical simulations on random arrays of spheres were also conducted along the same stress paths used in the experiments. Both experiments and simulations suggest that the yield surface(s) of a granular medium distort(s) in the direction of loading but not in other directions, and this finding is incorporated into the constitutive model proposed at the end of the report.

### 1.1 Brief Review of Constitutive Relations in Soils

Over the past 30 years considerable attention has been given to the development of constitutive laws for engineering materials (Hill 1950, Prager 1955, Mroz 1967, Dafalias and Popov 1976, Drucker and Palgen 1981). Among other formulations the existing models are based on the theories of elasticity, hypoelasticity, plasticity and viscoplasticity. Despite the large number of models, there is no consensus yet within the research community on the best approach.



However, the models based on the theory of plasticity or viscoplasticity appear to be most promising.

Most of the proposed models for soils are based on the incremental theory of plasticity. In these, the total strain increment is equal to the sum of elastic and plastic strain increments,  $d\epsilon_{ij} = d\epsilon_{ij}^e + d\epsilon_{ij}^p$ , with these increments being rate independent (Drucker and Prager 1952, Reyes 1966, Chen 1975, Lade and Duncan 1975, Prevost 1978, Hardin 1978).

A variety of associative and non-associative flow rules have been proposed for the plastic strain increment, of the form:

$$d\epsilon_{ij}^p = d\lambda \frac{\partial g}{\partial \sigma_{ij}} \quad (1)$$

where  $d\lambda$  is a coefficient of proportionality and  $g(\sigma_{ij})$  is the plastic potential function, which may or may not coincide with the yield function,  $f(\sigma_{ij})$  at which plastic strains develop.

In the simplest type of elastic-plastic model, there is only one yield surface. States of stress below that surface are assumed to be elastic. However, soils develop plastic strains even at very small strains; to allow for this behavior, a wide variety of strain-hardening laws have been proposed, including families of yield surfaces and specific strain hardening yield rules. In some of these models the elastic region is completely eliminated, allowing for plastic flow at very low strain levels (Prevost 1978).

An important aspect of the development of elastic-plastic models is the definition of the strain hardening law, which defines the modifications in the yield surface(s) in the course of plastic flow. This is critical for reversible loading, where

the type of strain hardening determines the stress-strain behavior after load reversals. In some of the older general plasticity models developed for monotonic loading, isotropic hardening is assumed (Hill 1950), with the yield surface(s) expanding in size as the stresses increase. With isotropic hardening, a large amount of load reversal is required for additional yielding to occur, in contradiction with the observed behavior in the laboratory.

A better alternative is provided by the kinematic hardening law proposed by Ishlinsky (1954) and Prager (1955), which assumes that the yield surface translates in stress space without changing shape or size during flow. Models with kinematic strain hardening are in better agreement with experimental results than models with isotropic hardening.

Some of the earliest and most popular formulations for sand have been based on the "cap model" of DiMaggio and Sandler (1971). As versatile as "cap models" may be, they have not been successful in accurately modelling cyclic loading conditions.

Similar limitations apply to other models (Balasubramanian and Rohani 1979), and can be argued that the existing plasticity models of the "cap" type are only adequate for monotonic loading of isotropic soil. In an effort to overcome this, a variety of constitutive laws have been proposed which incorporate a combination of isotropic and kinematic hardening (Mroz 1967, Lade 1977). Although these more recent theories represent a considerable advancement over the "cap" models, they too have drawbacks. These include the use of "a priori" geometrical hardening rules, and the fact that they do not predict either the inherent, elastic anisotropy of the soil or the stiffening effect measured after many load reversals.

This elastic (inherent) anisotropy, which is most significant for anisotropically consolidated sand, has been measured in sand by Stokoe and his coworkers (Knox et al. 1982, Koppermann et al. 1982), while Dafalias (1979) has discussed its implications for modelling. In their experiments Stokoe and his coworkers proved that the wave propagation velocity depends on the principal stresses in the direction of wave propagation and particle motion (Fig. 1) and not on the mean stress as proposed by Hardin and Black (1964) and Seed and Idriss (1970). This elastic anisotropy has not, to the best of the authors' knowledge, yet been incorporated into any plasticity model. The existing plasticity models also do not predict the dramatic stiffening occurring in a granular medium which has been precycled for thousands or millions of cycles at small strains ( $\gamma \approx 6 \times 10^{-4}$ ) without experiencing significant volumetric changes (Fig. 2, see also Drnevich 1967). These two examples are the result of micromechanical phenomena and are best modelled once these micromechanical phenomena are understood.

Another way to say the same thing is to state that until now plasticity models for soil have been mostly phenomenological. They have been typically developed from a manageable mathematical formulation, and they have been calibrated and modified by interpreting macroscopic experimental results. The underlying micromechanical phenomena have not been systematically considered. As a result, the existing plasticity models for soils are in need of constant refinement when needed for cases very different from the one the model was originally developed and calibrated for.

The current situation in metal plasticity is quite different. Although modelling of the nonlinear behavior of metals started on a similar phenomenological basis, there has been a shift in the last 20 years or so toward formulating the metal

response with due consideration of micromechanical principles (Budiansky and Wu 1962, Lin and Ito 1965, 1966). Recently this has been enhanced by specific experiments and micromechanical (electron microscopy) measurements (Stout et al. 1985, Helling et al. 1986). The situation is analogous in the modelling of more complex composite materials, where experiments and micromechanical analytical simulations are combined to create the corresponding constitutive law (Dvorak 1987, Dvorak et al. 1988).

Although metal properties are not pressure dependent and their material symmetry does not change as much with loading as in soils, the stress-strain behavior of metals and soils is similar in several respects. As a result, most current soil plasticity models are modified versions of popular phenomenological metal models. Notable examples include the Mroz (1967) model for metals and the Prevost (1978) model for undrained loading of clay, as well as the bounding surface model used by Dafalias and Herrmann (1982). Unfortunately, no plasticity model exists for soil resulting from the combination of specific laboratory experiments and micromechanical principles including numerical simulations of the behavior of granular arrays under load.

Recently, the geotechnical groups at the University of Colorado (Klisinski et al. 1988), US Army WES (Peters 1988), and University College of London (Arthur et al. 1988), working together in a concentrated effort, developed a constitutive law which is based on a series of innovative 3-D laboratory experiments performed for this purpose (Alawi et al. 1988). This may be the first time that a comprehensive experimental investigation is performed in Soil Mechanics which attempts to verify widely accepted rules and assumptions related to hardening, yield surface shape during loading, normality rule, etc (see Fig. 3). The resulting model (Klisinski et al.

1988) is based on the bounding surface model of Dafalias and Popov (1976) and on the theory of "fuzzy" sets. The model was used with moderate success to predict the behavior of sand in the International Workshop on Constitutive Laws at Case Western Reserve University (Saada 1987).

In the above approach many lab specimens were used to define one yield surface, which is satisfactory for monotonic loading but omits the effect of prestraining which in metals is known to play an important role in cyclic loading. Moreover, the development of the corresponding law is again phenomenological and includes no micromechanical considerations, relying instead on the interpretation of the macroscopic results of the above innovative experiments.

## 1.2 Micromechanical Interpretation of the Deformation Mechanism in Polycrystalline Aggregates.

For some purposes, granular soil can be modelled as a pressure-dependent polycrystalline aggregate. Regular arrays of identical spheres studied by Deresiewicz (1958, 1958a) and Petrakis and Dobry (1989) behave like pressure-dependent single crystals. Random arrangements of these regular arrays (polycrystals) have been successfully used to simulate the small strain behavior of sand by means of the Self Consistent and Finite Element techniques (Petrakis and Dobry 1986, 1987). Thus it is useful, from the viewpoint of the development of a constitutive law for granular soil, to review some findings on polycrystalline aggregates such as metals.

Starting in the 1950's, researchers have simulated the elastic-plastic, stress-strain behavior of such polycrystalline aggregates through analytical, semi-analytical, and numerical micromechanical techniques (Hershey 1954, Budiansky and Wu 1962, Lin and Ito 1965, 1966, Hill 1967, Canova et al. 1985). This micromechanical work has not supported the continuum mechanics hypotheses of either pure kinematic or isotropic strain hardening behavior, but has predicted instead a combined translation (kinematic hardening) and distortion of the yield surfaces in the direction of loading. This micromechanical prediction has been verified by several experiments (Naghdi et al. 1958, Phillips 1968, Phillips and Tang 1972, Phillips et al. 1974).

The micromechanical approach commonly used to analyze the elastic-plastic behavior of polycrystals assumes that they are an assemblage of equal anisotropic monocrystals (single crystals), randomly oriented in space (Fig. 4a). This results in an isotropic polycrystal if the spatial distribution of the orientations is statistically uniform. A monocrystal has  $n$  sliding planes<sup>(\*)</sup>, with each plane having  $m$  sliding directions, and with every sliding direction corresponding to a pair of parallel yield planes in stress space. In the limiting case in which an infinite number of possible crystal orientations is assumed, this infinitely sided polyhedron becomes a curved yield surface.

---

(\*) In the literature dealing with polycrystals, they are called "slip planes." Here they will be referred to as "sliding planes," as we will reserve the use of the word "slip" to denote a different phenomenon when discussing the contact between two elastic rough spheres

Plastic strain in the aggregate is caused by sliding of one of the sliding planes occurring in a family of similarly oriented crystals. After sliding has occurred in a number of these families, each surface of the polyhedron mentioned above expands and shifts differently. These sliding directions are all more or less parallel to the direction of the plane of the maximum shear stress acting on the aggregate. As the aggregate is loaded further beyond the elastic range, more crystals and crystal families slide, and increasingly more yield planes pass through the loading point on the yield surface. These yield planes of different orientations intersect at that point on the yield surface and form a corner or vertex (Fig 4b).

This vertex, which is particularly important for stress-strain modelling during cyclic loading, is not easily observed during testing. One reason is that the very large number of monocrystal orientations smoothes the effect, which appears as a "smooth vertex" or distortion of the yield surface in the direction of loading, rather than a sharp corner. Most important, this "vertex" does not appear at all if purely monotonic tests are performed, but it shows up once the loading is reversed at least once. This distortion of the yield surface associated with the vertex reflects the "memory" the material has of prestraining in the direction of loading. The existence of this yield surface distortion in metals has been observed experimentally by a number of researchers in several polycrystalline aggregates, including aluminum, aluminum alloys, brass and magnesium (Naghdi et al. 1958, Phillips 1968, Kelley and Hosford 1968, Phillips et al. 1970, Shiratori et al. 1976, Helling et al. 1986).

The late Professor Phillips developed a testing procedure to seek and compute the initial and subsequent yield surfaces of aluminum and their motion in stress space. This procedure is now widely used in experimental plasticity studies of

metals and metal matrix composites (Rousset 1985, Stout et al. 1985, Dvorak 1987, Dvorak et al. 1988). The experiments are typically conducted by applying a combination of tensile ( $\sigma$ ) and torsional shear ( $\tau$ ) stresses to a hollow cylindrical specimen, in a sequence similar to that shown in Fig. 5. In these tests, the loading stops and reverses as soon as a point on the yield surface is reached — so that the entire yield surface may be determined — as defined by a certain deviation from the linear portion of the stress-strain curve. Fig. 6 clearly shows the characteristic distortion of the initial yield surface in the direction of loading. While the yield surface (for a given temperature) in the  $\tau$ - $\sigma$  space is an ellipse, the subsequent yield surfaces have distorted and become pointed in the direction of loading (a), while becoming flatter in the opposite direction (b). As a result, the size of the yield surface shrinks in the direction of loading while staying constant in the other direction.

Laboratory results such as these have made possible the linking of the micromechanical theory with experiments (Stout et al. 1985, Helling et al. 1986), and have led to a new family of constitutive laws (Phillips and Weng 1975, Eisenberg and Yen 1981, 1984, Yen and Eisenberg 1987) which incorporate the above findings.

### 1.3 Micromechanical Behavior of Granular Soil

As mentioned earlier, the behavior of a sand aggregate is similar to that of a polycrystal, since the individual groups of grains or grain packings within the sand may be considered in first approximation to behave like randomly oriented crystals.



The main difference is that the properties of these packings are now pressure dependent. For example, a simple cubic array of equal spheres (Fig. 7) is a pressure-dependent monocrystal having three sliding planes ( $n=3$ ), with each sliding plane containing two sliding directions  $90^\circ$  apart ( $m=2$ ).

As in the case of polycrystalline aggregates, each sliding plane in each of the packings corresponds to a pair of parallel yield planes in stress space. The macroscopic yield surface of the material is the surface bounding the yield polyhedron, the sides of which are formed by the intersection of these yield planes. Plastic strain, defined as irrecoverable deformation, is the result of a slide in at least one of these packings. A conjecture to be discussed later in this report is that the yield surface of a granular medium distorts during loading, and forms a vertex in the direction of loading through a mechanism similar to those in metals.

Granular media, despite this similarity with metals, are also significantly different due to the pressure-dependent properties of the packing. Specifically, the amount of slide in each packing depends on the normal pressure acting on the plane, as do the moduli and the symmetry of the material. Moreover, granular media experience dilation under shear which is not necessarily present in polycrystalline aggregates. Finally, soils exhibit nonlinear inelastic stress-strain behavior even at small strains. Therefore, strictly speaking, a cohesionless aggregate does not have a clear linear elastic region followed by a region in which permanent deformations occur, like the aluminum tested by Phillips. However, granular soils experience little or not sliding (gross sliding) between particle contacts, and thus exhibit nondestructive behavior and no dilation up to the so called "threshold shear strain,"  $\gamma_t \approx 10^{-4}$  (Dobry et al. 1982). Therefore, in granular soils, loading below  $\gamma_t$  has some important features in common with elastic loading in metals before the initial

yield surface is reached. However, in soils the loading below  $\gamma_t$ , though nondestructive, is inelastic and does include some plastic yielding due to localized slipping within the intergranular contact areas. If this localized slipping effect below  $\gamma_t$  is neglected in first approximation, one possible definition of an initial yield surface in a cohesionless soils could be the surface in stress space where  $\gamma_t$  is reached, there is significant sliding between particles, and permanent volumetric deformation starts occurring due to shear. This may be measured by monitoring the volume in drained experiments or the residual pore pressure in undrained experiments. These inelastic deformations are typically the result of dilatancy in the granular medium and would not occur without this sliding between particles.

## 2. THE MICROMECHANICAL APPROACH

### 2.1 Problem of Contact Between Two Elastic Rough Spheres

The problem of the contact between two elastic rough spheres is of great importance to this research. The small strain behavior of a granular medium formed by spherical particles is controlled jointly by the elasticity and the friction coefficient of the contacts, with friction becoming more important at very large shear strains approaching failure of the medium. Therefore, a brief review of the contact problem will be presented herein, as well as some aspects of the recent numerical solution for the contact problem developed at RPI.

The problem of contact of two elastic, elliptical, semi-infinite bodies subjected to a normal force was first studied by Hertz (1882), with this solution including as a special case the normal compression of two spheres. Hertz demonstrated for the first time that the normal force-deformation behavior at the contact is nonlinear elastic. Subsequently, all work on the same topic was concerned with the loading of bodies by normal forces, until Cattaneo (1938), Mindlin (1949), and Mindlin and Deresiewicz (1953) addressed the problem of the contact of two identical elastic, rough spheres subjected to a combination of normal and tangential forces, and presented a number of closed form solutions for each of several specific load histories. Walton (1978) studied the problem of the oblique compression of two elastic, rough spheres when both tangential and normal forces are applied simultaneously. More recently, Szalwinski (1985) addressed the problem of the contact of two identical elastic bodies which form an elliptical contact area, and compared his solution to those in the literature.

The general case of two identical, elastic, rough spheres subjected to a normal force  $N$  followed by a tangential force  $T$  (Fig. 8), solved by Cattaneo (1938) and Mindlin (1949), is a problem of the linear theory of elasticity. Since the solution yields an infinite shear stress at the edge of the contact area, a slip needs to be prescribed at this edge, which transforms the formulation into a mixed boundary value problem where contact stresses and displacements are prescribed. This permanent set produced by the slip induces a nonlinear behavior, which is different from that computed by Hertz, since it is accompanied by energy dissipation. As demonstrated by Mindlin and Deresiewicz (1953), due to this slip now the force-deformation relation depends on the entire past history of the loading as well as on the instantaneous rates of change of the normal and tangential forces. A typical force-deformation curve for two spheres in contact under a constant normal force,  $N$ , subjected to a monotonically increasing tangential force,  $T$ , is shown in Fig. 8b, where the nonlinear, yielding behavior can be clearly observed.

All of the above suggest that a phenomenological plasticity model could describe this nonlinear behavior. Such a formulation would provide the long awaited (Deresiewicz 1958a) "general" solution to the problem of the contact of two elastic, rough spheres subjected to an arbitrary force history, which in turn could be used in numerical simulations. This has been achieved recently at RPI through a constitutive law (Seridi and Dobry 1984, Dobry et al. 1989) for the force-deformation behavior of two identical elastic, rough spheres in contact under a combination of arbitrarily varying normal and tangential forces, which was implemented through program CONTACT (Dobry et al. 1989). This model is based on the incremental theory of plasticity, uses an infinite number of yield surfaces and assumes kinematic hardening. Therefore, its main features are very similar to those

of the plasticity stress-strain models for engineering materials described previously. These features of the RPI contact model are presented in detail by Seridi and Dobry (1984) and Dobry et al. (1989), and are summarized below:

Yield Condition:

$$(T_x - x)^2 + (T_y - y)^2 = f^2(N - N_i)^2 \quad (2)$$

where  $\vec{x} = x \hat{i} + y \hat{j} + N_i \hat{k}$  is the position vector of the apex of the conic surface, and  $\vec{F} = T_x \hat{i} + T_y \hat{j} + N \hat{k}$  is the current force point (Fig. 9). Since the contact of the two spheres subjected to an increasing tangential force under constant  $N$  is continuously slipping, there must be an infinite number of yield cones. The elastic region is in the inside of the cone whose apex is at the current force point. The failure surface is the outer cone, defined as follows:

$$T^2 = T_x^2 + T_y^2 = f^2 N^2 \quad (3)$$

Flow Rule:

For a given force increment  $d\vec{F} = d\vec{N} - d\vec{T}$ , the increment of displacement between the centers of the two spheres is :

$$d\vec{D} = d\delta_x \hat{i} + d\delta_y \hat{j} + d\alpha \hat{k} = d\vec{\delta} + d\alpha \hat{k} \quad (4)$$

The value of  $d\bar{D}$  is given by:

$$d\bar{D} = \frac{dNk}{\frac{2Ga}{1-\nu}} + \frac{f dN}{H_0} \hat{n} + \frac{dT_n - f dN}{H} \hat{n} + \frac{dT_t}{H_p} \hat{t} \quad (5)$$

where:  $\hat{n}$  = normal unit vector to the yield circle at the current force point.

$\hat{t}$  = tangential unit vector tangent to the yield circle at the current force point.

$$dT_n = d\bar{T} \cdot \hat{n} \quad (6)$$

$$dT_t = d\bar{T} \cdot \hat{t} \quad (7)$$

$$d\bar{T} = dT_n \hat{n} + dT_t \hat{t} = d\bar{T}_n + d\bar{T}_t \quad (8)$$

$$H_0 = \frac{4Ga}{2 - \nu} \quad \text{is the elastic modulus} \quad (9)$$

$H = H_0 (1 - \frac{K}{fN})^{1/3}$  is the elastoplastic modulus corresponding to the yield surface of radius  $K$ .

$H_p = \frac{8Ga}{2 - \nu} \frac{K}{3fN} [1 - (1 - \frac{1}{fN})^{2/3}]$  is the tangential elastoplastic modulus.

$f$  = coefficient of friction of the material of the spheres.

$$a = (BNR)^{1/3}, \text{ with } B = \frac{3(2-\nu)}{8G}$$

R = radius of the spheres.

#### Hardening Rule:

In 3-D force space, the axis of any yield surface translates without rotation in such a way that it remains always parallel to the N axis:

$$d\vec{X} = d\vec{T} - fdN\hat{n} + (K + fdN)d\vec{n} \quad (10)$$

where  $d\vec{X}$  is the translation of the center of the "yield" surface on the  $\pi$ -plane, K is the radius of the yield surface on the  $\pi$ -plane and  $d\vec{n}$  is the change of the direction in the unit vector  $\hat{n}$  normal to the surface on the  $\pi$ -plane of the current force point.

#### 2.1.1 Verification of the Model

The constitutive relation briefly described above, implemented in computer program CONTACT (Seridi and Dobry 1984, Dobry et al. 1989), was subsequently tested to verify that it reproduces accurately the analytical solutions obtained by Mindlin and Deresiewicz (1953). In the numerical solution, the elastic properties of quartz were used as input to the program ( $G_s = 32.9$  GPa,  $\nu_s = 0.15$  and  $f = 0.5$ , White 1965), where  $G_s$  is the shear modulus and  $\nu_s$  the Poisson's ratio of the material of the spheres. Because of the complexity of some of the loading cases, only six of the most easily visualized cases will be presented herein. The

force-deformation curves from the analytical results of Mindlin and Deresiewicz (1953) are reproduced separately in Fig. 10, while the corresponding numerical results obtained with program CONTACT are shown in Figs. 11 to 16.

## 2.2 Differential Stress-Strain Relationships for Regular Arrays of Spheres

Once the solution of the contact problem is known, it can be used to develop incremental stress-strain constitutive laws for regular arrays of spheres. These incremental stress-strain relations can be integrated along specific stress paths in order to determine the large strain response of a regular packing of spheres under a number of loading conditions.

Based on the contact solutions outlined in Section 2.1, it is possible to develop these incremental stress-strain laws with the help of simple geometric considerations if the array is statically determinate, or by using geometric and compatibility relations if the array is statically indeterminate. Such differential stress-strain relationships have been developed, among others, for the simple cubic array (sc) shown in Fig. 17a (Deresiewicz 1958), for the body centered cubic array (bcc) of Fig. 17b (Petrakis and Dobry 1986) and for the face center cubic array (fcc) of Fig. 17c (Duffy and Mindlin 1957). These three arrays have a number of contacts per particle, or coordination number, CN of 6, 8, and 12 respectively. Other regular arrays for which differential stress-strain laws are available include the hexagonal close-packed (Duffy 1959) and the cubical-tetrahedral and tetragonal sphenoidal arrays (Makhlouf and Stewart 1967).



The general differential stress-strain relationship for regular arrays of spheres under isotropic pressure is of the form:

$$d\sigma_{ij} = S_{ijkl}d\epsilon_{kl}, \text{ or } d\epsilon_{ij} = C_{ijkl}d\sigma_{kl} \quad (11)$$

where  $S_{ijkl}$  is the stiffness and  $C_{ijkl}$  the compliance matrix.

In what follows, the nonzero coefficients of  $S_{ijkl}$  or  $C_{ijkl}$  are provided from the studies listed above, for the simple cubic, body centered and face centered cubic arrays.

1. Simple Cubic Array, (sc, CN = 6):

$$S_{1111} = S_{2222} = S_{3333} = \left(\frac{3}{2}\right)^{1/3} (1 - \nu_s)^{-2/3} (\sigma_0 G_s^2)^{1/3} \quad (12)$$

$$S_{1212} = S_{1313} = S_{2323} = \left(\frac{3}{2}\right)^{1/3} \frac{2(1 - \nu_s)^{1/3}}{(2 - \nu_s)} (\sigma_0 G_s^2)^{1/3} \quad (13)$$

2. Body Centered Cubic Array (bcc, CN = 8):

$$C_{1111} = C_{2222} = C_{3333} = \frac{2}{\sqrt{3}} \frac{1}{(4\sqrt{3}G_s^2\sigma_0)^{1/3}} [1 - \nu_s]^{2/3} + \frac{2 - \nu_s}{(1 - \nu_s)^{1/3}}] \quad (14)$$

$$C_{1122} = C_{1133} = C_{2233} = \frac{1}{\sqrt{3}} \frac{1}{(4\sqrt{3}G_s^2\sigma_0)^{1/3}} [(2(1-\nu_s)^{2/3} - \frac{2-\nu_s}{(1-\nu_s)^{1/3}})] \quad (15)$$

$$C_{1212} = C_{1313} = C_{2323} = \frac{4}{\sqrt{3}} \frac{1}{(4\sqrt{3}G_s^2\sigma_0)^{1/3}} [(1-\nu_s)^{2/3} + \frac{1}{4} \frac{2-\nu_s}{(1-\nu_s)^{1/3}}] \quad (16)$$

3. Face Centered Cubic Array (fcc, CN=12):

$$S_{1111} = S_{2222} = S_{3333} = [\frac{3G_s^2\sigma_0}{2(1-\nu_s)^2}]^{1/3} \frac{4-3\nu_s}{2-\nu_s} \quad (17)$$

$$S_{1122} = S_{1133} = S_{2233} = [\frac{3G_s^2\sigma_0}{2(1-\nu_s)^2}]^{1/3} \frac{\nu_s}{2(2-\nu_s)} \quad (18)$$

$$S_{1212} = S_{1313} = S_{2323} = [\frac{3G_s^2\sigma_0}{2(1-\nu_s)^2}]^{1/3} \frac{4-3\nu_s}{(2-\nu_s)} \quad (19)$$

In Eqs. 12-19,  $G_s$ ,  $\nu_s$  are the shear modulus and Poisson's ratio of the material of the spheres, respectively, and  $\sigma_0$  is the (macroscopic) isotropic pressure applied to

the regular array. It should be noted that for a given  $\sigma_o$  Eqs. 11–19 describe linearly elastic, anisotropic continua. This is a result of the crystal anisotropy inherent to any regular array structure. Uniform sand, however, is more or less isotropic under isotropic pressure (Knox et al. 1982, Kopperman et al. 1982, Lade and Nelson 1987), and since the objective herein is to model the behavior of granular soil, it is appropriate to define the conditions for which the stiffness matrices of the arrays become isotropic. From inspection of Eqs. 12–19, it can be seen that the necessary and sufficient condition for these three media to be isotropic under isotropic pressure is that  $\nu_s = 0$  for the material of the spheres. (Duffy 1959, Petrakis and Dobry 1986). The elastic constants of quartz are  $G_s \approx 32.9$  GPa (4780 ksi) and  $\nu_s = 0.15$  (White 1965). Moreover, it has been shown (Duffy 1959) that even when the degree of anisotropy is largest ( $\nu_s = 0.5$ ) the difference between the moduli of the array in different directions is not more than 3.6% to 9%, depending on the array considered.

Consequently,  $\nu_s = 0$  is a reasonable first approximation for quartz spheres forming regular cubic arrays. If  $\nu_s = 0$  is assumed,  $G_{\max} = \frac{1}{2} S_{1212} = \frac{1}{2} S_{1313} = \frac{1}{2} S_{2323} = \frac{1}{2} S_{1111}$ , independent of direction in the three arrays. For given values of  $G_s$  and  $\sigma_o$ ,  $G_{\max}$  is essentially proportional to the coordination number, CN, as illustrated by Fig. 18; the same trend has also been reported by Yanagisawa (1983). This is very interesting, as it shows that the stiffness of a regular array is directly controlled by the number of load-transmitting interparticle contacts, and it suggests that an increased number of contacts works in a way similar to the increase in stiffness of a system of springs in parallel when new springs are added. Of course, as CN increases, the regular array also gets denser and its void ratio,  $e$ , decreases, and therefore Fig. 18 can also be interpreted as showing that  $G_{\max}$  increases as  $e$

decreases. This inverse relation between  $G_{\max}$  and  $e$  is especially useful in actual sands and random arrays, where  $e$  can be easily obtained while CN may be impossible to determine.

Based on the expression for  $G_{\max}$  with  $\nu_s = 0$ , it is possible to compute velocities of shear and compressional waves propagating through the above three regular packings, for wave lengths significantly larger than the radius of the spheres. The shear wave velocity through an isotropically loaded regular array velocity is  $V_s = \sqrt{G_{\max}/\rho}$ , where  $\rho$  is the mass density of the medium. In the same way as  $G_{\max}$ ,  $V_s$  becomes larger as CN increases and  $e$  decreases. A plot of  $V_s$  in regular cubic arrays of quartz spheres versus void ratio,  $e$ , for a given isotropic pressure,  $\sigma_0$ , is presented in Fig. 19a, while Fig. 19b shows the experimental curves for sands reported by Hardin and Richart (1963). While the plots are qualitatively similar, the analytically computed wave velocities for the regular arrays are two to three times higher than those in the actual soils.

It is hypothesized herein that the difference between Figs. 19a and 19b is related to the dependence of shear stiffness on coordination number shown in Fig. 18. That is, the dependence of  $G_{\max}$  and  $V_s$  on the void ratio in real soils is explained by the increase in the number of intergranular contacts as void ratio decreases. This hypothesis has also been made by other authors (Deresiewicz 1958, Ko and Scott 1967). Furthermore, while the empirical relations in sand give  $G_{\max} = Af(e)\sigma_0^{1/2}$  (or  $V_s \propto \sigma_0^{1/4}$ ), where  $f(e)$  is a function of the void ratio  $e$  and  $A$  is a constant, the analytical expressions plotted in Fig. 19a give  $G_{\max} = Bf(e)\sigma_0^{1/3}$  (or  $V_s \propto \sigma_0^{1/6}$ ). These higher values of moduli (and velocities) obtained analytically as compared to measurements, and the difference between the  $1/4$  and  $1/6$  power in the exponent of the confining pressure for  $V_s$ , are well known and have been

observed in the past (Duffy and Mindlin 1957, Deresiewicz 1958). Figure 20 presents a comparison between analytically obtained and experimental values of rod wave velocity,  $V_r = \sqrt{E_{\max}/\rho}$ , where  $E_{\max}$  is the small strain Young's modulus, versus confining pressure,  $\sigma_0$ , in rods constructed of equal steel spheres assembled in the fcc packing. It should be noted that as the pressure increases, not only the dependence of  $V_r$  on the pressure changes from  $\sigma_0^{1/4}$  to  $\sigma_0^{1/6}$ , but also the experimental results approach the theory.

Duffy and Mindlin and Deresiewicz have provided an explanation for the results of Fig. 20, which is consistent with the argument advanced herein to interpret Figs. 19a and 19b. As the particles used for the experiments of Fig. 20 were unequal in size and not perfectly spherical, they had a number of contacts which transmitted little load (spheres barely touching or touching on asperities) or no load (spheres not touching). Consequently, the measured stiffness of the actual medium was less than predicted and the dependence of the velocity on the pressure,  $\sigma_0$ , was not  $1/6$ . When  $\sigma_0$  increased, the barely touching contacts started transmitting their full load and new contacts appeared. As a result, the experimental values of  $V_r$  approached the theoretically predicted ones. This increase in stiffness and change of the dependence of the velocity on the exponent of the pressure from  $1/4$  to  $1/6$  can be explained by this initial increase and subsequent stabilization of the number of effective contacts with pressure, including the influence of the roughness of the actual sphere surface. The above phenomena are illustrated by the two sets of data in Fig. 20, corresponding to high and low tolerance steel spheres. In the low tolerance spheres, having a greater variation of spheres' sizes, the velocity is lower but it increases faster with  $\sigma_0$  at low pressures

than for the high tolerance spheres. Both low and high tolerance spheres approach the theoretical line and the slope  $1/6$  at high pressures (Deresiewicz 1958).

Regular arrays of spheres capture some aspects of the actual sand behavior, and some analytically obtained results are in good qualitative agreement with laboratory measurements on granular soils. As shown previously, they can also be made to behave as a linear isotropic elastic solid once  $\nu_s = 0$  is assumed. However, each one of the three regular arrays has a fixed value of void ratio,  $e$  (see Fig. 18) and thus cannot simulate a sand of arbitrary density. In what follows, an improved random model of granular soil based on combining these three regular arrays is proposed and some of the properties of this regular/random medium are compared to measurements in actual sand.

### 2.3 The Self Consistent Method

One of the most common procedures used to describe the behavior of multiphase (composite) media is the Self Consistent Method (Hill 1965, Budiansky 1965).

This approach was first applied by Hershey (1954) and Kroner (1958) to model the behavior of isotropic and anisotropic polycrystalline media. Hill (1965) and Budiansky (1965) improved the method and applied it to the study of multiphase media; they also developed the basic procedure adopted herein. The improved Hill-Budiansky method yields an estimate of the macroscopic elastic constants of a multiphase medium which is an aggregate of isotropic, linearly elastic materials.

The medium is assumed to consist of continuous, irregular regions containing the constituents, like those of a polycrystal. Furthermore, the shape of these regions is assumed not to deviate much from ellipsoidal. The spatial distribution of the microscopic components is such that this "composite" medium can be assumed to be macroscopically isotropic and homogeneous. The medium has  $N$  constituents and a total volume  $V$ . The volume of the  $i$ th phase is  $V_i$  and the volume concentration of the phase is  $c_i = V_i/V$ . It should be pointed out that in the limiting case of many small concentrations,  $c_1, c_2, c_3, \dots, c_{N-1}$ , the first  $N-1$  phases will tend to appear as individual inclusions in a matrix which in turn is the  $N$ th phase.

In order to obtain the macroscopic elastic constants of the medium,  $K^*$ , a uniform macroscopically stress field  $\sigma_{ij}^0$ , is applied to the medium. Then, assuming that the shape of the "inclusions" is elliptical, and using the solution for an elastic isotropic inclusion inside an elastic, isotropic medium (Eshelby 1957), the elastic field is computed for each of the phases. Finally, in order to determine the effective moduli,  $G^*$ ,  $\nu^*$ , or  $K^*$ , the total strain energy calculated in terms of the individual phase properties,  $G_i, K_i$ , is equated to that of the macroscopic, yet unknown, medium with constants  $G^*$  and  $K^*$ .

For example, to compute the macroscopic shear modulus,  $G^* = \tau^0/\bar{\gamma}$ , where  $\tau^0 = \int_V \tau_{ij} dV$  is the macroscopically applied uniform shear stress, see Hill (1965), and  $\bar{\gamma}$  is the average value of the engineering shear strain,  $\gamma_{ij}$ , over the total volume,  $V$ , the strain energy,  $E$ , is evaluated in terms of the macroscopic material properties (Budiansky 1965):

$$E = \frac{1}{2} \int_V \tau^0 \gamma_{ij} dV \quad (20)$$

In terms of the individual phase properties, Eq. 20 can be rewritten as follows (Budiansky 1965):

$$E = \frac{1}{2} \int_v \frac{\tau^0 \tau_{ij}}{G_N} dV + \frac{1}{2} \int_v \tau^0 (\gamma_{ij} - \frac{\tau_{ij}}{G_N}) dV \quad (21)$$

which in terms of the N individual constituent properties yields

$$E = \frac{V(\tau^0)^2}{2G_N} + \frac{\tau^0}{2} \sum_{i=1}^N (1 - \frac{G_i}{G_N}) \int_{v_i} \gamma_{ij} dV \quad (22)$$

and finally,

$$E = \frac{V(\tau^0)^2}{2G_N} \left[ \frac{1}{G_N} + \sum_{i=1}^{N-1} c_i (1 - \frac{G_i}{G_N}) (\frac{\bar{\gamma}_i}{\tau^0}) \right] \quad (23)$$

Comparing Eqs. 20 and 23, we see that the macroscopic shear modulus is given by

$$\frac{1}{G^*} = \frac{1}{G_n} + \sum_{i=1}^{N-1} c_i (1 - \frac{G_i}{G_N}) (\frac{\bar{\gamma}_i}{\tau^0}) \quad (24)$$

The expression for the macroscopic bulk modulus,  $K^*$ , can be obtained through a similar calculation

$$\frac{1}{K^*} = \frac{1}{K_N} + \sum_{i=1}^{N-1} c_i (1 - \frac{K_i}{K_N}) (\frac{\bar{\epsilon}_{vi}}{\sigma_0}) \quad (25)$$



$G^*$ ,  $K^*$  are the unknown shear and bulk moduli of the medium,  $G_i$ ,  $K_i$  ( $i = 1, \dots, n$ ) are the corresponding moduli of phase  $i$ ,  $c_i = V_i/V$  is the volume concentration of phase  $i$ ,  $\bar{\gamma}_i$ ,  $\bar{\epsilon}_{vi}$  the shear and volumetric strains of this  $i$ th constituent, and  $\tau^0$  and  $\sigma_0^0$  are the applied shear and hydrostatic stresses at the boundary of the medium.

Eshelby (1957) found that, in the case of an ellipsoidal inhomogeneity, the elastic field within the phase is uniform and the corresponding uniform strains are given by:

$$\bar{\gamma}_i = \frac{\tau^0}{G^* + \beta^*(G_i - G^*)} \quad (26)$$

$$\bar{\epsilon}_{vi} = \frac{\sigma_0^0}{K^* + \alpha^*(K_i - K^*)} \quad (27)$$

After substituting Eqs. 26 and 27 into 24 and 25, and then by "smearing out", that is substituting the properties of the matrix which surrounds every "inclusion" (constituent) with those of the resultant, yet unknown, medium, Eqs. 24 and 25 simplify and become:

$$\sum_{i=1}^N \frac{c_i}{1 + \beta^* \left( \frac{G_i}{G^*} - 1 \right)} = 1 \quad (28)$$

$$\sum_{i=1}^N \frac{c_i}{1 + \alpha^* \left( \frac{K_i}{K^*} - 1 \right)} = 1 \quad (29)$$

where  $a^*$  and  $b^*$  are constants depending on the shape of the inclusion (Eshelby 1957). For spherical inclusions:

$$\alpha^* = \frac{1+\nu^*}{3(1-\nu^*)} \quad (30)$$

$$\beta^* = \frac{2(4-5\nu^*)}{15(1-\nu^*)} \quad (31)$$

and the Poisson's Ratio of the medium,  $\nu^*$ , is

$$\nu^* = \frac{K^* - 2G^*}{6K^* + 2G^*} \quad (32)$$

Finally, the elastic constants of the macroscopic medium,  $G^*$ ,  $K^*$ , are obtained by solving Eqs. 28–32 simultaneously. The solution obtained through this method always lies between the Voigt and Reuss bounds (spatial averages of the Stiffnesses and Compliances, respectively) and, under certain conditions, between the more strict Hashin and Shtrickmann (1963) bounds (Hill 1965, Budiansky 1965).

#### 2.4 A Model of a Random Array of Equal Spheres

Smith et al. (1929) observed that after shaking and tamping had been applied to a random arrangement of equal spheres, the medium appeared to be composed of clusters of dense and loose regular arrays. These measurements also showed that CN ranged between 6 and 12 contacts per sphere, which corresponds to the theoretical range for regular arrays.

Additional experimental work by Bernal and Mason (1960), Bernal et al. (1964), Scott (1960), Davis and Deresiewicz (1974), Shahinpoor and Shahrpass (1982), and Finney (1985), has confirmed that both 2-D and 3-D random assemblages of equal spheres tend to crystallize. Consequently, it is generally accepted that an assemblage of identical spheres can be modelled by a combination of regular arrays, as idealized in Fig. 21a, where each polyhedron contains a regular packing. The macroscopically observed porosity would then be obtained by the appropriate combination of the porosities of the packings weighed by their volume fractions,  $c_i$  (Finney 1983, Backman et al. 1983).

Therefore, the authors developed a model of a random array of equal spheres consisting of randomly distributed clusters of  $N$  regular packings such as the three cubic arrays discussed previously. Furthermore, every regular cluster is assumed to be isotropic (that is, for cubic arrays, the Poisson's ratio of the spheres,  $\nu_s = 0$ ). Each of these clusters is considered to be an inclusion in the macroscopic medium, such as shown by the observation of an actual random 2-dimensional array of spheres in Fig. 21b, where regions of loose and dense packings can be clearly seen. One could imagine the 2D medium of Fig. 21b to be a cross section of the 3D medium of Fig. 21a, which would be composed of an appropriate combination of the three regular arrays: fcc (dense clusters) bcc (less dense clusters) and sc (loose clusters). In this case,  $N = 3$ .

As a second step, a suitable combination of volume concentrations  $c_i$  ( $i = 1, \dots, N$ ), which yields the desired porosity of the random array, needs to be defined for  $N$  regular arrays. For this, the model proposed by Shahinpoor (1981) is used. In his work, Shahinpoor derived an analytical expression for the spatial probability density function, pdf, of the void ratio,  $p(e)$ , in a three-dimensional random packing of

equal steel spheres, which he later confirmed experimentally in two dimensions by means of an optical scanning technique (Shahinpoor and Shahrpass 1982).

Finally, once the volume fractions,  $c_i$ , have been determined for the regular arrays, the Self Consistent method is used to average the properties of the  $N$  regular arrays within the (unknown) macroscopic medium, which is compressed at its boundary by a hydrostatic pressure,  $\sigma_0$ , and subsequently loaded by a small increment of stress,  $d\sigma_{ij}$ . Of course, for these granular arrays the Self-Consistent method must be modified to account for the effect of  $\sigma_0$  on the elastic properties of both the medium and regular array clusters.

The first step in the application of the proposed method to random packings of spheres is to define the phases or constituents. Here, the sand will be assumed to consist of the three regular arrays of spheres: sc, bcc, and fcc. The expression of the pdf,  $p(e)$ , is (Shahinpoor 1981):

$$p(e) = \frac{\lambda \exp(-\lambda e)}{\exp(-\lambda e_{\min}) - \exp(-\lambda e_{\max})} \quad (32)$$

where  $\lambda$  is a constant defined by the following equation

$$\bar{e} = \frac{1}{\lambda} + \frac{e_{\min} \exp(-\lambda e_{\min}) - e_{\max} \exp(-\lambda e_{\max})}{\exp(-\lambda e_{\min}) - \exp(-\lambda e_{\max})} \quad (33)$$

and  $e_{\min}$ ,  $e_{\max}$  are the minimum and maximum values of the void ratios of the constituents ( $e_{\min} = 0.32$ ,  $e_{\max} = 0.91$  for identical spheres) and  $\bar{e}$  is the mean value of the distribution.

Since the mean value of the pdf of the porosity,  $p(n)$ ,  $\bar{n}$ , coincides with the macroscopic average (measured value) of the porosity of the granular medium, whereas the mean void ratio does not, the pdf of the void ratio,  $p(e)$ , is transformed into  $p(n)$  by using the transformation  $p(n) = |de/dn|p(e)$  (Benjamin and Cornell 1970). Then the appropriate  $p(n)$  is chosen so that  $\bar{n}$  coincides with the macroscopically measured value. The continuous function  $p(n)$  is subsequently lumped at the three porosities of the regular arrays and thus the volume concentrations are determined. If now it is assumed that the above three regular packings form clusters ("inclusions") within the macroscopic medium, which are approximately ellipsoidal in shape (spherical, in this instance for simplicity) the Self Consistent Method described by Eqs. 24–32 can be applied. This case of a granular medium is rather complex since the properties of the constituents,  $G_i$ ,  $K_i$ , as well as of the whole medium,  $G^*$ ,  $K^*$ , are pressure dependent. Furthermore, the pressure taken by each inclusion,  $\sigma_o^i$ , which influences directly its elastic constants (see Eqs. 11–18), depends on the moduli of both the inclusion and the macroscopic, yet unknown, medium. Once again, the pressure  $\sigma_o^i$  inside inclusion  $i$  can be computed from the Eshelby solution as follows:

$$\sigma_o^i = \sigma_o^0 \frac{K_i}{K^*} \left[ \frac{1}{1 + \alpha^* \left( \frac{K_i}{K^*} - 1 \right)} \right] \quad (35)$$

Finally, the problem reduces to the simultaneous solution of Eqs. 28–32 and 35 in which the values of  $G_i = G_i(\sigma_o^i)$  and  $K_i = K_i(\sigma_o^i)$  are given by Eqs. 11–18 and the volume concentrations,  $c_i$ , from the lumped  $p(n)$  for  $i = 1, 2$  and 3 corresponding to the sc, bcc and fcc arrays respectively.

## 2.5 Application of the Self-Consistent Method to Uniform Rounded Sand

The proposed model was evaluated by predicting the small strain shear moduli,  $G_{\max}$ , of a rounded, uniform, quartz sand which had been subjected to isotropic pressure in the resonant column device and was then heavily precycled (Fig. 2). This was achieved by using as input the elastic properties of quartz for the individual spheres (grains):  $E_s = 75.8$  GPa (from  $G_s = 32.9$  GPa and  $\nu_s = 0.15$ , White 1965). However, in order to ensure that the individual arrays as well as the macroscopic medium are isotropic under isotropic pressure, a value of  $\nu_s = 0$  was assumed here for the Poisson's ratio of the spheres and used with  $E_s = 75.8$  GPa. The actual value of  $\nu_s$  is very small already, and as mentioned previously, this substitution does not affect the values of the moduli of the arrays in different directions by more than about 2–3%.

The computed values of  $G_{\max} = G^*$  appear in Fig. 22 (continuous lines) plotted versus the isotropic confining pressure acting on the medium,  $\sigma_o^0$ , for  $e = \bar{n}/(1-\bar{n})$ , equal to 0.46, 0.54 and 0.58. The corresponding values of bulk modulus,  $K^* = \sigma_o^0/\bar{\epsilon}_v$ , were also computed, and Fig. 23 contains a plot of the confining pressure,  $\sigma_o^0$ , versus the resulting average volumetric strain,  $\bar{\epsilon}_v$ , predicted by the model for  $e = 0.54$ . The volumetric strain was derived from this bulk modulus,  $K^*$ , for different  $\sigma_o^0$ :  $\bar{\epsilon}_v = \sigma_o^0/K^*$ .

Figure 22 also contains experimental data from precycled Ottawa C-109 sand where millions of cycles were applied to isotropically consolidated hollow cylindrical specimens. This is the same research previously discussed in connection with Fig. 2 (Drnevich 1967). The data in Fig. 22 are for the same void ratios used in the analytical simulations, with a number of cycles,  $N$ , between  $1 \times 10^6$  and  $22 \times 10^6$ ,

and an applied cyclic torsional shear strain,  $\gamma_{\theta x}$ , between  $3 \times 10^{-4}$  and  $6 \times 10^{-4}$ . This precycling increased the sand stiffness more than three times, while at the same time the void ratio stayed about constant and equal to the initial, virgin specimen (dotted line in the figure). Furthermore, the precycling modified the dependence of  $G_{\max}$  on pressure,  $\sigma_o^{(*)}$ , from about  $\sigma_o^{1/2}$  to  $\sigma_o^{1/3}$  (Fig. 22c), and made the experimental results approach closely the theoretical values after a very large number of cycles. Those trends provide strong confirmation to the hypothesis that sand behaves as predicted by the theory, once the theoretical number of load transmitting contacts is reached, in this case as a result of many cycles of shear precycling.

In Fig. 23, an additional hydrostatic compression was applied to a specimen after precycling it  $1 \times 10^6$  times at a cyclic shear strain of  $6 \times 10^{-4}$  (square data points). Here, the stiffness of the medium approached the theoretical values faster than did the shear stiffness in Fig. 22, for the same number of cycles. This happened probably because, in addition to the precycling there was a subsequent increase in the confining pressure, which completed the formation of contacts started by the repeated shearing.

Additional experimental data from resonant column tests on 30–40 Ottawa C-109 sand, this time on solid specimens, covering a wide range of densities from dense to medium loose, are presented in Fig. 24 (Song and Stokoe, 1987). The strain amplitude in these experiments was  $\gamma_{\theta x} = 6 \times 10^{-4}$ . It can be clearly seen

---

(\*)  $\sigma_o$  and  $\sigma_o^*$  are both used interchangeably herein in the text and figures to denote the macroscopic, isotropic pressure applied to the medium.

that while again the value of the shear modulus,  $G_{\max}$ , increases dramatically with number of cycles (Fig. 24a), the void ratio remains essentially constant (Fig. 24b). It becomes almost certain, then, that this increase in the stiffness is not caused by any great change in the particulate structure of the medium, which would have manifested itself through a change in the macroscopic void ratio, but by the much subtler change associated with an increase of the number of contacts at constant void ratio, as one could deduce from Figs. 20 and 24. With the continuous cycling at small strains, probably not only new contacts were created between the sand grains, but old "dead" ones became load-transmitting ("live"), resulting in the excellent agreement between theory and experiment in Fig. 22 after many cycles.

Finally, Fig. 25 presents the variation of shear modulus at small strains,  $G_{\max}$ , with number of contacts per sphere  $CN$  and with  $\sigma_0$  calculated from: i) the three regular cubic arrays, that is from Fig. 18; ii) the Self Consistent Method; and iii) the analytical solution of Walton (1987). Walton, by considering the pressure dependent normal and tangential compliances at the interparticle contacts derived the following expressions for the two elastic moduli (Lame constants),  $\lambda^*$  and  $\mu^* = G_{\max}$ , of a random packing of equal elastic spheres with an infinite coefficient of friction under an isotropic pressure  $\sigma_0$ :

$$\lambda^* = \frac{C}{10(2B+C)} \left[ -\frac{3\varphi^2(CN)^2\sigma_0}{\pi^4 B} \right]^{1/3} \quad (35)$$

$$\mu^* = G_{\max} = \frac{(5B+C)}{10(2B+C)} \left[ -\frac{3\varphi^2(CN)^2\sigma_0}{\pi^4 B} \right]^{1/3} \quad (36)$$



where  $\varphi=(1-n)$ , and  $n$  is the average porosity of the medium,  $B$  and  $C$  are constants which depend on the material properties of the spheres,  $G_s$  and  $\nu_s$ , and  $CN$  is the average coordination number.

The final result is the very consistent plot of Fig. 25, with the Self Consistent Method providing a prediction in excellent agreement with the analytical results by Walton (in Eqs. 35 and 36,  $\nu_s$  was set to zero and the coordination number was given by this Self Consistent scheme). Thus, the earlier hypothesis, extrapolated from the regular arrays, that the small strain shear modulus,  $G_{max}$ , of a random array of equal spheres is essentially a linear function of the average number of contacts per particle is confirmed and justified by two different analytical approaches.

## 2.6 A Two-Dimensional Numerical Model of Granular Soil at Small Strains

In the previous section, a closed form solution was obtained for the elastic constants of a random aggregate of equal, rough, elastic spheres having an arbitrary macroscopic void ratio and subjected to isotropic loading. This was done through the use of the Self-Consistent Model and on the assumption that the array is composed of different phases, and the results contributed to an improved understanding of the small strain behavior of sands under isotropic conditions. The fact that this analytical solution was obtained with relatively small effort should be attributed to the high level of symmetry of such a system under isotropic pressure.

Since the Self Consistent Method was developed to determine the elastic constants of a multiphase medium, it is not suitable for the determination of

elastoplastic properties. Although there have been modifications proposed to adapt the Self Consistent Method to nonlinear behavior, these adaptations would not work in the case of a granular medium, since particle sliding changes the material configuration and thus it also changes the distribution of the various volume fractions. Moreover, the symmetry of the constituents would change dramatically with loading and the problem would become intractable. To overcome this, it was decided to attempt a numerical model, which although containing assumptions similar to those of the Self Consistent Method, could perform numerically the integration of the equations to larger strain levels. This model is similar to those proposed by a number of researchers (Budiansky and Wu 1962, Lin and Ito 1965, 1966) as discussed in Section 1.1, in that it is composed of regular packings of spheres randomly oriented so as to ensure a statistically isotropic medium. The properties of the packing to be used as basic "element" of this medium is defined by the contact law described in Section 2.1. In other words, the constitutive law of this regular packing is similar to those described by Eqs. 12-18, but now the compliances are given by program CONTACT described in Section 2.1.

#### 2.6.1 Nonlinear Finite Element Simulations

In order to model the behavior of granular soil at small strains, a two-dimensional numerical model was developed which calculates the response of a random aggregate of equal, elastic, rough spheres under an arbitrary boundary stress state,  $\sigma_{ij}$ . For this, a finite element analysis was performed in which the element corresponded to a simple cubic array of equal, rough elastic quartz spheres. Each

2D element contains an undetermined number of spheres, and is assumed to be subjected to a uniform stress field so that four spheres can be used to represent the above element (Duffy and Mindlin 1957). Figure 26 sketches this individual element. The stress-strain behavior of this array under a biaxial state of stress,  $\sigma_{11}$  and  $\sigma_{22}$ , followed by pure shear, appears in Fig. 27c. Figures 27a and 27b portray the force-deformation behavior of the "weak" and "strong" contacts for the same case, respectively. Therefore, the behavior of this packing under biaxial loading is the result of the interaction of the two sets of contacts. In this element, the force-deformation relation at each of the contacts between spheres is given by the numerical solution discussed in Section 2.1, through program CONTACT, and the constitutive law is obtained by combining the numerical solutions through geometric considerations. The element cannot sustain a tensile stress normal to the slip planes, since this would imply that the corresponding contacts would cease to exist, and as a result the particles would attempt to rearrange and form a new packing. Although this rearrangement obviously happens in actual sand aggregates, its simulation is too complex and computationally demanding to implement in the present finite element code, and the decision was made to make the contact normal forces positive-definite, that is they can be either positive or zero, but never negative.

A subroutine implementing the behavior of this element was coded into the nonlinear finite element program ABAQUS (1982) as a user defined material subroutine (UMAT). Finally, an incrementally linear analysis was done using eight noded elements with reduced integration.

Several media were used in these simulations consisting of a number of simple cubic arrays in two dimensions (a monolayer of equal spheres assembled in simple

cubic patterns), oriented in a such a way as to resemble a statistically isotropic random aggregate. As discussed above, each of the elements is a simple cubic array, randomly oriented, and the number of elements used in each of these media varies from 16 (4 x 4) to 64 (8 x 8) as illustrated in Fig. 28. Therefore, the medium has the same properties of the simple cubic array in terms of void ratio and coordination number. Although other packings could in principle have been used, it would have been more difficult (Petrakis and Dobry 1987). It was felt that the inability of varying the void ratio or the coordination number (number of contacts per particle) did not unduly constrain the planned FE simulations, which were expected to provide useful insight into the behavior of a sand at small strains.

### 2.6.2 Monotonic Finite Element Loading Simulations

As a first step, the isotropy of the media used was verified by loading them isotropically up to  $\sigma_0^0 = 100$  KPa, followed by pure shear which was applied incrementally. This was accomplished by imposing on each medium a predetermined direction of the major principal stress. The values used for the angle,  $\alpha$ , between the major principal stress and the vertical direction of the medium (Fig. 29a) were  $0^\circ$  (compression in the vertical direction);  $22.5^\circ$ ;  $45^\circ$  (pure shear in the vertical and horizontal planes);  $67.5^\circ$ ; and  $90^\circ$  (extension in the vertical direction). The results of these simulations are shown in Fig. 30 as plots of the applied deviator stress,  $\sigma_1^0 - \sigma_2^0$ , versus the resultant shear strain,  $\gamma = \epsilon_1 - \epsilon_2$ . Figure 30 includes results of all four media composed of 16 and 64 elements of Fig. 28.

It can be seen in Fig. 30 that the medium is indeed isotropic under isotropic pressure, as expected. Since Fig. 30 shows that the difference between the stress-strain behavior of the 16-element and 64-element media is not significant, it was decided that for subsequent parametric studies, as well as for monitoring the stress-strain behavior of each element, any of the less costly 16-element media could be used as representative of the aggregate. In another simulation using Medium 2 with 16 elements, a monotonically increasing hydrostatic pressure was applied up to  $\sigma_0^0 = 500$  KPa, and it was observed that both the macroscopic and the microscopic (element) response exhibits a locking nonlinear elastic behavior, similar to that observed in sand (Fig. 31, see also Fig. 23).

Therefore, the media being used in the numerical experiments simulate well important aspects of the behavior of actual, uniform, rounded sand, by being isotropic under isotropic pressure, yielding in shear and locking under hydrostatic compression. That is, these "random" media have the desirable properties of the regular simple cubic array without its problematic aspects.

In the numerical simulations of pure shear summarized in Fig. 30, it was observed that the yielding/failure process of the medium occurs in two successive stages. In the first stage, a growing number of "soft" elements, oriented more or less parallel to the directions of the applied shear stress, slide and this sliding accounts for the increasing nonlinearity of the curves in Fig. 30, as the shear strain,  $\gamma = \epsilon_1 - \epsilon_2$ , increases from 0 to values around  $0.1 \times 10^{-3}$ . At these larger values of shear strain, typically around 20% of the elements have already slid (failed). In the second stage, occurring at about  $\gamma = \epsilon_1 - \epsilon_2 = 0.16 \times 10^{-3}$ , one or several of the "stiff" elements, oriented more or less perpendicular to the direction of the shear stress, and which had not yet slid, tend to separate as the normal force at the

contact becomes zero, the corresponding ratio shear/normal force at the contact reaches  $f$ , and the element slides. This, of course, is related to the fact that the normal contact force is allowed to be zero but not negative. Once some of the "stiff" elements fail due to this tendency to separate, a growing number of both "soft" and "stiff" elements slide in the next increment(s) by a combination of shear stress increase and separation tendency, thus precipitating the failure of the medium, occurring at  $\tau_f = 44.8$  KPa. This value of  $\tau_f$  is close to, but slightly less than the yield stress of the simple cubic array subjected to pure shear on the sliding planes of the array:  $\tau = (0.5)(100) \approx 50.0$  KPa. This "failure" of the aggregate, defined here by the sequence of phenomena just described, which at the end result in the global stiffness matrix of the medium becoming singular, is associated with a generalized tendency of the particles to slide, separate and rearrange themselves into more stable positions. This corresponds roughly to the changes in geometry occurring in actual sands at the threshold strain,  $\gamma_t = 0.1$  to  $0.2 \times 10^{-3}$  (Dobry et al. 1982), as verified by the fact that "failure" of the medium in Fig. 6 occurs at a shear strain,  $\gamma = \epsilon_1 - \epsilon_2 = 0.16 \times 10^{-3}$ .

### 2.6.3 Cyclic Finite Element Loading Simulations

The (16-element) Medium 1 was also subjected to an isotropic stress of  $\sigma_0^0 = 300$  KPa followed by a complete isotropic cycle with an amplitude 200 KPa, that is  $\sigma_0^0$  was first increased to 500 KPa and then decreased to 100 KPa, and then back to 500 KPa. The stress-strain behavior calculated for the medium is

presented in Fig. 32, and it shows a nonlinear elastic behavior similar to that of actual sands (Ko and Scott 1967).

The same 16-element medium, consolidated isotropically to  $\sigma_0^0 = 100$  KPa, was also cycled under pure shear conditions, with an amplitude of shear stress,  $\tau_c = 20, 30, 35, 40$  and  $43$  KPa. The hysteresis loops for  $\tau_c = 40$  and  $\tau_c = 43$  KPa appear in Figs. 33a and 33b, respectively.

#### 2.6.4. Computation of Dynamic Properties and Wave Propagation Velocities.

The secant shear moduli,  $G$ , obtained from the pure shear simulations at different angles  $\alpha$  for the constant mean stress case (Fig. 30), were normalized with respect to the shear moduli at very small strains,  $G_{\max}$ , obtained in the same simulations, and the corresponding values of  $G/G_{\max}$  versus shear strain are plotted in Fig. 34a, where they are compared with the bounds proposed by Seed and Idriss (1970) from actual tests on sands. The corresponding damping ratio,  $\xi$ , obtained from the loops under cyclic pure shear (Fig. 33) is plotted against cyclic shear strain in Fig. 34b. Figure 34 corresponds to simulations done at a mean stress of 100 KPa. Figure 34 also includes the corresponding curves for  $G/G_{\max}$  and damping ratio for the case of pure shear along the sliding planes of a simple cubic array, computed by Dobry et al. (1982). The slopes of both the  $G/G_{\max}$  and damping ratio versus  $\gamma$  curves in Fig. 34 for the aggregate are flatter than that of the simple cubic array. This "stiffer" behavior of the aggregate, as compared to that of a single cubic array, should be attributed to the interaction between the elements of the medium.

Finally, the small strain constrained moduli,  $D_{ij}$ , were computed in both principal (vertical and horizontal) directions, as follows: The medium was loaded to the desired biaxial stress ratio,  $K = \sigma_1^0 / \sigma_2^0$ , and then very small stress increments with the appropriate sign were applied,  $\Delta\sigma_1^0, \Delta\sigma_2^0$ , the corresponding differences in strain were computed and, finally, the small strain constrained moduli of the medium,  $D_{11}, D_{22}$  were calculated in both directions. The results of this simulation are shown in Figs. 35a and 35b as plots of the normalized constrained moduli of the medium,  $D_{22}^{(K)} / D_{22}^{(1)}$  and  $D_{11}^{(K)} / D_{11}^{(1)}$  versus the stress ratio  $K = \sigma_1^0 / \sigma_2^0$ , where  $D_{ii}^{(K)}$  is the constrained modulus at a given  $K$ , and  $D_{ii}^{(1)}$  the corresponding constrained modulus under the initial isotropic stress,  $\sigma_0^0$ . The same figure includes also data points from a number of measurements on sand in the large cubic facility at the University of Texas at Austin (Kopperman et al. 1982), which were performed during a test similar to that defined for these numerical simulations. The agreement between normalized experimental results and numerical simulations in Fig. 35a and 35b is excellent. Consequently, the main conclusion obtained from the University of Texas laboratory results, that the P-wave velocity propagating along a principal stress direction is only a function of the value of that principal stress is fully predicted by the numerical experiments. Therefore, as previously hypothesized by the authors, this is an effect due to the particulate nature of the soil, which can be explained and reproduced analytically once this particulate nature is taken into account.



## 2.7. Two-Dimensional Nonlinear Distinct Element Simulations

After the discussion on the limitations of the nonlinear finite element model described above, it was decided to use a different type of numerical simulation, capable of modelling granular soil subjected to large strain anisotropic loading, in which contact separation, sliding and rearrangement of the particles are allowed.

There are several approaches to model the behavior under load of random arrays of equal and unequal spheres. One of the most widely used procedures is the "Distinct Element Method" (Cundall and Strack 1979), who have used an explicit finite difference scheme to determine the static response of an array to applied strains (program TRUBAL) or to applied boundary displacements (program BALL).

Program TRUBAL (Strack and Cundall 1984) was modified at RPI by Ng and Dobry (1989) within another, NSF sponsored project, by replacing the existing arbitrary linearly elastic-perfectly plastic, non pressure dependent, force displacement relation at the intergranular contacts, by the more realistic and rigorous Hertz-Mindlin contact law. This was accomplished once more by attaching program CONTACT, described in Section 2.1, as a subroutine in TRUBAL (Table 2). The new two-dimensional program was named CONBAL-2 ; it is very similar to three-dimensional program TRUBAL, but it has one less dimension, due to the increased computation and storage requirements imposed on the program by the nonlinear subroutine CONTACT. Moreover, program CONBAL-2 has been vectorized to run more efficiently on a supercomputer with vector facilities. Another difference is the absence of particle rotation in

CONBAL-2, as this causes as yet unsolved problems in the numerical simulations. This absence of rotation as well as the 2-D nature of the simulation make the random arrays of spheres somewhat stiffer than actual 3-D arrays and soils; Ng and Dobry (1989) have accounted for this by reducing the interparticle angle of friction from 0.5 to 0.35. Therefore, CONBAL-2 is very similar to TRUBAL, except for the differences noted above.

The results of extensive parametric studies performed to check the accuracy of this new program appear in Ng (1989). These parametric studies established the appropriate range of the necessary input variables (time step, strain rate and damping) and confirmed the excellent agreement between the results of CONBAL-2 and existing analytical results. At this point, a copy of CONBAL-2 became available to the AFOSR project for research on the stress-strain behavior of granular soil.

As a first step, it was decided to start simulating phenomena in the small strain range, and at a later stage to focus on the large strain, fully nonlinear inelastic behavior. Furthermore, it was also decided to compare the results of CONBAL-2 with answers obtained using the analytical and numerical procedures presented in Section 2, as well as with experimental data in the literature.

Since the interparticle force-deformation relationships developed by Cattaneo (1938), Mindlin (1949) and Mindlin and Deresiewicz (1953) apply only to spheres of the same sizes and same properties, only random arrays of equal and moderately unequal spheres were developed and studied. Program CONTACT, and thus CONBAL-2 can, in principle handle only random arrays of equal spheres; however, the same program, with certain assumptions, can handle in first approximation moderately unequal spheres of the same material.

### 2.7.1 Small Strain Moduli of Isotropically Compressed Random Arrays of Equal Spheres.

Two different 2-D random arrays of 477 identical particles having the properties of quartz were generated using CONBAL-2. The first array was very loose with an average coordination number, CN, of 2.1, while the second was medium dense with CN=3.0. These arrays were then subjected to three different values of isotropic pressure ( $\sigma_0=91, 334$  and  $698$  KPa) without significant change in their average number of contacts.

The configuration of the array with CN=3.0 subjected to  $\sigma_{11} = \sigma_{22} = \sigma_0 = 91$  KPa, is shown in Fig. 36, where the circles represent the spheres and the rectangles the relative magnitudes and directions of the contact forces. There are four different rectangle widths, with each one of them corresponding to a range of forces between four equal fractions of the maximum computed contact force. For example, if the maximum contact force is  $F$  KN, the narrowest rectangle stands for the range of forces between 0 and  $F/4$  KN, the next wider rectangle for the range of forces between  $F/4$  and  $F/2$  KN, etc. This notation will be used throughout this report whenever results from the distinct element method are presented.

Figure 37 portrays some of the micromechanical statistics which are calculated as a result of the isotropic compression simulation. Figure 37 includes the frequency distributions of contact angles, mobilized angle (angle between contact force and contact normal), coordination number and contact force. As can be seen in the above distributions, the array is not perfectly isotropic. This is a result of the small number of spheres used in the periodic cell, coupled with the crystallization which occurred due to the identical sizes of all 477 spheres. The combined effect of these

two features has increased the "characteristic size" of the smallest constituent to that of a crystalized region; as a result the array is not statistically isotropic. Another important observation is the transmission of the applied forces through columns of particles, in which all "columns" experience the same contact force; this has caused the contacts to form along preferential directions rather than uniformly in all directions.

These deviations from isotropic behavior are not that significant, however, and the 477-particle arrays can be considered to be isotropic, at least in first approximation.

These two arrays of 477 equal particles were subsequently used to compute the small strain shear modulus  $G_{\max}$  under three levels of isotropic pressure:  $\sigma_0 = 91$ , 334 and 698 KPa. The shear modulus was computed by applying an increment of macroscopic shear strain,  $\Delta\gamma = 1 \times 10^{-6}$ , and computing  $G_{\max}$  as  $G_{\max} = \Delta\tau / \Delta\gamma$ . The results of this simulation appear in Fig. 38 (diamonds), as a plot of  $G_{\max}$  versus the Coordination Number. In this figure they are also compared with the values obtained from the regular arrays of spheres, the Self Consistent method and the analytical expressions of Walton (1987), already discussed in Section 2.5 and plotted in Fig. 25. In order to compare the 2-D results obtained by the Distinct Element Method with those obtained by other 3-D approaches, it was decided to adjust the coordination number to account for the third dimension. The only regular packing of identical spheres where a clear relation can be established between the coordination number and  $G_{\max}$  in two and three dimensions is the simple cubic array, which has the same shear moduli in 2 and 3-D. In this regular array,  $CN=4$  for 2-D and  $CN=6$  for 3-D. Therefore the values of the coordination number in the Distinct Element Simulations of Fig. 38 were multiplied by  $6/4=1.5$ . The final

result is the very consistent plot of Fig. 38 using points from four different methods. The plot essentially confirms the hypothesis presented by Yanagisawa (1983) and Petrakis and Dobry (1986) that the small strain shear modulus,  $G_{\max}$ , of a random array of equal spheres is in first approximation a linear function of the average number of contacts per particle.

### 2.7.2 Small Strain Moduli of Anisotropically Compressed Random Arrays

The same 2-D array already discussed with 477 equal elastic, rough spheres and coordination number,  $CN=3$ , consolidated under  $\sigma_0 = 91\text{KPa}$  (Fig. 36), was further loaded in program CONBAL-2 under biaxial compression to  $\sigma_{22} = 233\text{KPa}$ , while keeping  $\sigma_{11}$  constant. This was done to: i) investigate the influence of the magnitude and direction of the principal stress on the constrained moduli,  $D$ , and also on the velocities of P-waves propagating through the medium, ii) interpret the experimental findings of Kopperman et al. (1982), and iii) verify the results of the nonlinear finite element model presented in Section 2.6.

The constrained moduli,  $D_{ii} = \rho V_p^2$  were calculated in the same way as in the nonlinear finite element model of Section 2.6, as follows: once the desired stress ratio,  $K = \sigma_1/\sigma_2 = \sigma_{22}/\sigma_{11}$ , was reached at specific points during loading, very small increments,  $d\epsilon_{11}$ ,  $d\epsilon_{22}$ , equal to  $1.062 \times 10^{-6}$  were applied to the array with the appropriate signs. The corresponding stress increments,  $d\sigma_{11}$ ,  $d\sigma_{22}$ , were computed, and finally, the small strain constrained moduli,  $D_{ii}^{(K)} = d\sigma_{ii}/d\epsilon_{ii}$ , were calculated both in the direction of the major ( $\sigma_1 = \sigma_{22}$ ) and minor ( $\sigma_2 = \sigma_{11}$ ) principal stresses.

The same simulation was performed on a second random array of 531 moderately unequal quartz spheres, having a ratio of radii,  $R_1/R_2 = 1.5$ . In this array 168 spheres had a radius  $R_1$  and 363 had a radius of  $R_2$ . The relation of sizes was set to 1.5 so that the Mindlin–Deresiewicz theory at the contact could be approximately applied by using the concept of "equivalent radius". This equivalent radius,  $R_e = R_1 R_2 / (R_1 + R_2)$ , where  $R_1$  and  $R_2$  are the radii of the particles in contact, has been used in the past in the case of unequal cylinders (Poritsky 1950). It is derived from the Hertz (1882) theory for smooth spheres ( $f=0$ ) and can be applied to the case of rough spheres as a first approximation (Ng 1989).

The above array was first subjected to isotropic pressure,  $\sigma_0 = 132$  KPa; the corresponding geometrical and statistical information is given in Figs. 39 and 40. As the spheres now are not identical there is no crystalization and the 531 sphere aggregate is almost isotropic. Therefore, this 531 spheres arrays exhibits a higher level of symmetry than the 477 equal spheres arrays and can be assumed to be isotropic.

The array was then loaded under biaxial compression to  $\sigma_{22} = 332$  KPa while keeping  $\sigma_{11}$  constant. The array configuration and the distribution of the contact forces at the end of loading are shown in Fig. 41; the corresponding micromechanical information is shown in Fig. 42. This simulation was run for the same reasons as with the 477–sphere array, and also in order to generalize the earlier findings for the case of unequal spheres.

The constrained moduli were again calculated at different values of  $K = \sigma_{11}/\sigma_{22}$ . The normalized constrained moduli,  $D_{11}^{(K)} / D_{11}^{(1)}$  from this simulation, as well as of the simulations on the 477 equal sphere array, appear in Fig. 43, where they are plotted against the stress ratio,  $K = \sigma_{22}/\sigma_{11}$ . Figure 43a contains the

values of  $D_{11}^{(K)}/D_{11}^{(1)}$  spheres in the direction of the increasing principal stress ( $\sigma_{22}$ ), while Fig. 43b contains the normalized moduli in the other direction, in which the stress ( $\sigma_{11}$ ) is kept constant. Both figures also include data points from a number of experiments on sand (squares) performed at the University of Texas by Kopperman et al (1982), as well as the results of the nonlinear finite element simulations of Section 2.6.

The agreement between all normalized results in Fig. 43 is quite good and a straight line of equation  $D_{22}^{(K)}/D_{22}^{(1)} = (\sigma_{22}/\sigma_{11})^{0.38} = K^{0.38}$  could be fitted to all numerical and experimental data points included in Fig. 43a. It should be noted that, if the change in sand density as  $K$  increases is neglected,  $D_{22}^{(K)}/D_{11}^{(1)} \approx [V_p^{(K)}/V_p^{(1)}]^2$ . Using the results of the experiments of Kopperman et al (1982) in sand one computes  $D_{22}^{(K)}/D_{22}^{(1)} \approx K^{0.4}$ , which is very similar to the line in Fig. 43. Therefore, the results of the experiments performed at the University of Texas, that the P-wave velocity ( $V_p = \sqrt{D/\rho}$ ) propagating along a principal stress direction is in first order approximation only a function of that principal stress, is fully predicted by all numerical techniques developed as part of this research.

To further demonstrate the fact that the P-wave propagation velocity (or the constrained modulus) is only a function of the principal stress in the direction of wave propagation, and not of the mean stress  $\sigma_0$ , the 477 equal sphere array was subjected to a biaxial compression-extension loading simulation under constant mean stress,  $\sigma_0 = 91$  KPa. The vertical stress  $\sigma_{22}$ , was increased from 91 to 137.4 KPa, while the horizontal stress,  $\sigma_{11}$ , was decreased from 91 to 44.7 KPa. Thus  $\sigma_0 = 0.5 (137.4 + 44.7) = 91$  KPa at the end, equal to the initial value of  $\sigma_0$ . Again the normalized constrained moduli,  $D_{11}^{(K)}/D_{11}^{(1)}$  were computed at specific values of the stress ratio,  $K = \sigma_{ii} / \sigma_0$  in both directions  $\sigma_{11}$  and  $\sigma_{22}$ , and are

plotted versus the stress ratio,  $K$  in Fig. 44. If the moduli were a function of the mean stress, the P-wave velocity (and modulus in that direction) would be unaffected by the changes in the magnitude of the principal stresses and the results would plot as a horizontal straight line  $D_{ii}^{(K)}/D_{ii}^{(1)} = 1.0$ . This is not the case, however, and the moduli either decrease or increase together with the change in the magnitude of stress in that particular direction. Therefore, Fig. 44 confirms that the constrained moduli,  $D_{ii}$ , are affected by the principal stress in the direction of loading only and are not by the mean stress.

Based on the results of the distinct element micromechanical numerical simulations presented herein, it is concluded that changes in the structure of the random packings and granular soils are responsible for the observed macroscopic behavior, and specifically for the dependence of the P-wave velocity only on the principal stress in the direction of wave propagation. Under isotropic compression (Figs. 36, 37, 39, and 40), the orientations of the contacts have a more or less uniform distribution, the material behaves isotropically and the wave propagation velocity is a function of the isotropic stress,  $\sigma_0$ . Under biaxial (2-D, see Figs. 41 and 42) or triaxial (3-D) compression, a significant number of contacts is gained in the direction of the increased major principal stress,  $\sigma_1$ , while contacts are lost in all non-principal directions. These contacts along principal directions form "branches" or "stiff chains" parallel to the principal stresses which transmit most of the applied principal stresses from periodic "boundary" to periodic "boundary", see also Cundall and Strack (1983). The result is a structure reminiscent of a simple cubic array loaded by stresses  $\sigma_1$ ,  $\sigma_2$  and  $\sigma_3$  parallel to the main axes of the array, and with the effect of each principal stress being more or less uncoupled from the other two. This uncoupling, which in the simple cubic array happens naturally due to the geometry



of the array, develops in the random arrays as a consequence of these stiff columns or "branches" of particles which carry the applied load. Therefore, as in the case of the simple cubic array of Section 2, the longitudinal modulus,  $D$ , in any principal direction is a function only of the stress in this direction and is unaffected by variations in the stresses in the other directions. Although the CONBAL-2 simulations discussed herein are two dimensional, the authors postulate that the same phenomenon occurs in three-dimensions with the formation of "stiff chains" in three directions instead of two. It has been shown (Deresiewicz 1958, 1958a, Petrakis and Dobry 1986), that the shear moduli of the simple cubic array depend only on two principal stresses and are independent of the third principal stress. Since the moduli of the random arrays are expected to be of similar nature due to the 3-D "stiff columns" just discussed, it is believed that this is the reason why the shear moduli (or S-wave velocities) have been observed experimentally to depend only on the principal stresses in the direction of wave propagation and particle motion. However, this hypothesis could not be verified with the 2-D simulation shown and further work needs to be done once the 3-D version of CONBAL is developed.

Despite the limitations of CONBAL-2 discussed above (2-D instead of 3-D, no particle rotation), the results presented in the previous section and by Ng (1989) show that the program is a powerful tool for simulating the monotonic and cyclic behavior of sand. Therefore, it will also be used to investigate the validity of the assumptions regarding the possible distortion of the shape of the soil yield surface presented in Section 1.1.

The next two sections present a combined effort including laboratory and numerical experiments aimed at defining the necessary parameters of a constitutive

law for granular media, while Section 5 discusses the main features such law must have in order to reflect the observed macroscopic behavior. These parameters include the initial and subsequent shape of the yield surface(s), the hardening and flow rules, etc. Both the laboratory and numerical experiments supplement each other as they correspond to similar materials and stress paths. The numerical simulations provide micromechanical information not available from the experiments, providing additional insight and helping in the interpretation of the macroscopic data.

### 3. EXPERIMENTAL STUDY

The main objective of this experimental work is to determine the hardening characteristics of the yield surface(s) of a granular medium after experiencing various load histories. For this, a number of experiments were performed along specific stress paths on hollow cylindrical specimens composed of glass beads. These stress paths are similar to those used by Phillips et al. (1972) in the experimental study of the yield behavior of aluminum discussed in Section 1.2. Since the concept of yield surface or yield function is central to plasticity theory, the shapes of the initial yield surfaces were defined and measured on distinct but identical specimens. As a second step, the motion and the shapes of these yield surfaces after loading were also obtained by a series of cyclic experiments run on the same specimen.

As discussed in Section 1.3, even at constant pressure soils have different yield characteristics than metals, with the most important difference being the absence of a clearly defined elastic region. While it is possible to define an initial yield surface through the threshold strain (for example the locus of all points at which irreversible volumetric or pore water pressure changes start to occur), this is difficult to implement in the laboratory. An alternative is to define the yield surface as the locus of all points having a certain value (close to the threshold but above it) of the octahedral shear strain; this approach was recently adopted by Peters (1988) and will also be used in this study.

The experiments were performed on long thin hollow cylindrical specimens made out of glass beads. Each specimen was first consolidated isotropically by having the same internal and external pressure,  $\sigma_c (= \sigma_o)$ , and then was subjected to shear by a combination of axial and torsional loads, always in drained condition,

using a computer-controlled axial/torsional servohydraulic device. In any given test, the mean stress was kept constant and equal to the consolidation pressure during the shear stage. Therefore, all experimental data from the test are on one  $\pi$ -plane in stress space.

### 3.1 Laboratory Equipment

The tests were performed in RPI's Class of 1933 Earthquake Engineering and Cyclic Loading Laboratory. This laboratory houses the MTS axial/torsional closed loop servohydraulic device which is connected to a digital computer. The computer is a MACSYM-2 computer made by Analog Devices. It is built around the 8086 Intel chip and uses a 16-bit bus and the Intel 8087 co-processor for computing. At the front end it has a 8088 chip for fast data acquisition and control from ten available channels. Figure 45 sketches the configuration of this computer driven axial/torsional apparatus.

The axial/torsional MTS system can perform cyclic tests in both axial and torsional modes, alone or combined. Each mode can be applied either monotonically or cyclically, in stress or strain control.

The applied load is monitored by a load cell which can detect changes in the axial force of  $\pm 0.445 \times 10^{-2}$  KN. The axial deformation of the specimen is measured by an LVDT located at the top of the loading piston. The resolution of the LVDT is  $\pm 0.635 \times 10^{-4}$  m Full Scale Output (FSO).

The applied torque is measured by a torsional load cell which is able to distinguish changes in the torque in the order of  $\pm 0.565 \times 10^{-4}$  KN-m. The rotation is measured by an RVDT which is also located at the top of the loading piston. The resolution of the RVDT is  $\pm 0.05$  degrees FSO.

The volumetric changes are measured by an WF17038 automatic volume change apparatus. This device measures the changes in the position of a brass piston incorporating a Bellofram rolling diaphragm. Volumetric changes on the order of  $\pm 0.05$  cc can be measured.

The cell pressure is measured by a pressure transducer which is connected to the cell the bottom of the triaxial cell. The resolution of the pressure transducer is  $\pm 1.03$  KPa FSO.

The signals from the previously described devices are transmitted using six different channels to the MACSYM-2 computer through a Analog/Digital converter; its resolution for the particular gain used in these tests, was  $\pm 4.88$  mV. The computer performs all appropriate calculations and sends signals to keep the mean stress constant by changing the cell pressure. This is achieved by transmitting the signals through the Digital/Analog converter to Electropneumatic Regulator NIT200. This regulator is capable of implementing cell pressure changes of  $\pm 0.14$  KPa within a pressure range from 0 to 120 KPa.

### 3.2 Specimen Properties

Glass beads were used in the hollow cylindrical specimens. Glass beads were used instead of natural sand to investigate the yield surfaces of granular media, in order to minimize the variability in geometric properties which may influence the results, and in order to compare with the numerical simulations using program CONBAL-2. The glass beads are manufactured by Potters Industries Inc, New Jersey, and are made from soda-lime glass.

The specific gravity of the glass spheres is 2.45 to 2.50 and their minimum roundness is 70%. The Young's modulus is  $E_s = 68.97 \times 10^6$  KPa, the Shear Modulus  $G_s = 29.66 \times 10^6$  KPa, and the Poisson's ratio,  $\nu_s$ , is 0.21. The static coefficient of friction is 0.9 to 1.0 and the dynamic coefficient is 0.7 to 0.8. The coefficient of friction as measured by Chen (1986) is 0.15. Table 3 summarizes the properties of the material used.

The hollow cylindrical specimens had an outside diameter,  $D_o$ , of 7.11 cm and an inside diameter,  $D_i$ , of 5.08 cm, and were 13.97 cm tall, as shown in Fig. 46. These dimensions satisfy the criteria for stress uniformity in such specimens proposed by Wright et al. (1978) and DeNatale and Vrymoed (1981):

$$R_i/R_o \geq 0.65 \quad (37)$$

$$H \geq 5.44 \sqrt{R_o^2 - R_i^2} \quad (38)$$

where  $R_i$  and  $R_o$  are the inside and outside radii of the hollow cylinder, respectively.

All specimens were prepared by the dry tamping undercompaction technique (Ladd 1978) using eight layers 1.27 cm thick. The undercompaction value of the bottom layer was chosen equal to 5%. Undercompaction was used instead of other alternative techniques because it produces uniform samples which can be easily reproduced (Baziar 1987).

Once the specimen was completed, it was placed in the triaxial cell which was filled with deaired water to prevent migration of air through the specimen membrane. After this the specimen was percolated upwards with  $CO_2$  to eliminate air, and was then saturated with deaired distilled water and backpressured overnight to ensure good saturation.

The next day the B parameter was measured, and then the cell with the specimen was placed in the MTS axial/torsional device.

### 3.3 Testing Program

The testing program consisted of a series of monotonic tests and of another series of cyclic tests. The monotonic tests were used to classify the material based on its monotonic stress-strain behavior under various inclinations of principal stress, while the cyclic tests were used to define the yield surfaces (Kotsanopoulos 1989).

The specimens were composed of a mixture of sieve 40-50 (0.43 to 0.3 mm) and sieve 60 - 80 (0.25 to 0.18 mm) glass beads with ratio 1:2 in weight. The grain size distribution of this material appears in Fig. 17. A mixture was used instead of

one size of spheres as a result of instabilities and sliding which occurred during monotonic tests of specimens composed of identical particles. It appears that these instabilities and sliding are the result of regular packings and crystalline regions which are present in assemblages of equal spheres, but not necessarily in assemblies of particles of unequal diameters. All specimens were prepared by the same technique described in Section 3.2 and their initial void ratio,  $e$ , was the same in all tests. In both monotonic and cyclic tests, the mean stress,  $\sigma_c$ , was kept constant during loading by changing the cell pressure accordingly. Therefore, each experiment corresponds to a single  $\pi$ -plane defined by this  $\sigma_c$ .

Five drained monotonic radial shear tests were performed as listed in Table 3. In three of these tests, the specimens were isotropically consolidated to  $\sigma_c \cong 140$  KPa, while the fourth specimen was consolidated to 277 KPa and the fifth to 414 KPa. For each of the three radial shear tests performed at  $\sigma_c \cong 140$  KPa, the principal stress formed a constant angle  $\omega$  with respect to the vertical direction, with  $\omega = 0^\circ, 45^\circ$  and  $90^\circ$ . These correspond to vertical compression, torsional, shear, and vertical extension, respectively. In all tests the mean stress was kept constant at the  $\sigma_c$  of the test ( $\cong 140$  KPa). The other two tests were performed in compression ( $\omega = 0^\circ$ ). The test conditions and stress parameters of each monotonic test are summarized in Table 4.

The two last columns of Table 4 include the angle of shear direction,  $\theta$ , and the coefficient  $b$  used in the five tests. The angle  $\theta$  defines the direction of the octahedral shear stress in the octahedral plane and is given by  $\tan \theta = [3(\sigma_2 - \sigma_3)/(2\sigma_1 - \sigma_2 - \sigma_3)]^{1/2}$ . The coefficient  $b$  gives the relative magnitude of the intermediate principal stress  $\sigma_2$ , and is defined as  $b = (\sigma_2 - \sigma_1)/(\sigma_3 - \sigma_1)$ .



The results from the monotonic tests performed at  $\sigma_c \cong 140$  KPa appear in Figs. 48 and 49. Figure 48 portrays the stress-strain curves ( $\tau_{oct}/\sigma_c$  vs  $\gamma_{oct}$ ) obtained from these tests; it can be seen that while all stress paths give different peak strengths, the shear test ( $\omega=45^\circ$ ,  $\theta=30^\circ$ ) has also a different initial stiffness; this suggests that the material is not isotropic. Figure 49 presents the measured volumetric strain as a function of the octahedral shear strain, and here again, the behavior is different depending on the stress path followed.

The resulting stress-strain curves from three monotonic compression tests at  $\sigma_c = 136.8$ , 277. and 414.1 KPa appear in Fig. 50, and the volumetric behavior is shown in Fig. 51. Another interesting plot is the variation of octahedral shear stress ( $\tau_{oct}$ ) with volumetric strain, which appears in Fig. 52; plots like this are used in constitutive law modelling, since they indicate at which stress level volumetric strain starts to accumulate.

### 3.4 Experimentally Obtained Yield Surfaces

As discussed previously, granular media exhibit nonlinear inelastic stress-strain behavior even at very small strains. Thus, cohesionless aggregates do not have a clearly defined elastic region, and as a result each initial yield surface can not be defined the way it is done in metals; as the locus of all points beyond which plastic deformation occurs. To assume a mathematical model of the type proposed by Mroz (1967) or Prevost (1978), which describes the nonlinear behavior of materials by a number of yield surfaces associated with a constant elastoplastic modulus would link the results of this research to a specific type of model and would

also be very difficult to achieve in the laboratory. Consequently, a yield surface was not defined here as the locus of all points with a constant elastoplastic modulus. Instead, the yield surface was defined as the locus of all points in stress space ( $\tau_{z\theta}$ ,  $(\sigma_{zz} - \sigma_{rr})/2$ ) having the same total octahedral shear strain  $\gamma_{oct} = 0.05\%$  or  $0.10\%$  in monotonic tests. This definition of yield surface is similar to that used by Sture et al. (1987) for studying the yielding characteristics of sand.

Figure 53 sketches the initial yield surface obtained from the hollow cylindrical tests on glass beads described in the previous section. Each point of the yield surface corresponds to a different drained monotonic radial shear test conducted on a new specimen.

Then, two series of two reversible (cyclic) experiments each were conducted in order to define the hardening characteristics of the yield surface when the specimen is prestrained in: i) compression, and ii) shear (torsion). The test conditions and stress parameters of each reversible test are summarized in Table 5. The sequence of loading paths for these tests is shown in Fig. 53, where the numbers may be followed to identify the applied stress path. Each specimen was prestressed to point  $R_x$  ( $x = a, t$ ) in stress space which is called the "Reference" point. Then the load was increased until a change in octahedral strain of  $0.05\%$  was detected (points 1 in Fig. 53), whereupon the load was reversed to  $R_x$  and then further decreased to point 3, defined by  $|\gamma^{(R_x)} - \gamma^{(3)}| = 0.05\%$ . This probing procedure was repeated in different directions until all indicated points on the yield surface had been defined (see Fig. 53). Throughout the experiment, the mean stress was kept constant. Since this procedure cannot be implemented manually, a data acquisition/control software was developed to control the above experiments, and the corresponding flowchart is shown in Fig. 54.

As described above, stress increments such as used above (for example to go from points 1 to 3 in Fig. 53) were either a torsional or a compression increment depending on the test, and torsion and compression increments were not applied simultaneously, so as not to distort the shape of the yield surface. While it is true that in order to reach a yield surface a stress must be applied which may cause the yield surface to slightly displace or distort, the stress paths described above minimize this effect by cancelling it (e.g., stress path 9-10-11-12 in Fig. 53). This occurs because the yield surface is expected to be symmetric about either the horizontal deviatoric stress or the shear axis, depending on the test. This procedure is different from that employed by Peters (1988), in which the yield surface is determined by radial stress paths on different specimens, and from that followed by Phillips et al. (1972), see Fig. 5. On the other hand, it is very similar to that utilized for composite materials by Dvorak et al. (1988).

One important decision in this work was to use the prestress point  $R_x$  as the "reference" point from which all stress probes start. Dvorak et al. (1988) used the same technique, but started the stress probes from the midpoint between points 1 and 3 (Fig. 53) in stress space. Point 3, as well as all other points on the yield surface was defined by Dvorak et al. as the point at which nonlinearity starts. Soils, however, do not have a linear region beyond which permanent deformations occur, and thus another criterion must be used to select the reference point, which is critical because it controls the shape of the yield surface. Prestress point  $R_x$  was chosen herein for reference because it is the prestraining to this point which controls the subsequent yielding behavior of the specimen. Therefore, it was decided to start all stress probes from point  $R_x$  in stress space. If soils had a clearly defined linear elastic and plastic regions, this method would coincide with that of Dvorak et al.

(1988). Although point  $R_x$  remains more or less in the same position in stress space, there is permanent deformation associated with these cyclic stress paths. Unfortunately, this is a result of the properties of the specimen, and little can be done other than keeping the strains as small as possible. On the other hand, if a multiple yield surface model is envisioned, these stress paths would correspond to the stress probes needed to define any of the nested yield surfaces. This yield surface would then be analogous to those of Mroz (1967) or Prevost (1978), since it would also map a state of the material on a parameter, in this case  $\gamma_{oct}$ .

Figures 55 and 56 summarize the initial and subsequent positions of yield surfaces defined from monotonic and cyclic tests with  $\sigma_c \approx 140$  KPa. A total of four cyclic tests were performed; in all of them the mean stress was kept constant and equal to the initial confining pressure,  $\sigma_c \approx 140$  KPa. Therefore all experimental data lie on this  $\pi$ -plane. Of these four tests, two were prestrained in shear while two were prestrained in compression. In the first series of experiments, the yield surface was defined as the locus of all points with  $\gamma_{oct} = 0.1\%$ . In the second series of experiments the strain level defining the yield surface was reduced to 0.05%. A further reduction of the strain level is anticipated in the future, so as to approach the threshold strain,  $\gamma_r \approx 1.0 \times 10^{-4}$  to  $2.0 \times 10^{-4}$ , as close as possible. The specimens of the second series of the experiments were also subjected to 600 cycles of torsional shear strain amplitude  $\gamma_{z\theta} = 0.07\%$  in strain-control under drained conditions prior to the actual experiment. This was done to reduce the inherent anisotropy created during the sample preparation and to stiffen the sample on horizontal planes. However, it was found that this neither stiffened nor disturbed the specimen.

The results of the first series of tests appear in Fig. 55. The yield surfaces are defined as the loci of all points with  $\gamma_{oct} = 0.1\%$  and were obtained by prestraining

one sample in torsion to  $\gamma_p = \gamma_{oct} = 0.3\%$  and the other sample in compression to  $\gamma_p = \gamma_{oct} = 0.79\%$ . In the second series of the experiments the strain yield criterion was reduced by 50%, to  $\gamma_{oct} = 0.05\%$  (Fig. 56). One sample was prestrained in shear (torsion) to 0.3% and a second sample was prestrained in compression to  $\gamma_{oct} = 0.5\%$ . In both series of tests  $\sigma_c$  was kept constant at about 140 KPa.

The results suggest a significant prestraining effect and distortion of the chosen yield surface in the direction of loading. The size of the yield surface has decreased in size in the direction of prestraining, while in the other direction the size remains essentially unchanged. Moreover, it is observed that the yield surface translated in stress space. These findings are important, since the usual hypothesis of pure kinematic hardening would have predicted that the new, translated yield surface size would be the same as before.

Finally a "failure" surface was constructed out of all monotonic tests; this surface is shown in Fig. 57, where the deviatoric stress  $q = (\sigma_1 - \sigma_3)/2$  is plotted versus  $p = (\sigma_1 + \sigma_3)/2$ . The shape of this failure surface can be approximated as conical. It is reasonable to expect that this failure surface must be very similar to the yield surfaces.

These two series of cyclic experiments are in excellent agreement between themselves; moreover, they are in general qualitative agreement with results obtained in other materials such as  $\pi$  and metal matrix composites. Since the common plastic deformation mechanism between polycrystalline aggregates and granular assemblies is sliding taking place along sliding planes, it is believed that these observed results are a consequence of those sliding mechanisms occurring at the micromechanical level.

#### 4. NUMERICAL SIMULATIONS

In order to confirm the experimental results presented in Section 3 and to gain insight into the micromechanical processes occurring at the contact level, a series of 2-D numerical simulations was performed using program CONBAL-2, along stress paths very similar to the experimental ones, on the random array of 531 unequal spheres presented in Section 2.7. This array was used since the glass beads tested in the laboratory was composed of spheres of different diameters.

The stress paths followed are very similar to those of the laboratory experiments presented in Fig. 53, with two minor differences: i) the octahedral strain used as the yield criterion was first set to  $\gamma_{oct}=0.05\%$  and was later reduced to 0.02%, which is very close to the threshold strain,  $\gamma_t$ ; and ii) the numerical simulations were strain controlled, thus all points were defined in strain space. Because of the two-dimensional nature of the numerical simulations, qualitative rather than quantitative agreement between the simulations and the laboratory experiments was sought. These two differences between numerical simulations and laboratory experiment are not very important, and if anything, the smaller  $\gamma_{oct}$  used in the simulations are better, since a smaller  $\gamma_{oct}$  is closer to the threshold strain and thus defines a region near the cut-off point between permanent geometrical changes and effects due to sliding taking place at the contacts.

The 531 quartz array was consolidated to 130 KPa; the particle configuration and the micromechanical statistics at this stage were presented in Figs 39 and 40. Then, two series of calculations simulating four tests on four initial identical specimen were conducted in which the array was prestrained in: i) compression to two different strain levels, and ii) in shear to two different strain levels. All four

"specimens" were prestrained first to  $\gamma_{oct}=0.98\%$  and subsequently to  $\gamma_{oct}=2.33\%$ . The mean stress was kept constant in all cases at  $\sigma_c=130$  KPa throughout each simulation.

Figure 58 portrays the results of the simulations which defined the yield surface as the locus of all points with  $\gamma_{oct}=0.05\%$ . There are five yield surfaces in this figure, the circular one being the initial surface which was defined by four monotonic tests. The "subsequent" yield surfaces correspond to prestraining to two strain levels,  $\gamma_p = \gamma_{oct} = 0.98\%$  and  $2.33\%$  as marked. It can be seen that there is a significant change in the shape of the prestrained yield surface: it has shortened in the direction of loading while its dimension in the other direction has not changed. Moreover, this shrinking of the yield surface increases with increasing prestraining. Finally, the surface became flatter in the direction opposite to the direction of loading. These results are very similar to those obtained in the laboratory experiments on glass beads (Figs. 55 and 56) and to those obtained in other materials by various researchers (Fig. 59).

Figure 60 portrays the results of the numerical simulations where the magnitude of the octahedral shear strain defining the yield surface was  $\gamma_{oct} = 0.02\%$ . The results are again very similar to those of the simulation in Fig. 58, to the laboratory experiments on glass beads (Figs. 55 and 56) and on other materials (Fig. 59). The fact that the yield surfaces defined by  $\gamma_{oct}=0.02\%$  are quite similar in size to those defined by  $\gamma_{oct}=0.05\%$  suggests that at these strain levels the granular material behaves more or less elastically. Moreover, it has been shown (Ng 1989) that there are very small permanent volumetric changes in these numerical simulations at a strain level of  $0.02\%$  or less, which confirms the fact that

the effects of the distortion of the yield surfaces observed is not a consequence of accumulated strain, but rather a result of sliding and other micromechanical phenomena occurring at the particle level.



## 5. PROPOSED CONSTITUTIVE LAW FOR GRANULAR MEDIA

This section presents the main features of a proposed constitutive law for granular media using the results presented in this report. Given the limitations of the existing constitutive laws as discussed in Section 1.1, the authors have taken a different approach to the formulation of a constitutive law for dry granular soil. This approach has as a starting point the micromechanical force-deformation contact law obtained by Seridi and Dobry (1984) and Dobry et al. (1989). In that contact model, there is an infinite number of yield surfaces of conical shape, all parallel to each other at all times. A stress-strain equivalent of this force-deformation contact law will be used for the proposed constitutive relation of granular media, modified to incorporate additional important features observed in granular soils.

The model is based on the results of the laboratory experiments presented in Section 3, enhanced by the numerical simulations discussed in Section 4. The proposed model uses the most important features of the contact law (Dobry et al. 1989) and is capable of incorporating the distortion of the shape of the yield surfaces due to loading, previously discussed.

Since the contact model was naturally formulated in terms of forces, the mathematical formulation used as the basis of the proposed constitutive law is the viscoplasticity model presented by Yen (1979) and Yen and Eisenberg (1987), but without the rate effects. This model must be modified to make it dependent on the mean stress,  $\sigma_c = p = \sigma_{ii}/3$ , and the hardening and flow rules must be changed to match those of the contact law as well as the experiments. The yield surfaces are initially conical, and they are permitted to distort in the direction of loading as

observed in the experiments and numerical simulations (Figs. 55, 56, 58, and 60). The flow rule is associative only on the deviatoric plane and the hardening rule allows for parallel translation of the yield surfaces in a way similar to that of the contact model.

The main aspects of the proposed constitutive law are summarized below. In 3-D stress space, the initial deviatoric stress state,  $S_{ij}$ , is referred to the subsequent state,  $s_{ij}$ , through:

$$S_{ij} = s_{ij} - \alpha_{ij} + R_{ij} \quad (39)$$

where  $s_{ij}$  is the deviator stress,  $\alpha_{ij}$  the location of the center of any given yield surface (there is a large number or even an infinite number of them) in deviatoric stress space, and  $R_{ij}$  is a measure of the distortion of this yield surface. The term  $R_{ij}$  does not appear in the force-displacement contact model, since the yield surfaces were not allowed to distort; it is used here for the first time, in an attempt to present a model which is general enough to be modified to take into account the distortion of the yield surfaces. Usually,  $R_{ij}$  is a function of the previous deviatoric stress state,  $S_{ij}$ , and of the history of material deformation (Eisenberg and Yen 1984). Assuming a yield function  $F$  of the same form as the micromechanical contact law (Dobry et al. 1989), it will be:

$$F = \frac{1}{2} (s_{ij} - \alpha_{ij} + R_{ij})(s_{ij} - \alpha_{ij} + R_{ij}) - m^2(p - p_i)^2 \quad (40)$$

where  $m$  is a material constant related to the friction angle of the soil and defined through laboratory experiments,  $p = \frac{1}{3} \sigma_{ii}$  is the value of the hydrostatic stress for a

point on the cone, while  $p_i$  is the hydrostatic stress at the apex of the same cone. Figure 61 presents several conical yield surfaces and a deviatoric plane ( $\pi$  - plane) in principal stress space. Figure 62a shows the intersection of one of these yield functions with a  $\pi$  - plane, which portrays the simultaneous translation (kinematic hardening) and distortion of the resulting yield circle. Figure 62b defines the corresponding distortion term  $R_{ij}$  used in Eq. 40.

If the distortion term,  $R_{ij}$  is eliminated, the yield function reduces to

$$F = \frac{1}{2} (s_{ij} - \alpha_{ij})(s_{ij} - \alpha_{ij}) - m^2 (p - p_i)^2 \quad (41)$$

which is the exact stress equivalent of the micromechanical force-displacement contact law (Dobry et al. 1989).

The flow rule is described by:

$$d\epsilon_{kl}^p = \frac{3}{2 H_p} (d\sigma_{ij} n_{ij})(n'_{kl} + \delta_{kl} u''_{mm}) \quad (42)$$

where  $H_p$  is the plastic tangent modulus. In Eq. 42,  $n'_{ij}$  is the deviatoric part of the normal vector to the yield surface,  $n_{ij}$ , and  $u''_{mm}$  is the spherical part of another vector  $u_{kl}$ , so that normality is observed only on the deviatoric plane. An example of the form of  $u''_{mm}$  is given by Prevost (1985):

$$u''_{mm} = \frac{1}{3} \frac{(\eta/\bar{\eta})^2 - 1}{(\eta/\bar{\eta}) + 1} \quad (43)$$

where  $\eta = \frac{3}{2} (s_{ij} s_{ij})^{1/2} / p$  is a stress ratio, and  $\bar{\eta}$  is a material parameter. Therefore, this observation of normality only on the deviatoric plane is a characteristic of the micromechanical constitutive law, as well as of a number of other models.

The hardening and distortion parameters,  $\alpha_{ij}$  and  $R_{ij}$ , can be either determined a priori or from a combination of results of micromechanical simulations and laboratory experiments. The exact form of these parameters is not currently known for the case of sand, but without loss of generality it can be assumed that

$$\dot{\alpha}_{ij} = \dot{\mu} v_{ij} \quad (44)$$

$$\dot{R}_{ij} = -\dot{\lambda} u_{ij} \quad (45)$$

where  $v_{ij}$  and  $u_{ij}$  are tensors defining the specific direction of hardening, and  $\mu$  and  $\lambda$  are scalars defining the magnitude of the hardening mechanism. If a finite number of yield surfaces is used in the model, the kinematic hardening direction,  $v_{ij}$ , can be defined in a number of ways including those proposed by Prager (1955), Ziegler (1958), Mroz (1967), and Phillips and Weng (1975). However, if functions defining an infinite number of yield surfaces are used such as done in the contact law, no such rule is necessary. The two scalars,  $\mu$  and  $\lambda$ , are related to each other through the consistency condition.

Yen (1979) and Yen and Eisenberg (1987), using the results from experiments by Phillips and his coworkers have defined both  $\alpha_{ij}$  and  $R_{ij}$  and used them successfully in a constitutive law for aluminum. The excellent agreement between theory and experiment in the case of cyclic loading of aluminum is shown in Fig. 63,

where the discrete points correspond to the laboratory data and the solid lines to the model.

As already noted, the above proposed stress equivalent model to the contact law summarized by Eqs. 39–45 has a number of advantages over the existing plasticity models for sand, while still lacking in some respects. The advantages include its foundation on basic micromechanical features such as the behavior at the interparticle contacts, and its ability to model a number of important observed macroscopic features such as the pressure dependence of stiffness, the generalized Mohr–Coulomb failure law and the basic hardening behavior during cyclic shear loading. Also, as already mentioned and included in Eq. 40, the model can incorporate the distortion of yield surfaces due to prestraining. Moreover, the micromechanical basis of the model allows it to be compared directly with the contact model through numerical simulations on random packings of spheres, so that the model can be adjusted at the macroscopic level with due consideration to the underlying micromechanical phenomena.

On the other hand, in its present state the basic model of Eqs. 39–45 still misses some features which have been observed in sands. The proposed law does not model the dilation  $\epsilon_v'$  observed in medium and dense granular soils for shear loading contained in the  $\pi$ -plane, and it does not account for inelastic volumetric strains due to isotropic consolidation, nor for overconsolidation effects. Finally, it does not consider initial (inherent, structural, elastic) anisotropy, which would permit the prediction of the anisotropic wave propagation phenomena reported by Stokoe and his co-workers for anisotropically consolidated sand (Knox et al. 1982, Kopperman et al. 1982).

The dilation can be handled, in principle, by modifying both the hardening and flow rules. Existing models such as Prevost's (1985) account for this by allowing rotation as well as translation of the yield surfaces (Fig. 64). To account for this, the yield surfaces in our proposed model could be permitted to rotate after a certain strain level has been reached, whereupon dilation will occur (Fig. 65). This is consistent with the experimental finding in sand that dilation occurs in medium and dense sand only after a certain strain level beyond the threshold has been reached. On the other hand, the experimental evidence presented in Fig. 52 as well as other observations on sand from the literature suggest that dilation under shear occurs at relatively large strains. Therefore, the flow rule does not have to be modified at small strains.

The inelastic volumetric strains during isotropic consolidation and the response of overconsolidated soil can be obtained with the help of a "cap" (Roscoe et al. 1958, DiMaggio and Sandler 1971, Baladi and Rohani 1979).

The problem of inherent (structural) anisotropy – especially important for anisotropically consolidated sand – is quite complex even in the case of metal plasticity. "Inherent anisotropy" means that the material is anisotropic in its reference state. After plastic flow has occurred, in general, the material ceases to have the anisotropy of the reference state. A very good example is the case of rolled steel; in its stress free state, before rolling, the material is isotropic and its behavior could be described by isotropic functions. After the sheet of steel has been subjected to rolling, it may exhibit orthotropic symmetry, and if this is to be the reference state, the material behavior should be described by orthotropic functions with respect to the new reference state. The case of soil anisotropy is very similar: if the behavior of an anisotropically consolidated sand is to be described, this has to be

done with orthotropic functions. In general, simple solutions applied only to the elastic part of the strain, such as proposed by Hardin (1980), are not appropriate. For example, if the tests of Stokoe and his coworkers are to be taken into account, orthotropic functions are needed for the description of the phenomenon. It is reported by Hill (1950) and Dafalias (1979) that the yield condition must take into account the material symmetries present in the initial (reference) state. The direction of flow is dependent upon those, and the yield surface must take them into account. This not only complicates the expressions of the yield surface considerably, but the implementation of the law as well. For example, according to Dafalias (1979), the expression for the yield condition of an orthotropic material becomes:

$$f = H_{ijkl}S_{ij}S_{kl} - k^2 \quad (46)$$

where  $H_{ijkl}$  is a fourth rank tensor which depends on the material symmetry and the plastic strain and  $k$  is the yield stress. Despite its obvious complexity, the plasticity of initially anisotropic materials can be taken into account in a number of ways for the cases of transverse isotropy and orthotropy. The case of transverse isotropy is very common in the mechanics of composite materials (Dvorak and Bahei-El Din, 1982), and is handled with the aid of four stress "pseudo-invariants" which take into account the symmetries of the material. In the case of soils, Dafalias (1986), Dafalias and Herrmann (1986) and Anandarajah and Dafalias (1986) have proposed a general plasticity model which has been applied to model isotropic and anisotropic clay in undrained condition. The case of drained loading

of sand is more complex, since its behavior is pressure dependent and its material symmetry is affected by variations in the mean stress  $\sigma_{ii}/3$ .



## 6. CONCLUSIONS

The results of a systematic micromechanical study was presented on the stress-strain behavior of granular media, aimed at developing a constitutive law for sands and other granular materials.

As summarized in Table 1, the research focused on the computation of the stress strain response of arrays of rough, elastic quartz spheres of similar sizes simulating uniform, rounded quartz sand. It started from the RPI general solution for the nonlinear force displacement relation at the contact between two spheres (program CONTACT), and it continued with analyses of regular and random arrays of spheres using a variety of analytical and numerical techniques. The research progressed from very small ( $\gamma \approx 10^{-6}$ ) to very large strains ( $\gamma \approx 10^{-2}$  to  $10^{-1}$ ), and it included comparisons at different strain levels between the results obtained with these techniques.

A number of regular arrays of spheres were analyzed, and then they were combined into regular/random arrays to attain arbitrary macroscopic void ratios. These regular/random array models were loaded isotropically and their macroscopic response was evaluated at very small strains by the Self Consistent Method. Then, another regular/random array model was developed and analyzed by a 2D Nonlinear Finite Element method. This Finite Element model was loaded first isotropically and then anisotropically to "failure" (corresponding to the beginning of generalized sliding and particle rearrangement), and it provided information from  $\gamma \approx 10^{-6}$  up to  $\gamma \approx 10^{-4}$ . Finally, 2D numerical simulations of random arrays were implemented using a Nonlinear Distinct Element technique, covering the whole strain range from  $\gamma \approx 10^{-6}$  to  $10^{-1}$ . In addition, comparisons between these calculations and

measurements in sands and other granular materials were performed, including experiments available from the literature and axial-torsional tests on glass beads conducted as part of this research.

It was found that all computational techniques are in very good agreement between themselves as well as with the experimental results. Some specific conclusions for the different strain levels are as follows:

1) In a granular medium isotropically loaded under a given macroscopic pressure, there is a unique relation between the shear stiffness at very small strains ( $G_{\max}$ ) and the average number of load-transmitting contacts per particle, with  $G_{\max}$  increasing with the number of contacts. This was confirmed by all techniques used in the report.

2) In the same isotropically loaded granular medium, the relation between void ratio and  $G_{\max}$  is not unique. For the same void ratio and particle geometric arrangement,  $G_{\max}$  can vary by a factor of three depending on the number of contacts. In a typical sand,  $G_{\max}$  is much smaller than predicted from a regular array or combination of regular arrays having the same macroscopic void ratio as the sand. However, millions of cycles of small strain amplitude ( $10^{-4} < \gamma < 10^{-3}$ ) will increase the stiffness of the sand and make it approach the theoretical value predicted by the Self Consistent method, by increasing the number of contacts while the void ratio stays essentially constant.

3) The P-wave velocity through an anisotropically loaded 2D granular medium depends mainly or exclusively on the principal stress in the direction of wave propagation. This seems to be the result of a specific force transmission mechanism throughout the medium, with the load paths oriented more or less parallel to the directions of the applied principal stresses. In this way, the behavior

of the medium resembles that of a simple cubic array, where the stiffness in a principal direction is not influenced by the stresses in the other direction. This result was confirmed for 2D by both the Nonlinear Finite Element model and the Nonlinear Distinct Element simulations. Based on this analysis and on available experimental results on sand, it is hypothesized that a similar conclusion and force transmission mechanism is also valid in 3D, for both P-wave and S-wave velocities.

4) In the small strain range below the threshold ( $\gamma < \gamma_t \approx 10^{-4}$  for quartz spheres), the shear stress-strain behavior of the medium is controlled by the original arrangement of the grains and by the nonlinear force-deformation response at the contacts, and essentially no rearrangement of particles takes place. Aspects of this small strain behavior including the existence of the threshold were known from previous experimental and analytical research. The Nonlinear Finite Element model confirmed this behavior. It also provided additional insight on the mechanics of small strain response, and on the process which culminates in particle separation and rearrangement when the shear strain reaches the threshold.

5) A major role in the shear stress-strain behavior of granular media is played by sliding taking place between the grains. Available analytical and experimental studies in polycrystalline aggregates such as metals suggest that specific sliding directions at the interparticle contacts control the features of specific portions of the yield surface of the medium in stress space. This was verified with our Nonlinear Finite Element calculations of random/regular arrays of spheres. One corollary of these studies in metals is that the yield surface not only translates due to shear loading but also shrinks and distorts in the direction of loading, forming a smooth vertex at the loading point. This same behavior was observed in our 2D

simulations of random arrays of quartz spheres using the Nonlinear Distinct Element, as well as in our axial-torsional tests on glass beads.

6) A constitutive law for granular media was proposed based on these findings, which is the stress-strain equivalent of the RPI force deformation model for the interparticle contact, enhanced to incorporate dilation for strains above the threshold, and to allow for distortion of yield surfaces in the direction of loading. Basic characteristics of this model include an infinite number of originally parallel yield surfaces of conical shape, as well as modified normality and kinematic strain hardening rules.

## REFERENCES

- ABAQUS (1982), User's Manual, Version 4, Hibbit, Karlsson and Sorensen Inc., Providence, RI.
- Alawi, M.M., Sture, S., and Ko H.-Y. (1988), "True Triaxial and Directional Shear Cell Experiments on Dry Sand," U.S. Army Waterways Experiment Station Report.
- Anandarajah, A., and Dafalias, Y.F. (1986), "Bounding Surface Plasticity. III: Application to Anisotropic Cohesive Soils," *J. Eng. Mechanics*, Vol. 112, No. 12, Dec. pp. 1292-1318.
- Arthur, J.R.F., Cutler, F., Dunstan, T., Ford, J. Leavell, D. A., Peters, J. F. and Pulsford, J. R. (1988), "Design Development and Operation of an Advanced Directional Shear Cell", U. S. Army WES Report.
- Backman, B.F., Brown, C.B., Jowitt, P.W. and Munro, J. (1983), "Statistical Mechanics for Granular Materials," *Advances in the Mechanics and the Flow of Granular Materials*, Vol. I, M. Shahinpoor, Ed., Trans. Tech. Publications, Clansthal-Zellerfeld, Fed. Republic of Germany.
- Baladi, G.Y. and Rohani, B. (1979), "Elastic-Plastic Model for Saturated Sand," *Journal of the Geotechnical Engineering Division*, ASCE, Vol. 105, No. GT4, April, pp. 465-480.
- Baziar, M.H., (1987), "Influence of the Testing Technique on the Steady State Lines of a Sand," M.S. Thesis submitted to RPI, Troy, N.Y.
- Benjamin, J.R. and Cornell, C.A. (1970), Probability, Statistics and Decision for Civil Engineers, McGraw Hill.
- Bernal, J.D. and Mason, J. (1960), "Coordination of Randomly Packed Spheres", *Nature*, Vol. 188, pp. 910-911.
- Bernal, J.D., Knight, K.R. and Cherry, I. (1964), "Growth of Crystals from Random Close Packing", *Nature*, Vol. 202, pp. 852-854.
- Budiansky, B. and Wu, T. (1962), "Theoretical Predictions of Plastic Strains of Polycrystals," *Proc., 4th U.S. Nat. Congr. Appl. Mech.*, pp 1175-1185.
- Budiansky, B. (1965), "On the Elastic Moduli of Some Heterogeneous Materials," *JMPS* 1965, Vol. 13, 223-227.
- Canova, G.R., Kocks, U.F., Tome, C.N., Jonas, J.J. (1985), "The Yield Surface of Textured Polycrystals," *J. Mech. Phys. Solids*, Vol. 33, No. 4, pp. 371-397.
- Cattaneo, C. (1938), "Sul Contatto di Due Corpi Elastici". *Atti Acad. Nazionale dei Lincei*, Serie 6, 27, pp. 342-348, 434-436, 474-478.

- Chen, W.F. (1975), Limit Analysis and Soil PLasticity, Elsevier Scientific Publishing Co., Amsterdam, The Netherlands.
- Chen, Y. (1986), "Experimental Determination of Fabric for Granular Materials," Ph.D. Dissertation, Cornell University, Ithaca, NY.
- Cundall, P. A. and Strack, O. D. (1979), "A Discrete Numerical Model for Granular Assemblies," *Geotechnique*, 29, No. 1, pp. 47-65.
- Cundall, P.A. and Strack, P.A. (1983), "Modelling of Microscopic Mechanisms in Granular Material," Mechanics of Granular Materials: New Models and Constitutive Relations, Jenkins and Satake, editors, pp. 137-149.
- Dafalias, Y.F. and Popov, E. (1976), "Plastic Internal Variables Formalism of Cyclic Plasticity," *Inter. Symp. on Soils under Cyclic Plasticity, Journal of Applied Mechanics*, Dec., pp. 645-651.
- Dafalias Y. (1979), "Anisotropic Hardening of Initially Orthotropic Materials, " *ZAMM*, 59, pp. 437-416.
- Dafalias Y.F., and Hermann, L.R. (1982), "Bounding Surface Formulation of Soil Plasticity," *Intl. Symp. on Soils under Cyclic and Transient Loading*, G. Pande and O.C. Zienkiewicz, eds., Wiley, London, U.K., pp. 253-282.
- Dafalias, Y.F. (1986), "Bounding Surface Plasticity. I: Mathematical Foundation and Hypoplasticity," *J. Eng. Mechanics*, Vol. 112, No. 9, pp. 966-987.
- Dafalias, Y.F., and Herrmann, L.R. (1986), "Bounding Surface Plasticity. II: Application to Isotropic Cohesive Soils," *J. Eng. Mechanics*, Vol. 112, No. 9, pp. 1263-1291.
- Davis, R.A. and Deresciewicz, H. (1977), "A Discrete Probabilistic Model for Mechanical Response of a Granular Medium," *Acta Mechanica*, 27, pp. 69-89.
- DeNatale, J.S. and Vrymoed, J.L. (1981), "Analysis and Stress Distribution in Torsional Shear Testing," *First Conference on Recent Advances on Geotechnical Earthquake Engineering*, Univ. Missouri-Rolla, St Louis, Vol. 1, pp. 145-148.
- Deresciewicz, H. (1958), "Mechanics of Granular Matter," *Advances in Applied Mechanics*, V, 233-306, New York: Academic Press Inc.
- Deresciewicz, H. (1958a), "Stress-Strain Relations for a Simple Model of a Granular Medium," *J. Appl. Mech.*, Trans. ASME, Sept., 402-406.
- DiMaggio, F.L. and Sandler, I.S. (1971), "Material Model for Granular Soils," *Journal of the Engineering Mechanics Division*, ASCE, Vol. 97, 935-950.

- Dobry, R., Ladd, R., Yokel, F.Y., Chung, R.M., and Powell, D. (1982), "Prediction of Pore Water Pressure Buildup and Liquefaction of Sands During Earthquakes by the Cyclic Strain Method," Building Science Series 138, National Bureau of Standards.
- Dobry, R., Ng, T., Petrakis, E. and Seridi, A. (1989), "An Incremental Elastic-Plastic Model for the Force-Displacement Relation at the Contact Between Two Spheres," submitted for publication to the *Journal of Engineering Mechanics*, ASCE.
- Drnevich, V.P. (1967), "Effects of Strain History on the Dynamic Properties of Sand," Ph.D. Dissertation, University of Michigan, Ann Arbor, MI.
- Drucker, D.C. and Prager, W. (1952), "Soil Mechanics and Plastic Analysis or Limit Design," *Quarterly of Applied Mathematics*, Vol. 10, 157-165.
- Drucker, D.C. and Palgen, L. (1981), "On Stress-Strain Relations Suitable for Cyclic and Other Loading," *J. Appl. Mechanics*, September, pp. 479-485.
- Duffy, J. and Mindlin, R.D. (1957), "Stress-Strain Relations of a Granular Medium," *J. Appl. Mech.*, Trans. ASME, Dec., 585-593.
- Duffy, J. (1959), "A Differential Stress-Strain Relation for the Hexagonal Close-Packed Array of Elastic Spheres," *J. Appl. Mech.*, **26**, 88-94.
- Dvorak, G.J. and Bahei-El-Din, Y.A. (1982), "Plasticity Analysis of Fibrous Composites," *Journal of Applied Mechanics*, Vol. 49, June, pp. 327-335.
- Dvorak, G.J. (1987), "Plasticity of Fibrous Composites," Report to U.S. ARO, Dept. Civil Engineering, Rensselaer Polytechnic Institute, Troy N.Y.
- Dvorak, G.J. Bahei-El-Din, Y.A., Macheret, Y. and Liu, C.H. (1988), "An Experimental Study of Elastic-Plastic Behavior of a Fibrous Boron Aluminum Composite," Report to ONR, dept. Civil Engineering, Rensselaer Polytechnic Institute, Troy, N.Y.
- Eisenberg, M.A. and Yen, C.F. (1981), "A Theory of Multiaxial Anisotropic Viscoplasticity," *J. Appl. Mechanics*, Vol. 48, June, pp. 276-284.
- Eisenberg, M.A. and Yen, C.F. (1984), "The Anisotropic Deformation of Yield Surfaces," *J. Engineering Materials and Technology*, Vol. 106, Oct., pp. 355-360.
- Eshelby, J.D. (1957), "The Determination of the Elastic Field of an Ellipsoidal Inclusion and Related Problems," *Proc. R. Soc. London*, Vol. A241, 376.
- Finney, J.L. (1985), "Structure and Properties of Granular Materials: Guidelines from Modelling Studies of Liquids and Amorphous Solids". *Advances in the Mechanics and the Flow of Granular Materials*, Vol. I, Shahinpoor, editor, Trans Tech Publications, Clansthal-Zellerfeld, Fed. Rep. of Germany.

- Hardin, B.O and Richart, F.E. (1963), "Elastic Wave Velocities in Granular Soils". *Journal of the Soil Mechanics and Foundations Division*, ASCE, Vol. 89, SM1, pp. 33-65.
- Hardin, B.O. (1978), "The Nature of Stress-Strain Behavior of Soils," *Proc. ASCE Specialty Conference on Earthquake Engineering and Soil Dynamics*, Pasadena, CA, Vol. 1, 3-90.
- Hardin, B.O. (1980), "Discussion to 'Anisotropic Shear Modulus Due to Stress Anisotropy' by S.K. Roesler," *Journal of the Geotechnical Engineering Division*, ASCE, 106(GT8), August, 956-958.
- Hashin, Z. and Shtrikman, S. (1963), "A Variational Approach to the Theory of the Elastic Behavior of Multiphase Materials," *JMPS*, Vol. 11, 127.
- Helling, D.E., Miller, A.K. and Stout, M.G. (1986), "An Experimental Investigation of the Yield Loci of 1100-0 Aluminum, 70:30 Brass and an Overaged 2024 Aluminum Alloy After Various Prestrains," *J. of Engineering Materials and Technology*, Vol. 108, pp. 313-320.
- Hershey, A.V. (1954), "The Elasticity of an Isotropic Aggregate of Anisotropic Cubic Crystals," *J. Appl. Mechanics*, Vol. 21, 236.
- Hertz, H. (1882), "Uber die Behrungs-fester Elastischer Korper". *J. Reine Angew. Math.*, 92, pp. 156-171.
- Hill, R. (1950), *The Mathematical Theory of Plasticity*, Oxford University Press, London, U.K.
- Hill, R. (1965), "A Self-Consistent Mechanics of Composite Materials," *JMPS*, Vol. 13, 213-222.
- Hill, R. (1967), "The Essential Structure of Constitutive Laws for Metal Composites and Polycrystals," *J. Mech. Phys. Solids*, Vol. 15, pp. 79-95.
- Ishlinsky, A. Iu. (1954), *Ikr. Mat. Zhurnal*, 6, 314.
- Kelley, E.W. and W.F. Hosford (1968), "The Deformation Characteristics of Textured Magnesium," *Transactions of the Metallurgical Society of AIME*, Vol. 242, April, pp. 654-660.
- Klisinski, M., Sture, S., Runesson, K. and Ko, H.K. (1988), "Incremental Constitutive for Cohesionless Granular Materials Based on Fuzzy Sets," *Proceedings, 7th ASCE-EMD Specialty Conference*, Blacksburg, VA, pp. 150.
- Knox, D.P., Stokoe, K.H. and Kopperman, S.E. (1982), "Effects of State of Stress on Velocity of Low Amplitude Shear Waves Propagating Along Principal Stress Directions in Dry Sand," *Geotechnical Engineering Report*, GR82-22, University of Texas, TX.



- Ko, H.Y. and Scott, R.F. (1967), "Deformation of Sand in Hydrostatic Compression," *J. Soil Mech. Found. Div.*, Proc. ASCE, 93, 137-156.
- Koppermann, S.E., Stokoe, K.H. and Knox, D.P. (1982), "Effect of State of Stress on Velocity of Low Amplitude Compression Waves Propagating Along Principal Stress Directions in Sand," Geotechnical Engineering Report, GR82-22, University of Texas, Austin, Texas.
- Kroner, E. (1958), "Berechnung der Elastischen Konstanten des Vielkristalls aus den Konstanten des Einkristalls," *Zeitschrift für Physik*, Bd 151, S504-518.
- Ladd, R.S. (1978), "Preparing Test Specimens Using Undercompaction," *Geotechnical Testing Journal*, Vol. 1, No. 1, March, pp. 16-23.
- Lade, P.V. (1977), "Elastoplastic Stress-Strain Theory for Cohesionless Soil with Curved Yield Surfaces," *Int. J. Solids Structures*, Vol. 13, pp. 1019-1035.
- Lade, P.V. and Duncan, J.M. (1975), "Elastoplastic Stress-Strain Theory for Cohesionless Soil," *Journal of Geotechnical Engineering Division*, ASCE, Vol. 101, No. GT10, pp. 1177-1194.
- Lade, P. V. and Nelson R.B. (1987). "Modelling of the Elastic Behavior of Granular Materials". *International Journal for Numerical and Analytical Methods in Geomechanics*, Vol. 11, pp. 521-542.
- Lin, T.H. and Ito, M. (1965), "Theoretical Plastic Distortion of Polycrystalline Aggregate under Combined and Reversed Stresses," *J. Mech. Phys. Solids*, Vol. 13, pp. 103-115.
- Lin, T.H. and Ito, M. (1966), "Theoretical Plastic Stress-Strain Relationship of a Polycrystal and the Comparison with the Von Mises and the Tresca Plasticity Theories," *Intl. J. Eng. Sci.*, Vol. 4, pp. 543-561.
- Makhlouf, H.M. and Stewart, J.J. (1967), "Elastic Constants of Cubical-Tetrahedral and Tetragonal Sphenoidal Arrays of Uniform Spheres," *Proc. Intl. Symposium on Wave Propagation and Dynamic Properties of Earth Materials*, Albuquerque, NM, Aug.
- Mindlin, R.D. (1949), "Compliance of Elastic Bodies in Contact", *Journal of Applied Mechanics*, Sept., pp. 259-268.
- Mindlin, R.D. and Deresiewicz, H. (1953), "Elastic Spheres in Contact Under Varying Oblique Forces," *J. Appl. Mech., Trans. ASME*, Sept., 327-344.
- Mroz, Z. (1967), "On the Description of Anisotropic Workhardening," *J. Mech. Phys. Solids*, Vol. 15, pp. 163-175.
- Naghdi, P.M., Essenburg, F., and Knoff, W. (1958), "An Experimental Study of Initial and Subsequent Yield Surfaces in Plasticity," *J. Appl. Mech.*, June, pp. 201-209.

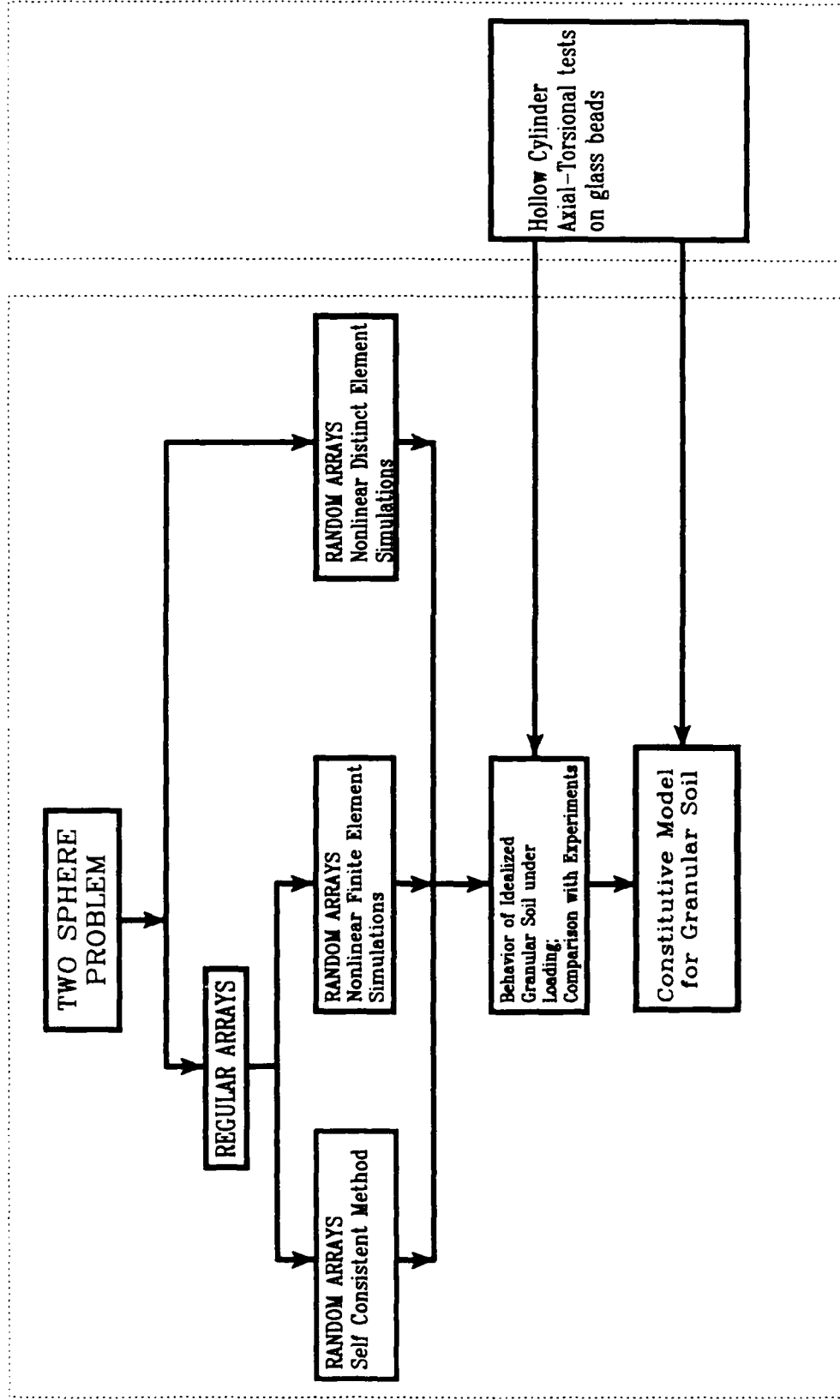
- Ng, T.-T. (1989), "Numerical Simulations of Granular Soil under Monotonic and Cyclic Loading: A Particulate Mechanics Approach". Ph.D. Dissertation, Rensselaer Polytechnic Institute, Troy, NY.
- Ng, T.-T. and Dobry R. (1989), "A Nonlinear Numerical Model for Soil Mechanics," submitted for possible publication to the *Journal for Numerical and Analytical Methods in Geomechanics*.
- Peters, J.F. (1988), "Kinematic Hardening under Jump Rotations," *Proceedings 7th Engineering Mechanics Conference*, Blacksburg, VA, pp. 207.
- Petrakis, E. and Dobry, R. (1986), "A Self Consistent Estimate of the Elastic Constants of a Random Array of Equal Spheres with Application to Granular Soil under Isotropic Conditions," Report CE-86-04, Dept. Civil Engineering, Rensselaer Polytechnic Institute, Troy, NY, July.
- Petrakis, E. and Dobry, R. (1987), "Micromechanical Modeling of Granular Soil at Small Strain by Arrays of Elastic Spheres," Report CE-87-02, Dept. Civil Engineering, Rensselaer Polytechnic Institute, Troy, NY, September
- Petrakis, E. and Dobry, R. (1987a), "A Two-Dimensional Numerical Micromechanical Model for Granular Soil at Small Strains," Research Report, Department of Civil Engineering, Rensselaer Polytechnic Institute, Troy, NY, June.
- Petrakis, E. Dobry, R. and Ng, T.-T. (1988), "Small Strain Response of Random Arrays of Elastic Spheres Using a Distinct Element Procedure," Research Report, Dept. of Civil Engineering, Rensselaer Polytechnic Institute, Troy, NY, July.
- Petrakis, E. and Dobry R. (1989), "Small Strain Elastic Constants of Precycled Sands by the Self-Consistent Method," submitted for possible publication to the *Journal of Engineering Mechanics*, ASCE.
- Phillips, A. (1968), "Yield Surfaces of Pure Aluminum at Elevated Temperatures," *IUTAM-Symposium on Thermoelasticity*, pp. 241-258.
- Phillips, A., Liu, C.S., and Justusson, J.W. (1970), "An Experimental Investigation of Yield Surfaces at Elevated Temperatures," *Acta Mechanica*, Vol. 14, pp. 119-146.
- Phillips, A. and Tang, J.L. (1972), "The Effect of Loading Path on the Yield Surface at Elevated Temperatures," *Int. J. Solids and Structures*, Vol. 8, pp. 463-474.
- Phillips, A., Tang, J.L. and Ricciutti, M. (1974), "Some New Observations on Yield Surfaces," *Acta Mechanica*, 20, pp. 23-29.
- Phillips, A. and Weng, G.J. (1975), "An Analytical Study of an Experimentally Verified Hardening Law," *J. Appl. Mech.*, June, pp. 375-378.

- Poritsky, H. (1950), "Stresses and Deflections of Cylindrical Bodies in Contact with Application to Contact of Gears and Locomotive Wheels," *Journal of Applied Mechanics*, June, pp. 191-201.
- Prager, N. (1955), "The Theory of Plasticity: A Survey of Recent Achievement," *Proceedings Inst. Mech. Eng.*, Vol. 169, pp. 41-57, London, U.K.
- Prevost, J.H. (1978), "Plasticity Theory for Soil Stress-Strain Behavior," *Journal of the Engineering Mechanics Division*, ASCE, Vol. 104, No. EM5, pp. 1177-1194.
- Prevost, J.H. (1985), "A Simple Plasticity Theory for Frictional Cohesionless Soils," *Soil Dynamics and Earthquake Engineering*, Vol. 4, No. 1, pp. 9-17.
- Reyes, S.F. (1966), "Elastic-Plastic Analysis of Underground Openings by the Finite Element Method," Ph.D. Thesis, University of Illinois, Urbana, Ill.
- Roscoe, K.H., Schofield, A.N. and Wroth, C.P. (1958), "On the Yielding of Soils," *Geotechnique*, Vol. 9, pp. 22-53.
- Rousset, M. (1985), "Surface Seuil de Plasticite: Determination Automatique et Modelisation", These de Docteur Ingenieur, Laboratoire de Mecanique et Technologie, Universite Pierre et Marie Curie, Paris-6, Cachan, France.
- Saada, A.S. (1987), "International Workshop on Constitutive Equations for Granular Non-Cohesive Soils," Case Western Reserve University, Cleveland, OH., July.
- Scott, G.D. (1960), "Packing of Equal Spheres," *Nature*, Vol. 188, pp. 908-909.
- Seed, H.B. and Idriss, I.M. (1970), "Soil Moduli and Damping Factors for Dynamic Response Analyses," Earthquake Engineering Research Center Report No. EERC 70-10, University of California, Berkeley.
- Seridi, A. and Dobry, R. (1984), "An Incremental Elastic-Plastic Model for the Force-Displacement Relation at the Contact Between Two Spheres," Research Report, Dept. of Civil Engineering, Rensselaer Polytechnic Institute, Troy, N.Y.
- Shahinpoor, M. (1981), "Statistical Mechanical Considerations on Storing Bulk Solids," *Bulk Solids Handling*, Vol. 1, Feb., 31-36.
- Shahinpoor, M. and Shahrpas, A. (1982), "Frequency Distribution of Voids in Layers of Randomly Packed Equal Spheres," *Bulk Solids Handling*, Vol. 2, 4, pp. 825-838.
- Shiratori, E., Ikegami, K., Yoshida, Kaneko, K. and Koike, S. (1976), "The Subsequent Yield Surfaces after Preloading under Combined Axial Load and Torsion," *Bulletin of the ISME*, Vol. 19, No. 134, August, pp. 877-883.

- Smith, W.O., Foote, P.D. and Busang, P.F. (1929), "Packing of Homogeneous Spheres," *Phys. Rev.*, **34**, 1271-1274.
- Song, K. and Stokoe, K.H. II (1987). The Effect of Prestraining on the Small Strain Shear Modulus of Dry Sand," Geotechnical Engineering Report, University of Texas, Austin, TX.
- Strack, O.D.L. and Cundall, P.A. (1984), "Fundamental Studies of Fabric in Granular Materials". Interim Report to NSF CEE 8310729, Department of Civil and Mineral Engineering, University of Minnesota, Minneapolis, MN.
- Stout, M.G., Martin, P.L., Helling, D.E. and Canova, G.R. (1985), "Multiaxial Yield Behavior of 1100 Aluminum Following Various Magnitudes of Prestrain," *Int. J. of Plasticity*, Vol. 1, pp.163-174.
- Sture, S., Alawi, M.M. and Ko, H.-Y. (1987), "True Triaxial and Directional Shear Cell Experiments on Dry Sand," Report to US Army Eng. Waterways Experiment Station, Dep. of Civil, Environmental, and Architectural Engng., University of Colorado, Boulder, Colorado.
- Szalwinski, C.M. (1985), "Flexibility of a Contact Area of An Isotropic Elastic Body". *Journal of Applied Mechanics*, Vol. 52, March, pp. 62-66.
- Walton, K. (1978), "The Oblique Compression of Two Elastic Spheres," *Journal of the Mechanics and Physics of Solids*, Vol. 35, pp. 213-226.
- Walton, K. (1987), "The Effective Elastic Moduli of a Random Packing of Spheres," *Journal of the Mechanics and Physics of Solids*, Vol. 26, 139-150.
- White, J.E. (1965), *Seismic Waves*, McGraw-Hill, New York.
- Wright, R.V., Gilbert, P.A. and Saada, A.S. (1978), "Shear Devices for Determining Dynamic Soil Properties," *Proc. of the Earthquake Engineering and Soil Dynamics Conference, Geotechnical Engineering Division*, ASCE, Pasadena, June, pp. 19-21.
- Yanagisawa, E. (1983), "The Influence of Void Ratio and Stress Condition on the Dynamic Shear Modulus of Granular Media," *Advances in the Mechanics and the Flow of Granular Materials*, Vol. II, M. Shahinpoor, Ed., Trans. Tech. Publications, Clausthal-Zellerfeld, Fed. Republic of Germany.
- Yen, C.F. (1979), "On the Theory of Cyclic Viscoplasticity," Ph.D. Dissertation, University of Florida, Gainesville, FL.
- Yen, C.F. and Eisenberg, M.A. (1987), "The Role of a Loading Surface in Viscoplasticity Theory," *Acta Mechanica*, **69**, pp. 77-96.
- Ziegler, H. (1958), "A Modification of Prager's Hardening Rule," *J. Appl. Math. Phys.*, Vol. 9a, No. 3, pp. 260-276.

**TABLE 1. AFOSR MICROMECHANICAL RESEARCH AT RPI**

**1. ANALYTICAL EFFORT**



**2. EXPERIMENTAL EFFORT**

## TABLE 2. RPI COMPUTER PROGRAM CONBAL-2

(after Ng and Dobry 1989)

CONBAL-2 = CONTACT truBAL in 2-D

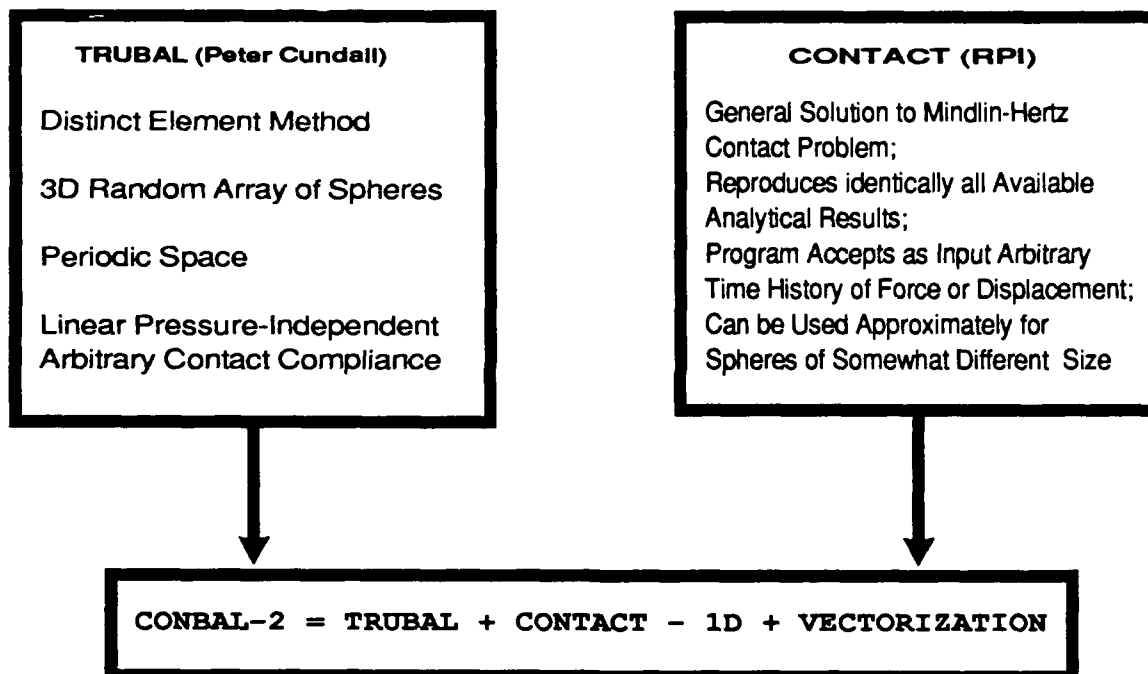


TABLE 3. Properties of Glass Beads

---

Specific Gravity	2.45 to 2.50
Roundness	Minimum of 70%
Poisson's Ratio	0.21
Young's Modulus	$68.97 \times 10^6$ KPa
Rigidity (Shear) Modulus	$29.66 \times 10^6$ KPa
Static Coefficient of Friction	0.9 to 1.0
Dynamic Coefficient of Friction	0.7 to 0.8

---

TABLE 4. Summary of Monotonic Radial Shear Tests on Glass Beads Specimens

Type of Test ( $\omega^\circ$ )	Isotropic Confining Pressure $\sigma_c$ (KPa)	Void Ratio e	Relative Density $D_r$ %	Pore Pres. Param. B	Angle of Shear Direct. $\theta^\circ$	Coefficient b
Compr. ( $0^\circ$ )	136.8	0.593	53	0.954	0	0.0
Tors. ( $45^\circ$ )	141.2	0.603	47	0.963	30	0.5
Ext. ( $90^\circ$ )	140.0	0.602	48	0.985	60	1.0
Compr. ( $0^\circ$ )	277.0	0.605	46	0.965	0	0.0
Compr. ( $0^\circ$ )	414.1	0.603	47	0.955	0	0.0



TABLE 5. Summary of Reversible Tests on Glass Bead Specimens

Direction of Pre- Straining	Isotropic Confining Pressure $\sigma_c$ (KPa)	Void Ratio e	Relative Density $D_r$ %	Pore Press. Param. B	Pre- Cycling (*)	Yield Surface Assoc. with $ \Delta\gamma_{oct} $
Compres.	137.0	0.595	52	0.987	Yes	0.05%
Torsion	138.1	0.598	50	0.950	Yes	0.05%
Compres.	139.2	0.597	51	0.954	No	0.1%
Torsion	139.5	0.604	47	0.978	No	0.2%

(\*) Applied cyclic shear strain  $\gamma_{z\theta} = 0.07\%$ . Number of cycles  $N = 600$

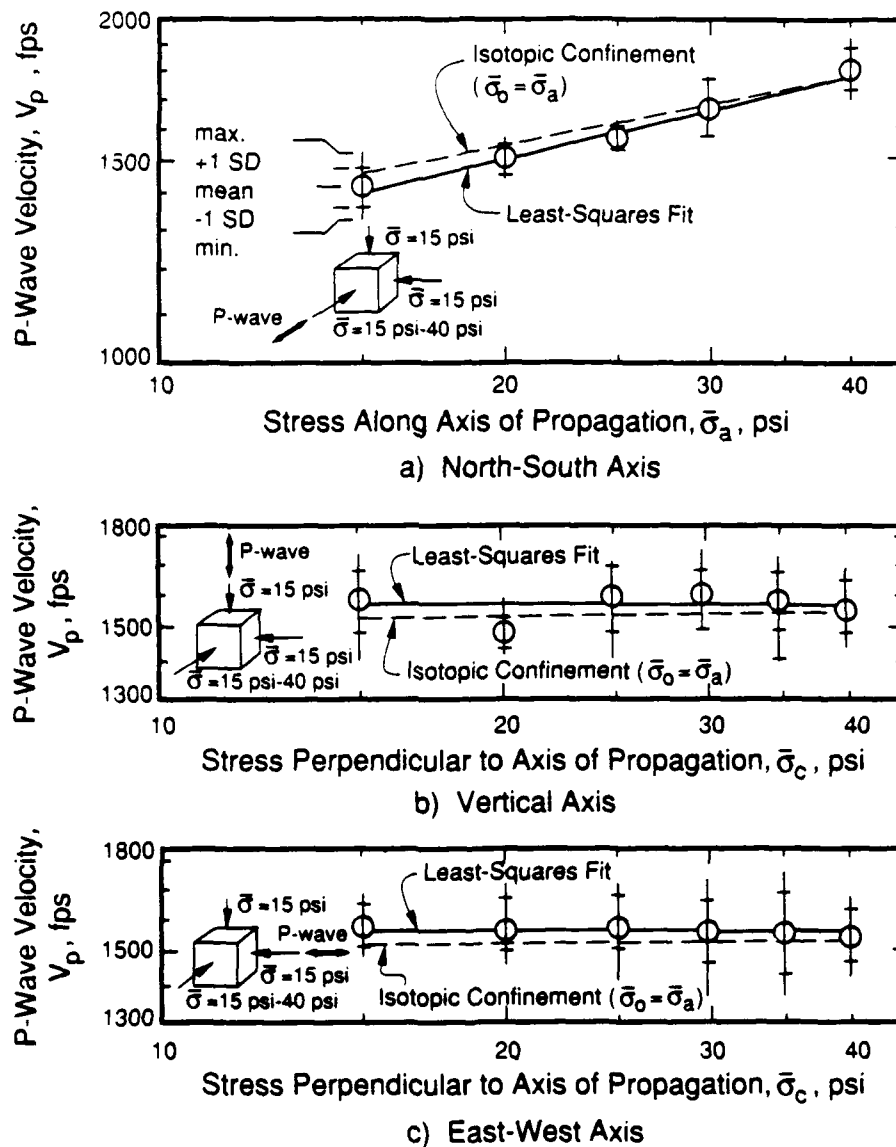


Figure 1. Effect of stress induced anisotropy on compressional wave velocity for triaxial confinement (Kopperman et al. 1982).

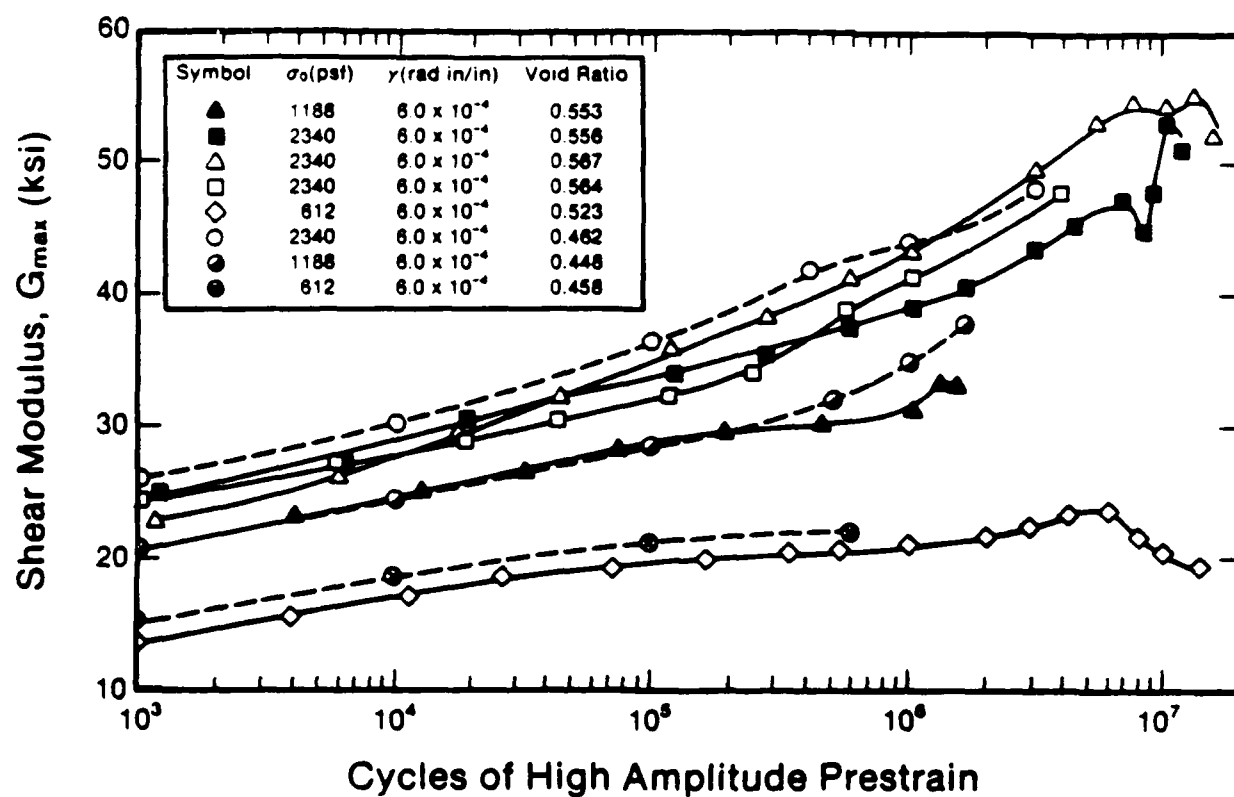


Figure 2. Small Strain Shear Modulus,  $G_{\max}$ , versus Cycles of Shear Prestrain – Hollow Cylindrical Samples (Drnevich 1967).

## Cubical Triaxial Cell Experiments

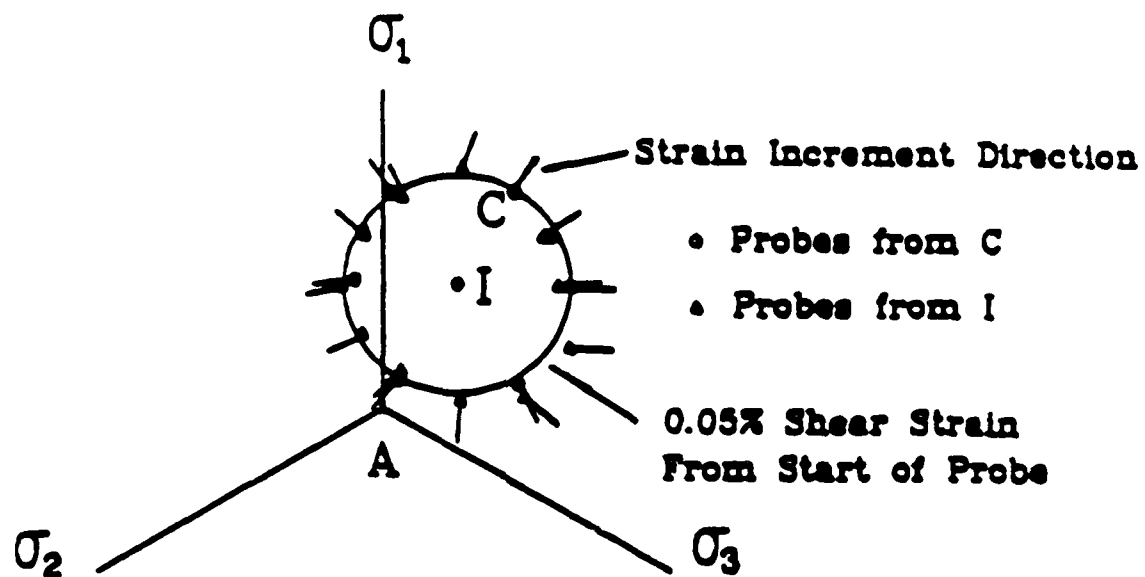


Figure 3. Experimentally obtained yield surface of sand from cubical triaxial experiments (Peters 1988).

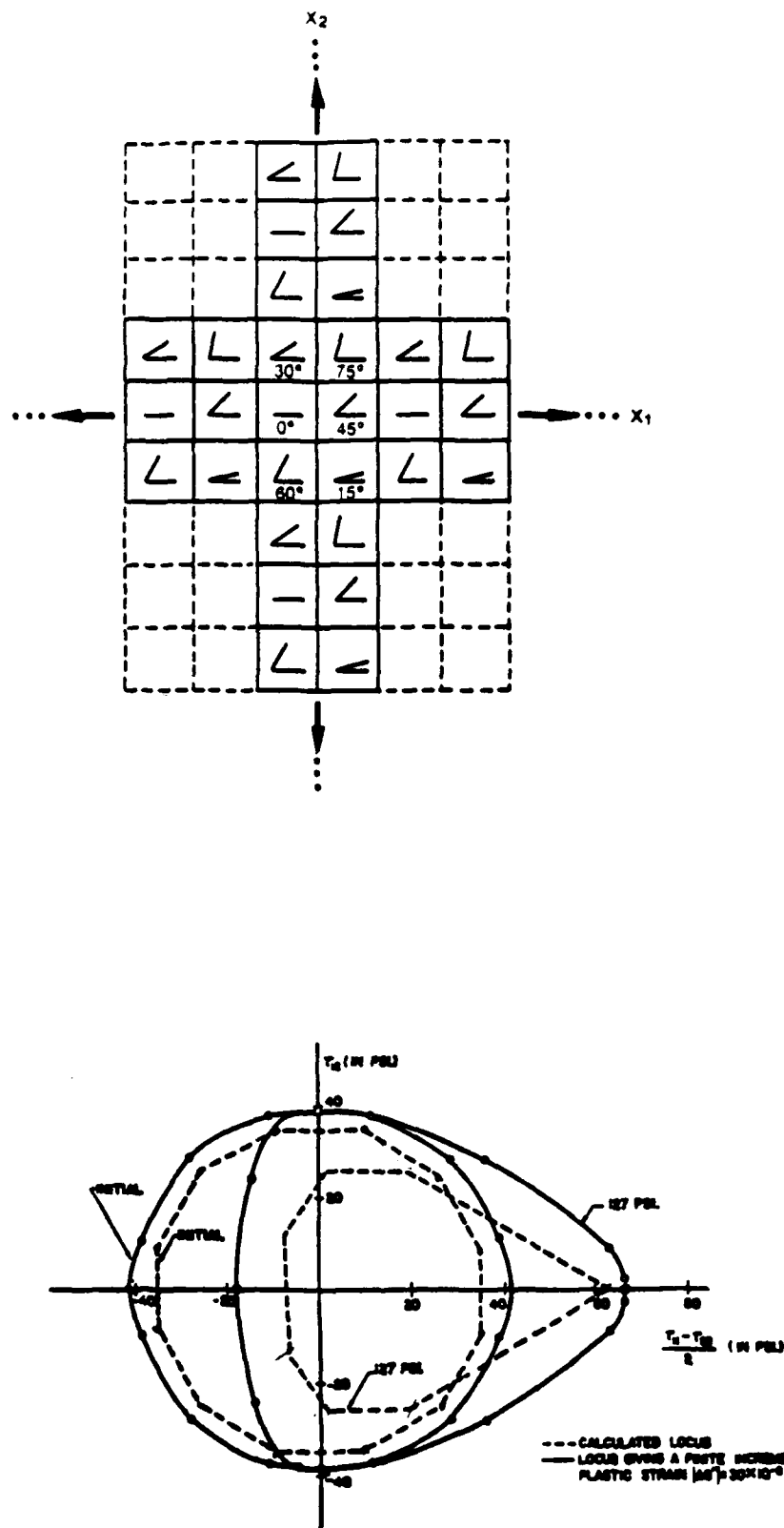


Figure 4.

The repeating six crystal aggregate in the infinite plane (angle of sliding shown in each crystal) (a), yield loci of the aggregate at different stages of tensile loading with an observed vertex (b), (Lin and Ito 1965).

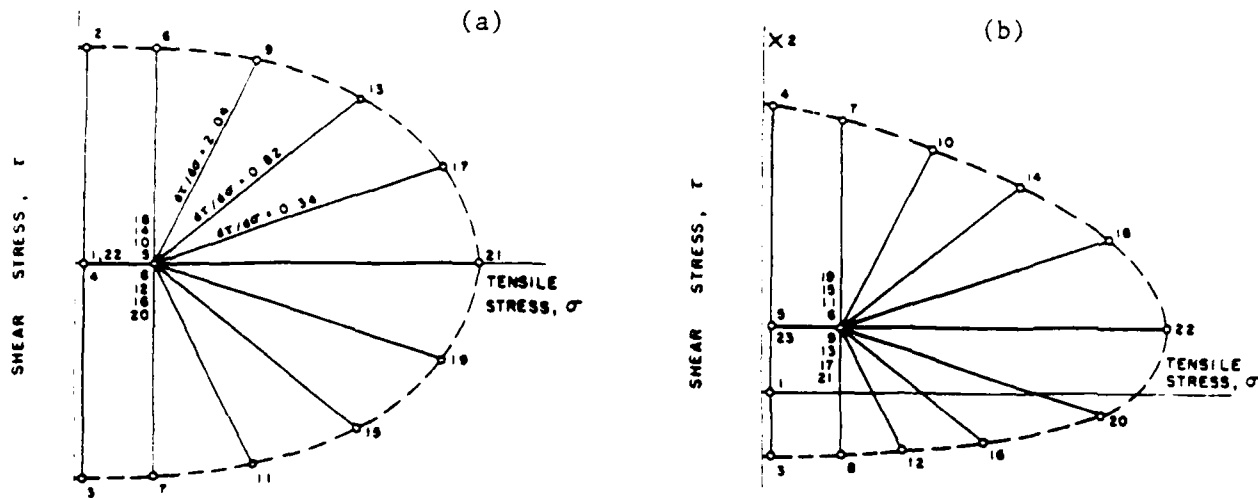


Figure 5. Loading paths for (a) initial, and (b) subsequent yield surfaces (Phillips 1968).

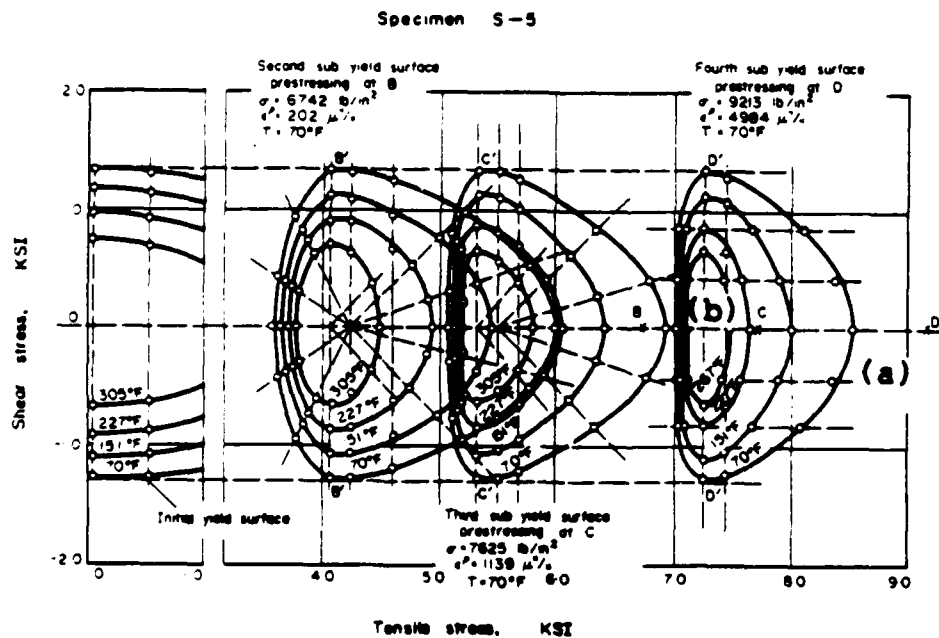
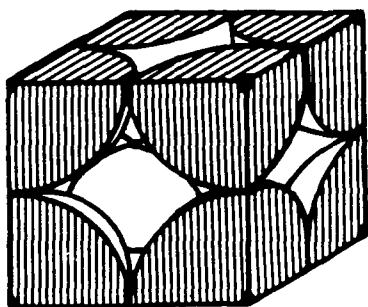
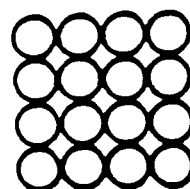


Figure 6. Experimentally obtained initial and subsequent yield surfaces for aluminum at 70°F temperature (Phillips and Tang 1972).



Simple Cubic Unit Cell



Simple cubic structure

Figure 7. Simple cubic array of spheres.

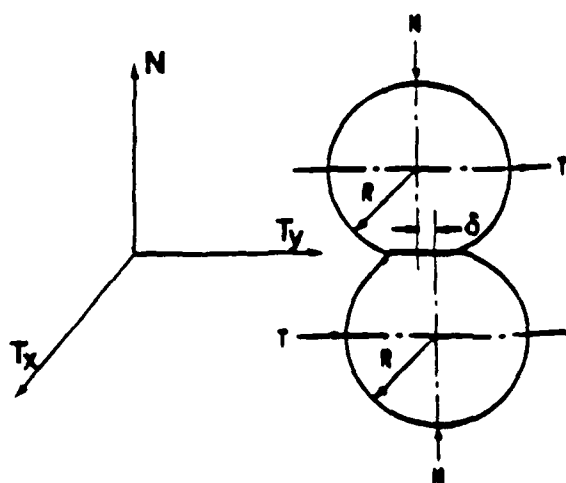


Figure 8a. Elastic Spheres Under Normal and Tangential Loads.

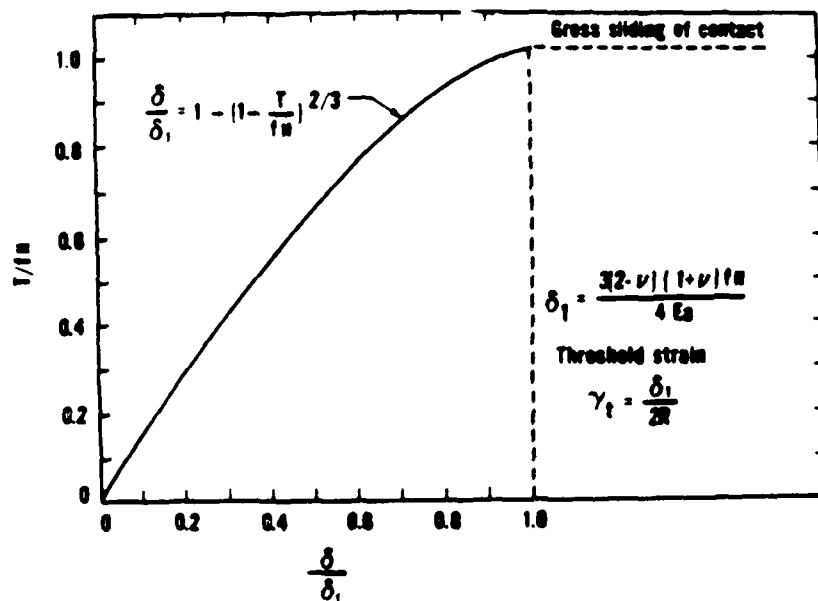


Figure 8b. Tangential Force-Displacement Relation for  $N$  Constant,  $T$  increasing (Dobry et al. 1982).



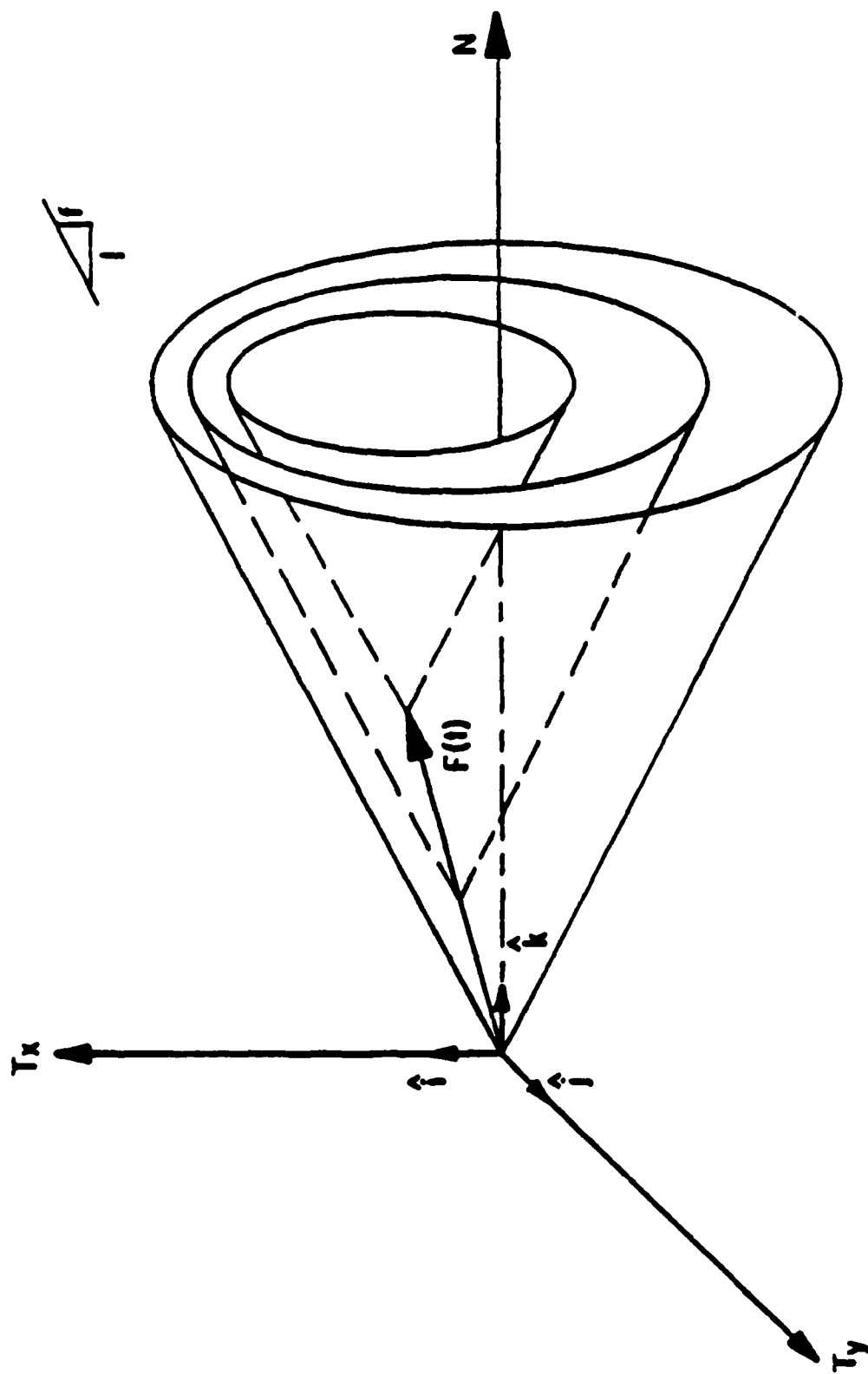


Figure 9. Contact Force Space and Conical Yield Surfaces, Elastic-Plastic Incremental Solution of Mindlin's Problem (Seridi and Dobry 1984).

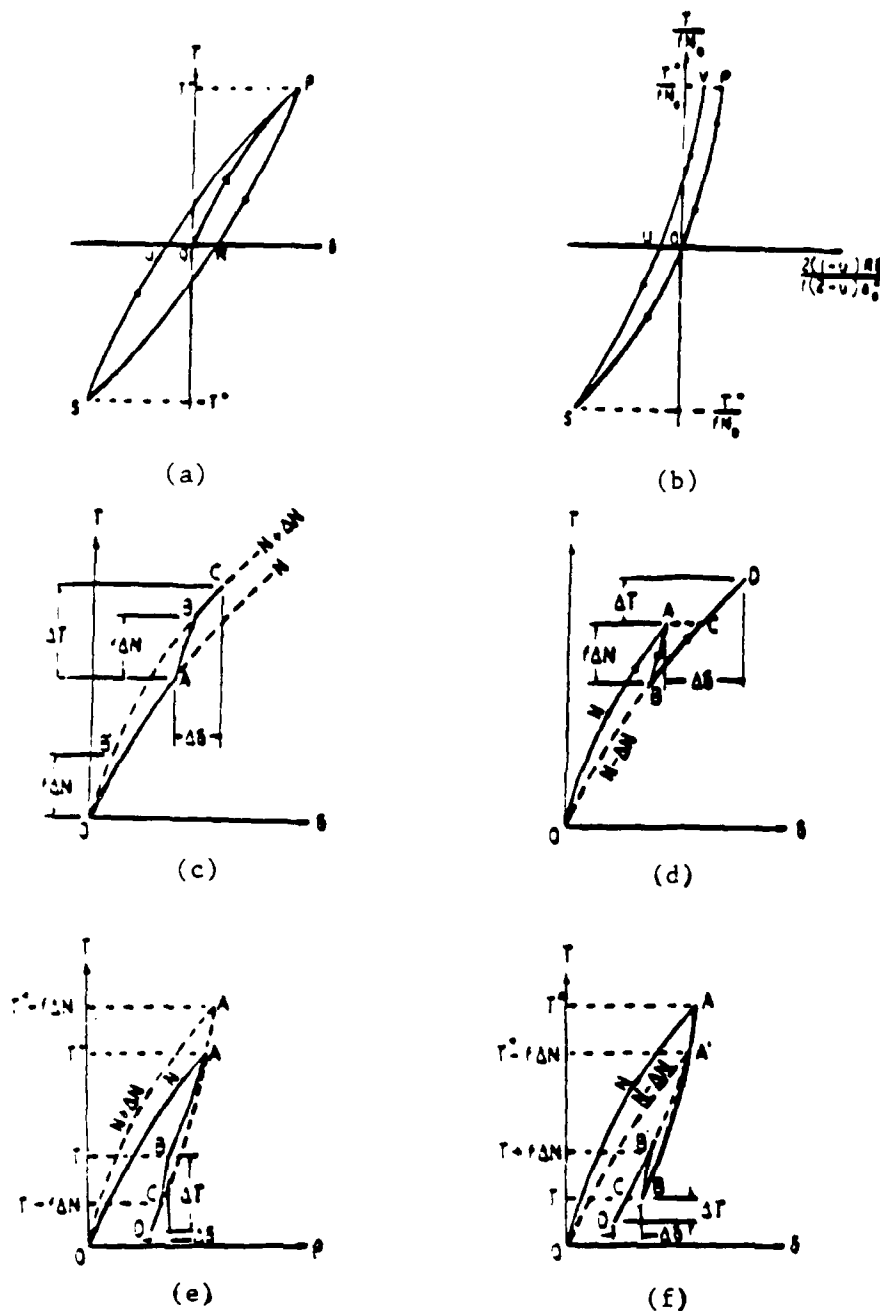


Figure 10. Force-deformation Behavior of Two Elastic Rough Spheres in Contact: Analytical Solution for Oscillating Oblique Forces with (a)  $dT/dN > f$  and (b)  $dT/dN < f$ ; (c)  $N$  Increasing,  $T$  Increasing; (d)  $N$  Decreasing,  $T$  Increasing; (e)  $N$  Increasing,  $T$  Decreasing; (f)  $N$  Decreasing,  $T$  Decreasing; (Mindlin and Deresiewicz 1953).

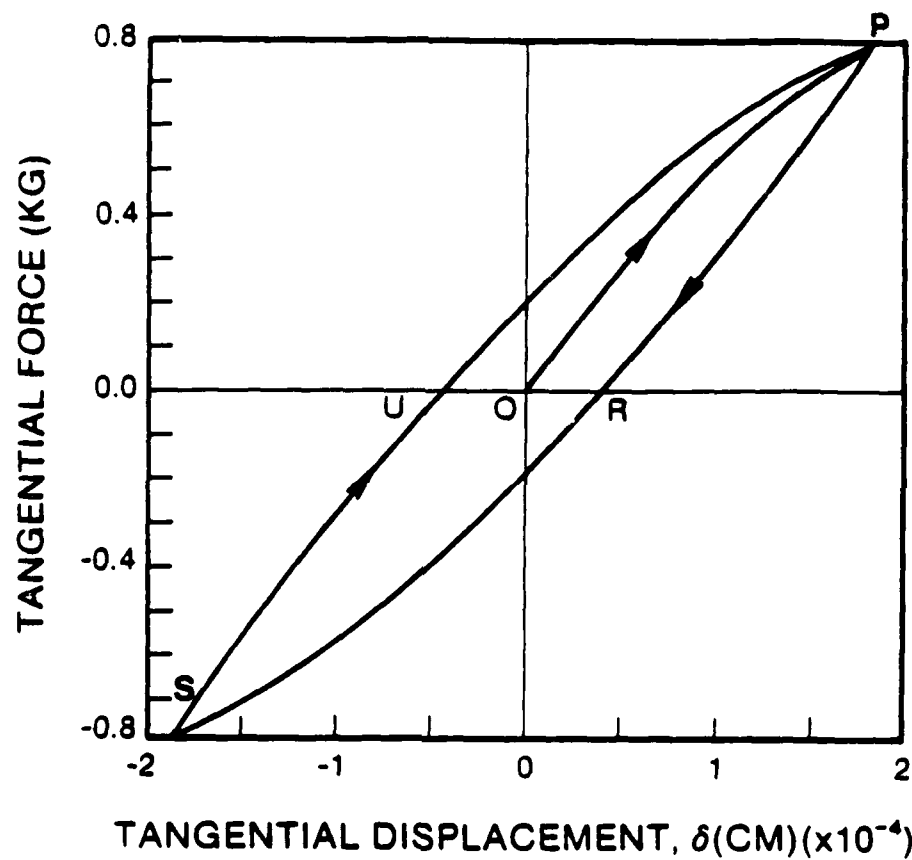


Figure 11.

Numerical Simulation of the Force-Deformation Behavior for Two Equal, Elastic, Rough Spheres in Contact: Load-Displacement Relation for an Oscillating Oblique Force with  $dT/dN > f$ .

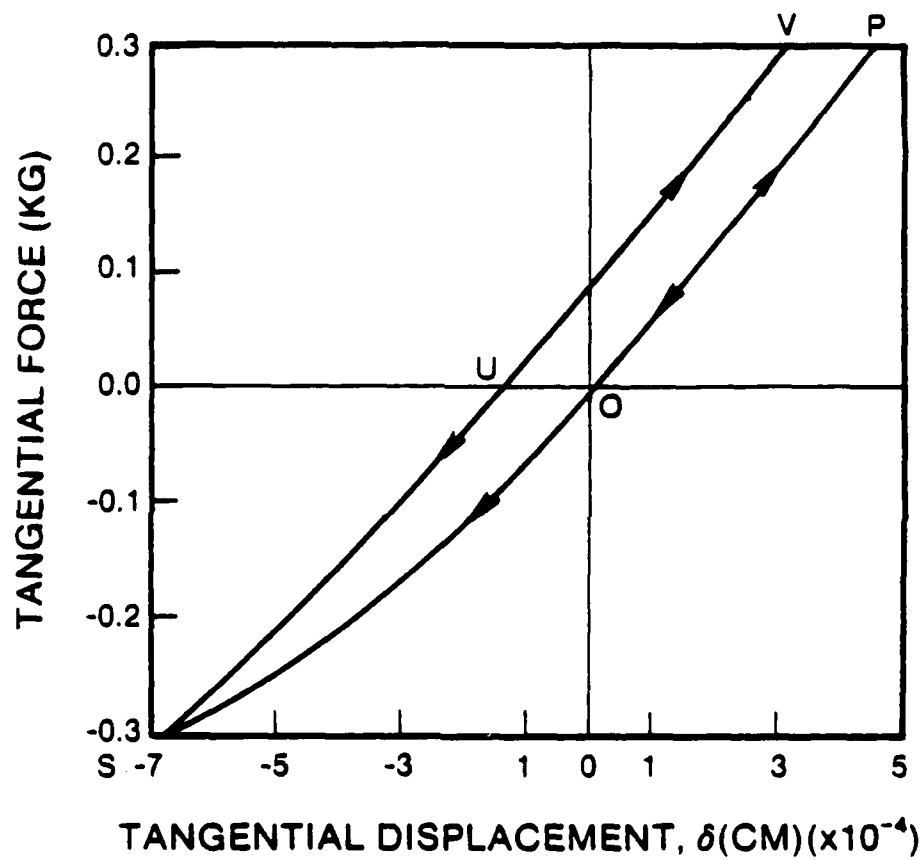


Figure 12.

Numerical Simulation of the Force-Deformation Behavior for Two Equal, Elastic, Rough Spheres in Contact: Load-Displacement Relation for an Oscillating Oblique Force with  $dT/dN < f$ .

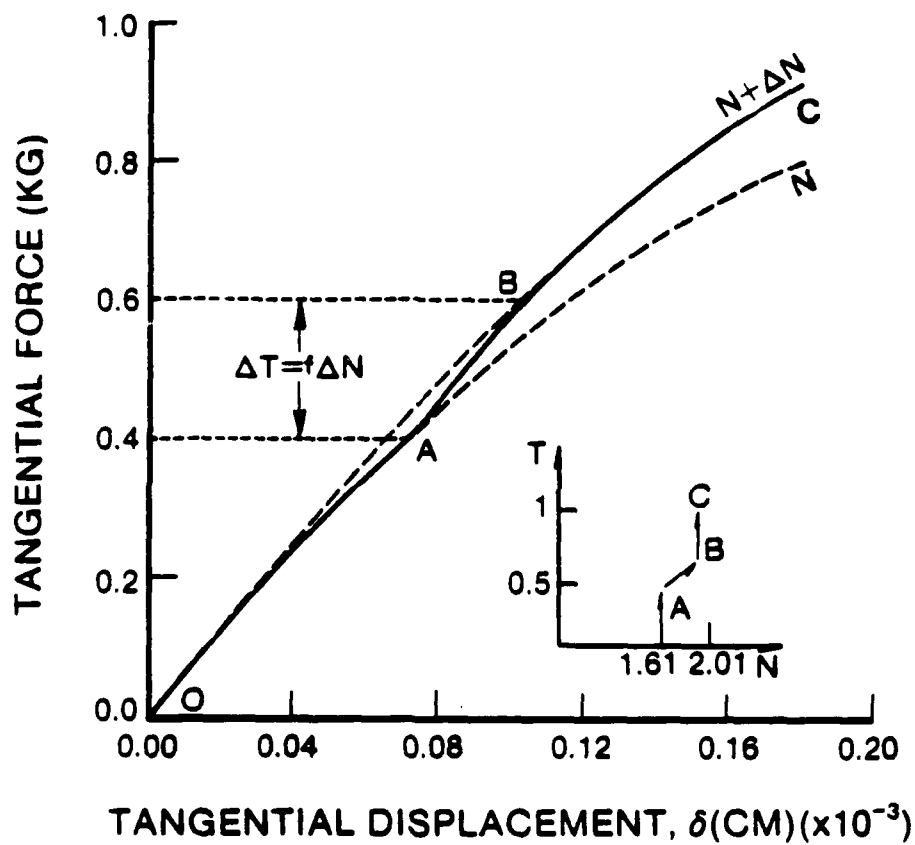


Figure 13. Numerical Simulation of the Force-Deformation Behavior for Two Equal, Elastic, Rough Spheres in Contact: Load-Displacement Relation for the Case in which  $N$  Increases and  $T$  Increases.

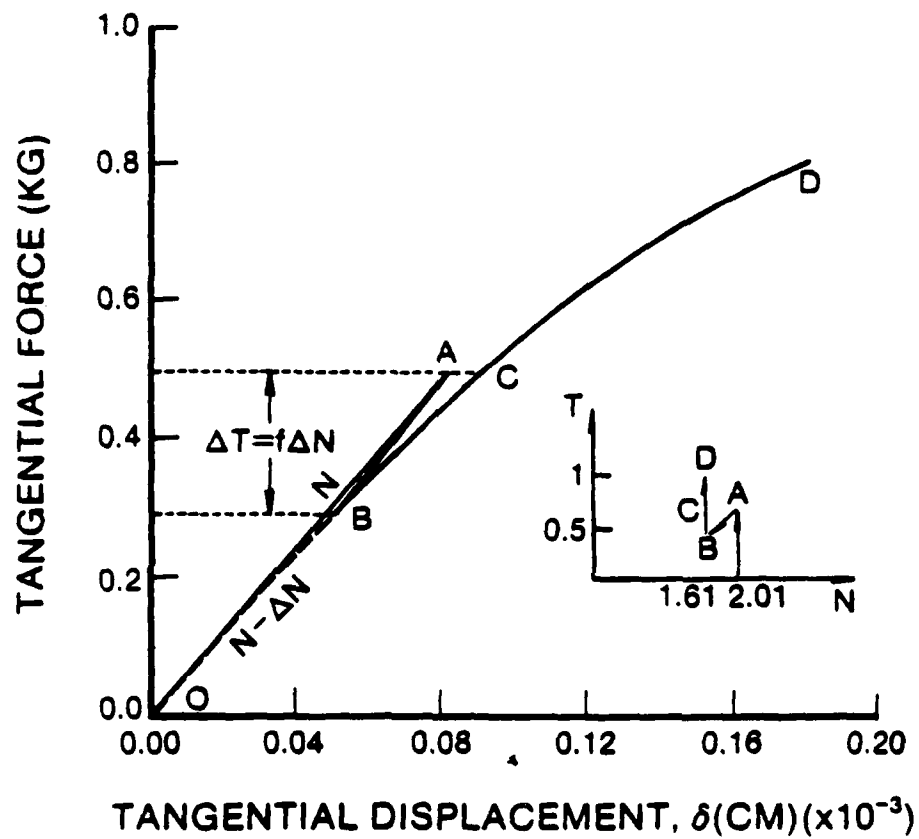


Figure 14.

Numerical Simulation of the Force-Deformation Behavior for Two Equal, Elastic, Rough Spheres in Contact: Load-Displacement Relation for the Case in which  $N$  Decreases and  $T$  Increases.

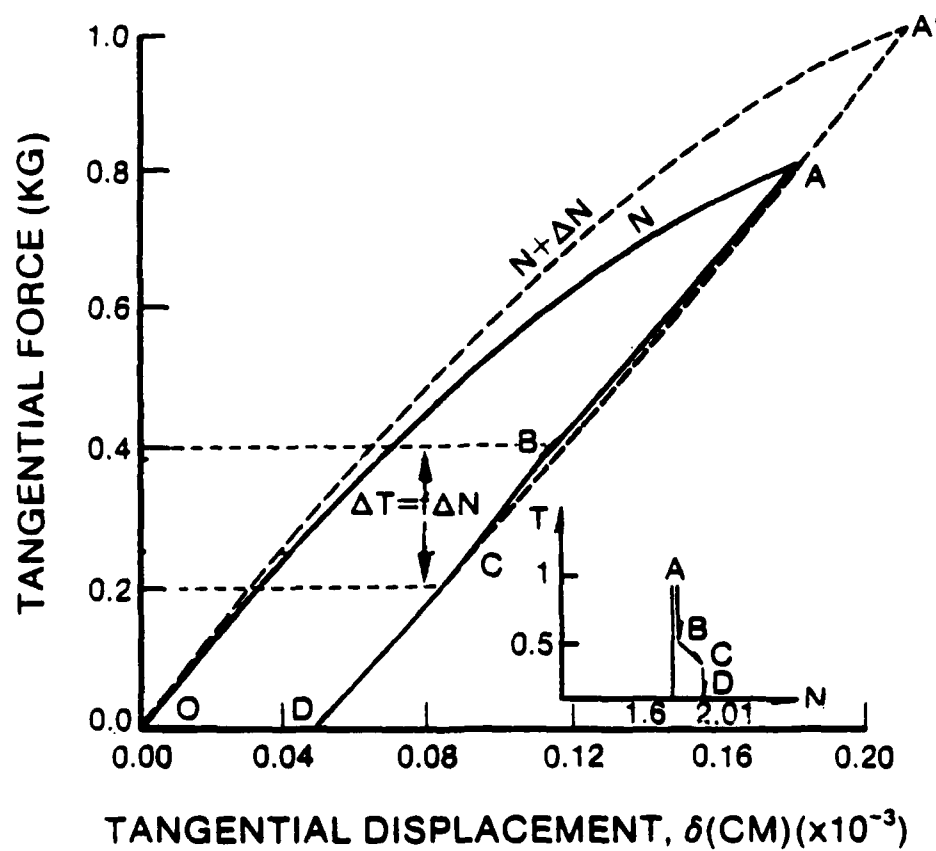


Figure 15.

Numerical Simulation of the Force-Deformation Behavior for Two Equal, Elastic, Rough Spheres in Contact: Load-Displacement Relation for the Case in which  $N$  Increases and  $T$  Decreases.

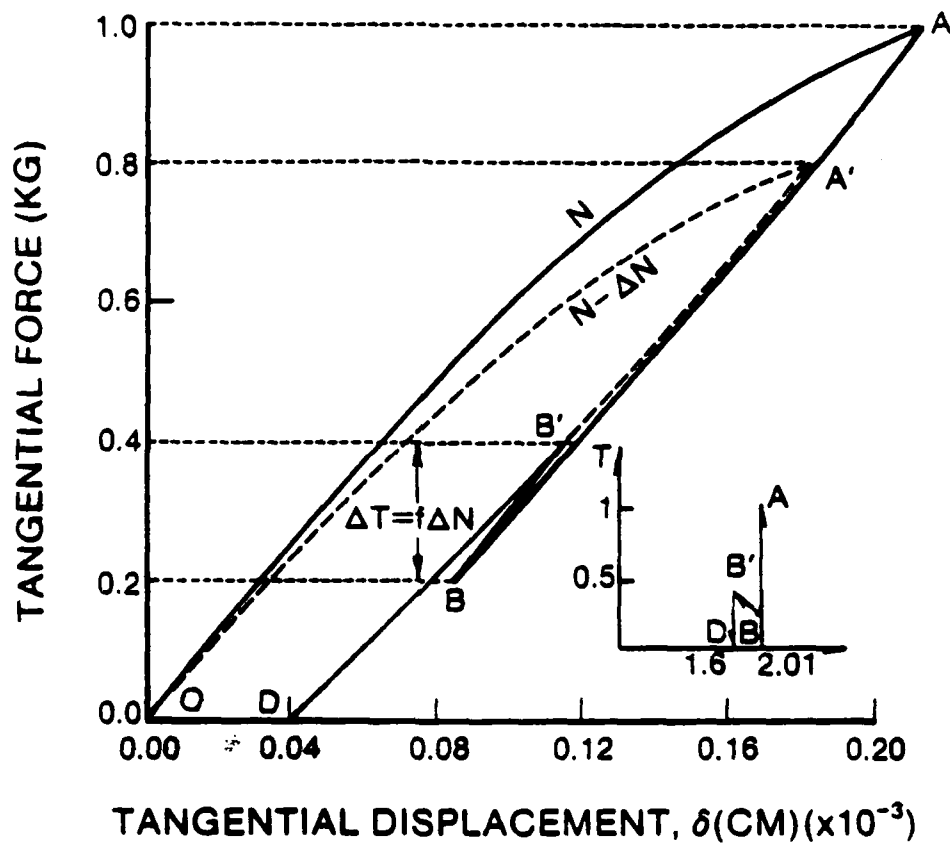
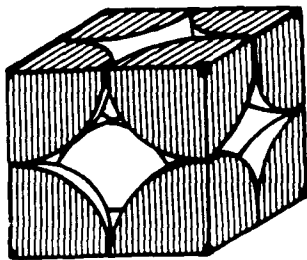


Figure 16.

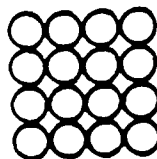
Numerical Simulation of the Force-Deformation Behavior for Two Equal, Elastic, Rough Spheres in Contact: Load-Displacement Relation for the Case in which  $N$  Decreases and  $T$  Decreases.



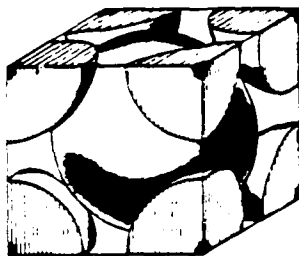


Simple Cubic Unit Cell

(a)



Simple cubic structure

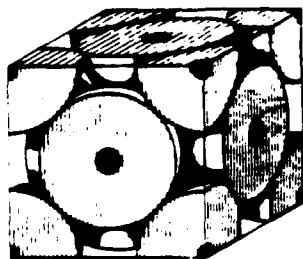


Body-centered cubic unit cell

(b)



Body-centered cubic structure



Face-centered cubic unit cell

(c)



Face-centered cubic structure

Figure 17. Three Regular Arrays of Equal Spheres.

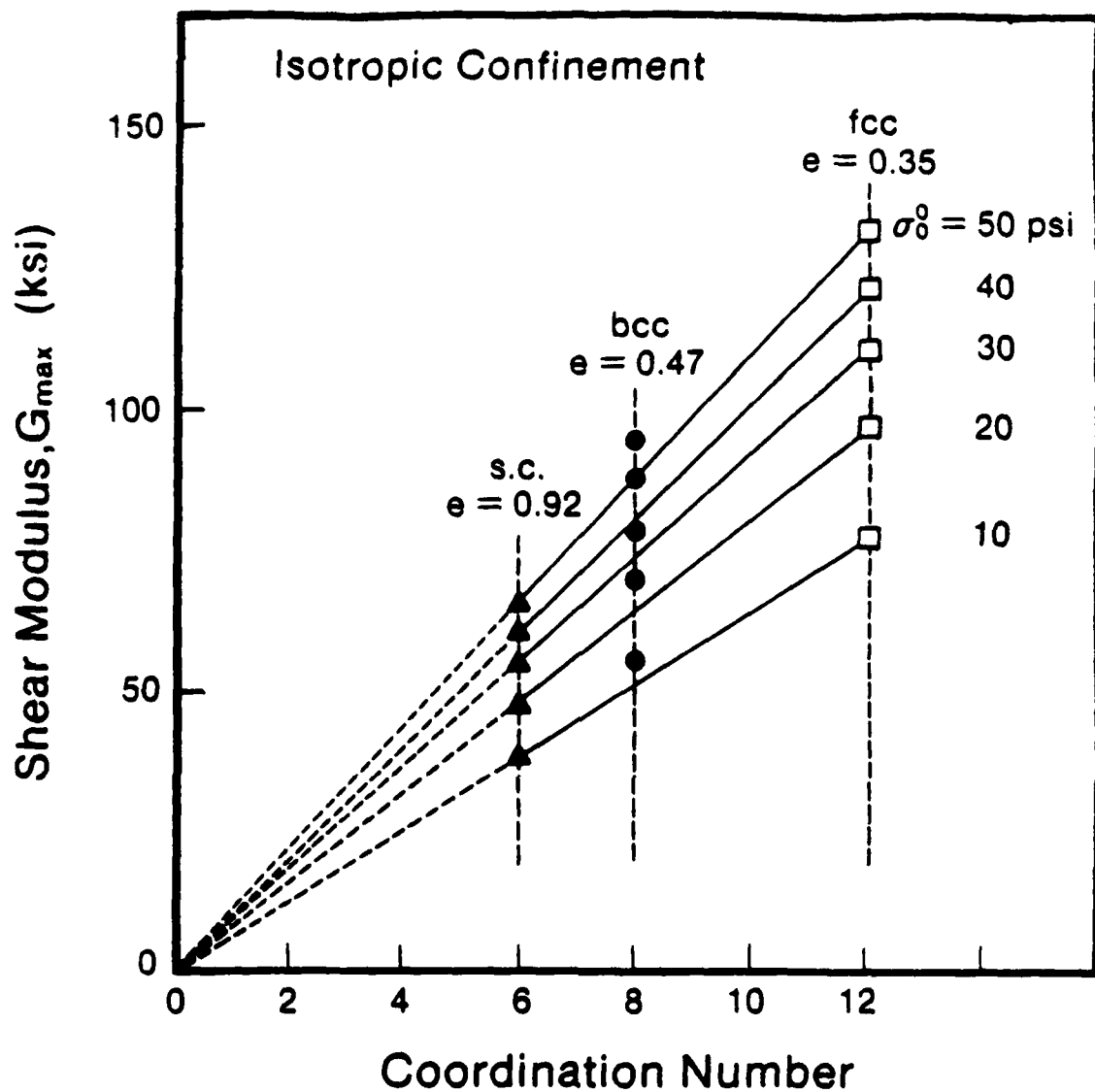


Figure 18. Small Strain Modulus,  $G_{\max}$ , versus Coordination Number (= number of contacts per sphere) for Regular Cubic Arrays of Quartz Spheres.

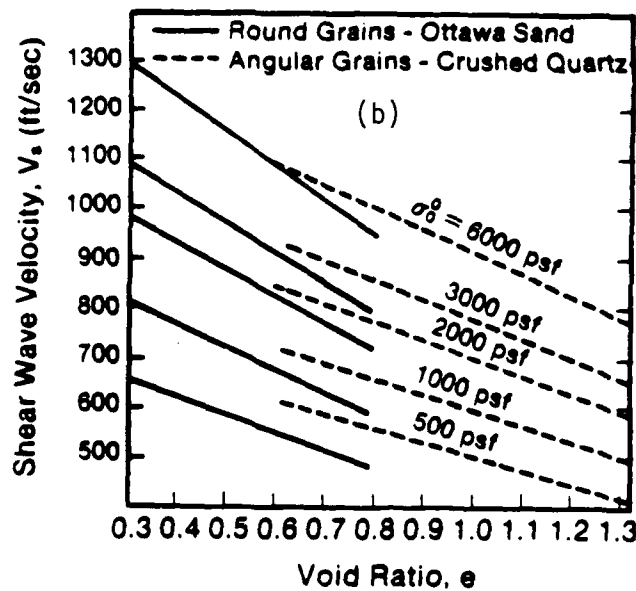
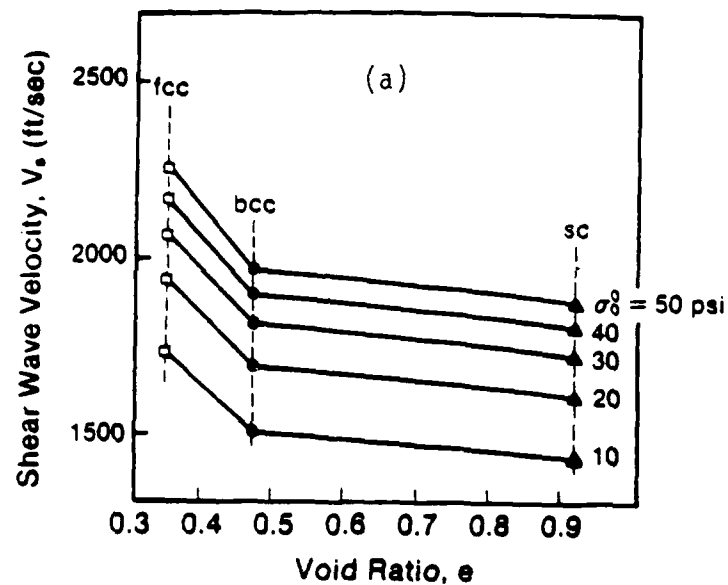


Figure 19.

Shear Wave Velocity versus Void Ratio: Comparison between Predictions from Regular Cubic Arrays of Quartz Spheres and Measurements in Quartz Sand.

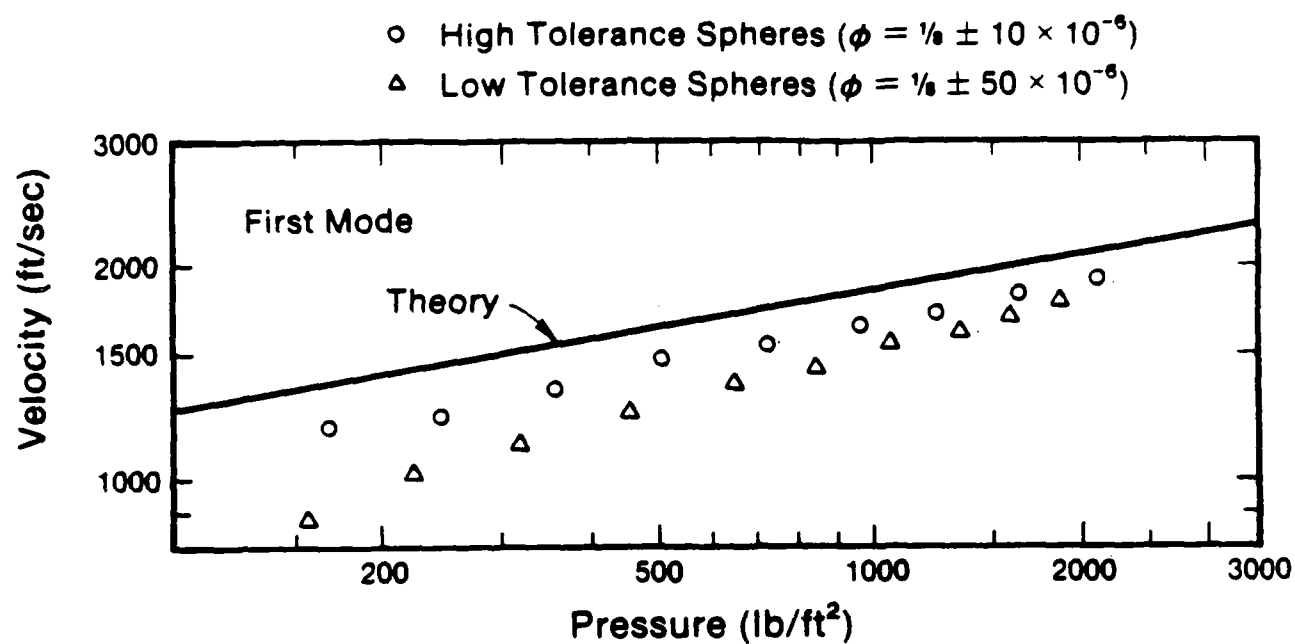


Figure 20. Rod Wave Velocity Measurements in Regular Dense Array of Steel Spheres Loaded Isotropically (Duffy and Mindlin 1957).

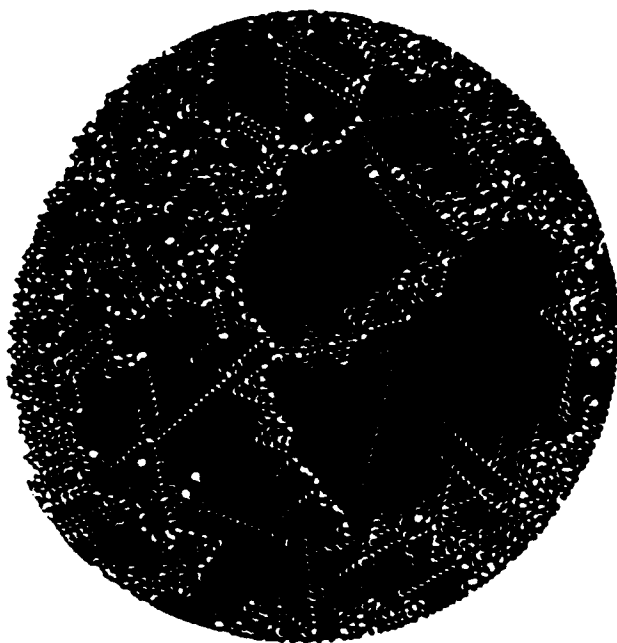
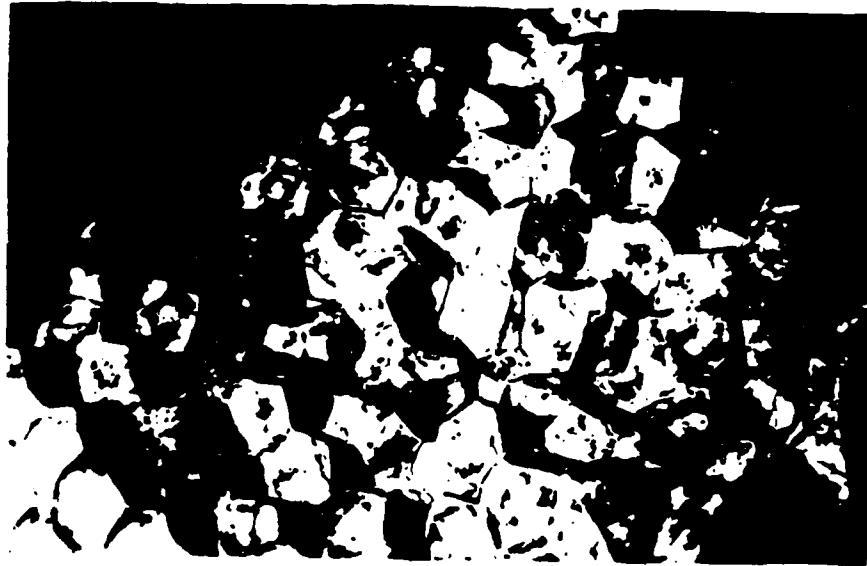


Figure 21. (a) Cut-Away Artistic View of a Space Filling Configuration of Voronoi Polyhedra Containing Regular Arrays of Spheres (Finney 1983) and (b) Random Two-Dimensional Packing of Equal Sized Spherical Steel Balls (Shahinpoor and Shahrpass 1982).

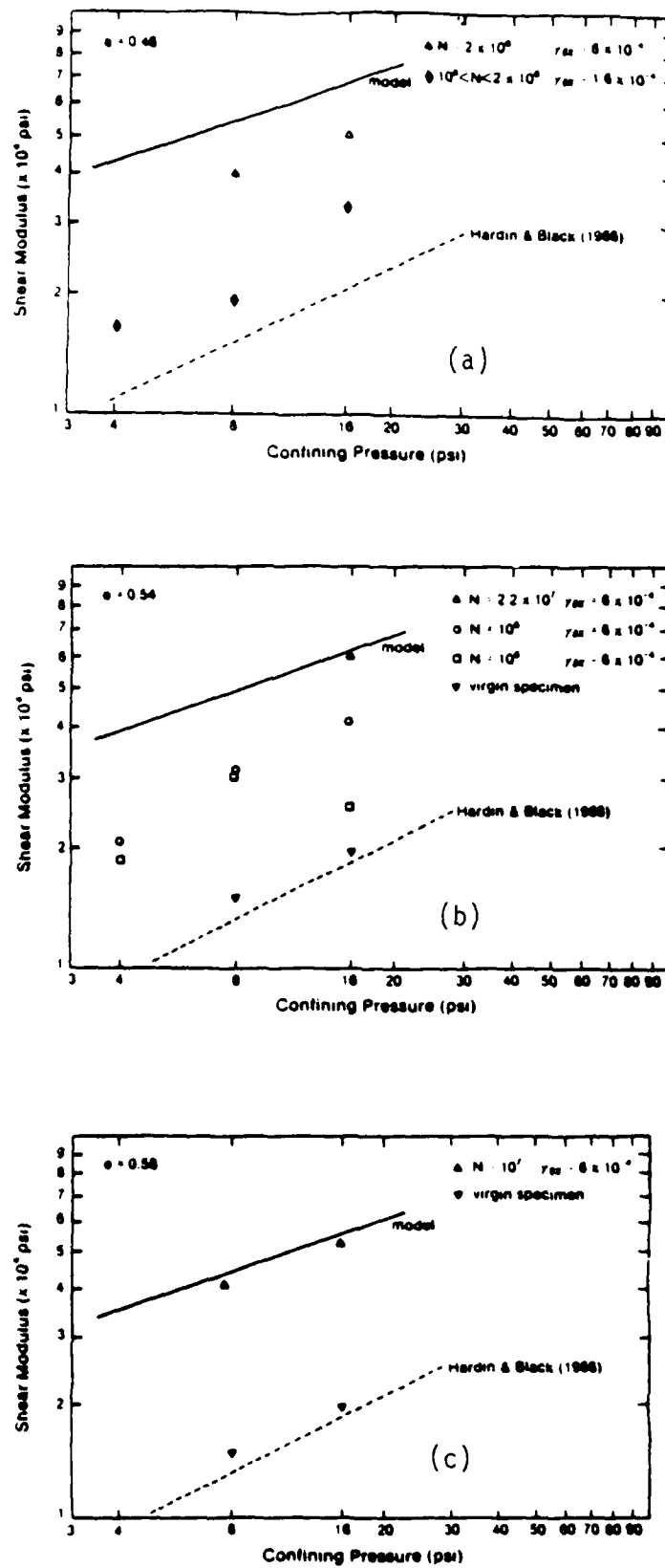


Figure 22. Small Strain Shear Modulus,  $G_{\text{max}}$ , versus Isotropic Confining Pressure: Analytical and Experimental Results for (a)  $e = 0.46$ , (b)  $e = 0.54$  and (c)  $e = 0.58$ .

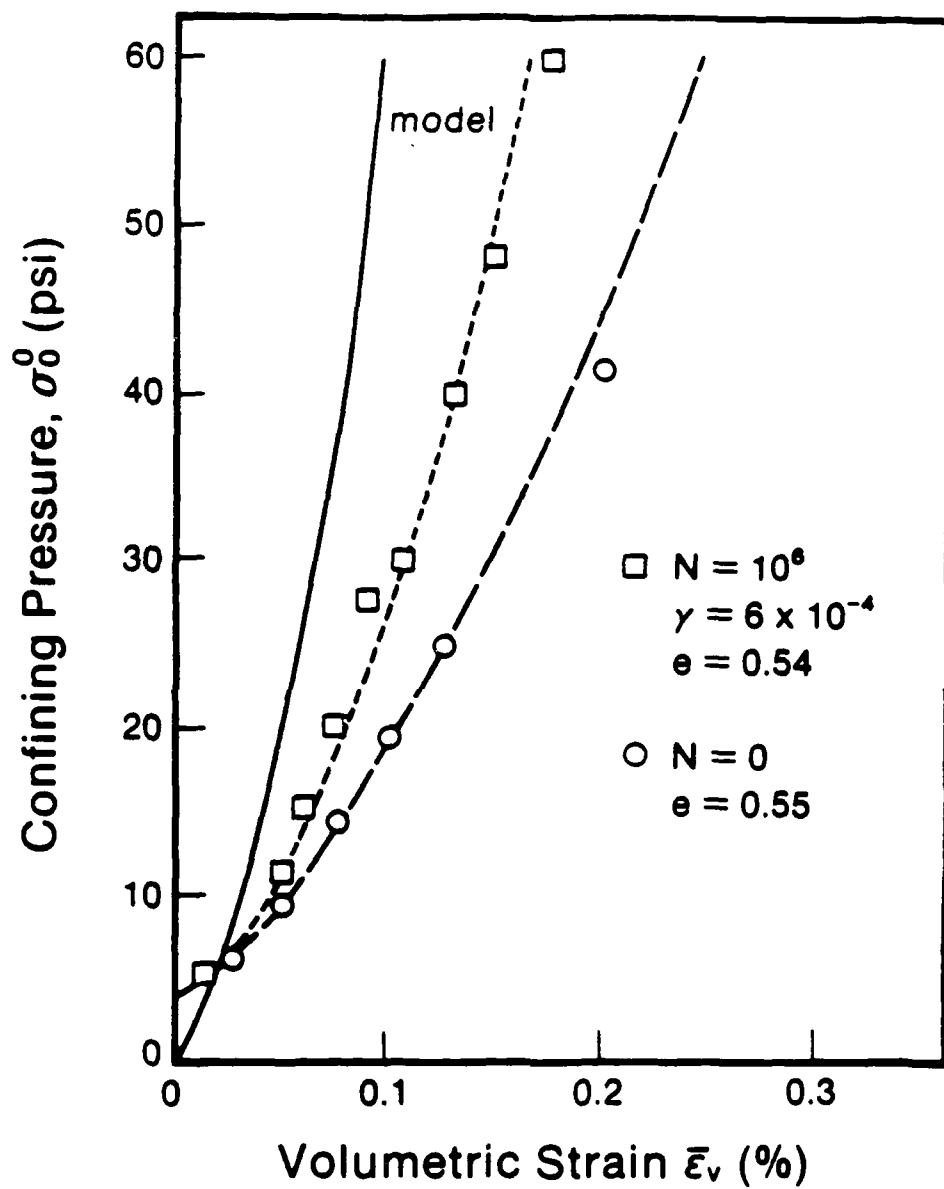


Figure 23. Isotropic Confining Pressure versus Volumetric Strain: Analytical and Experimental Results for  $e = 0.54$ .

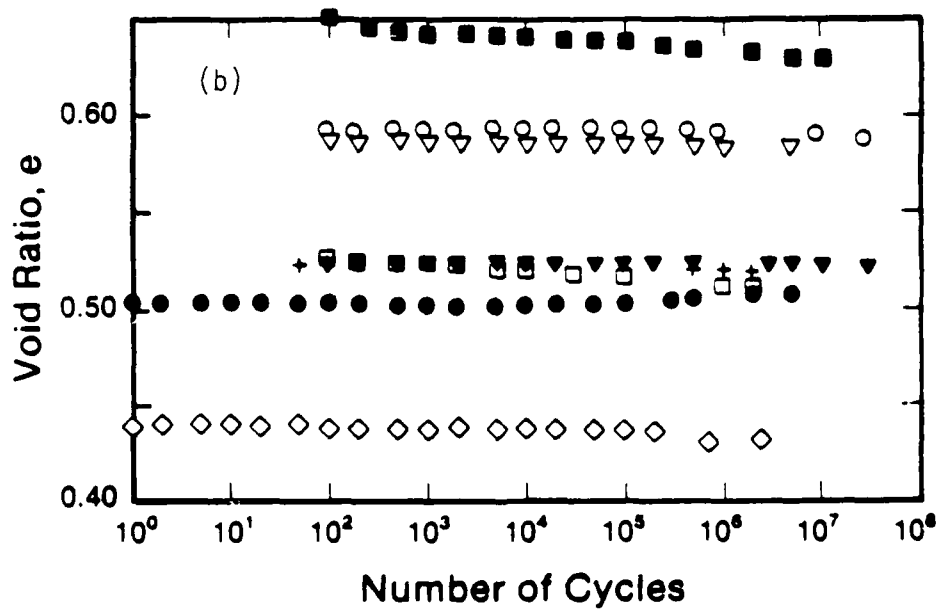
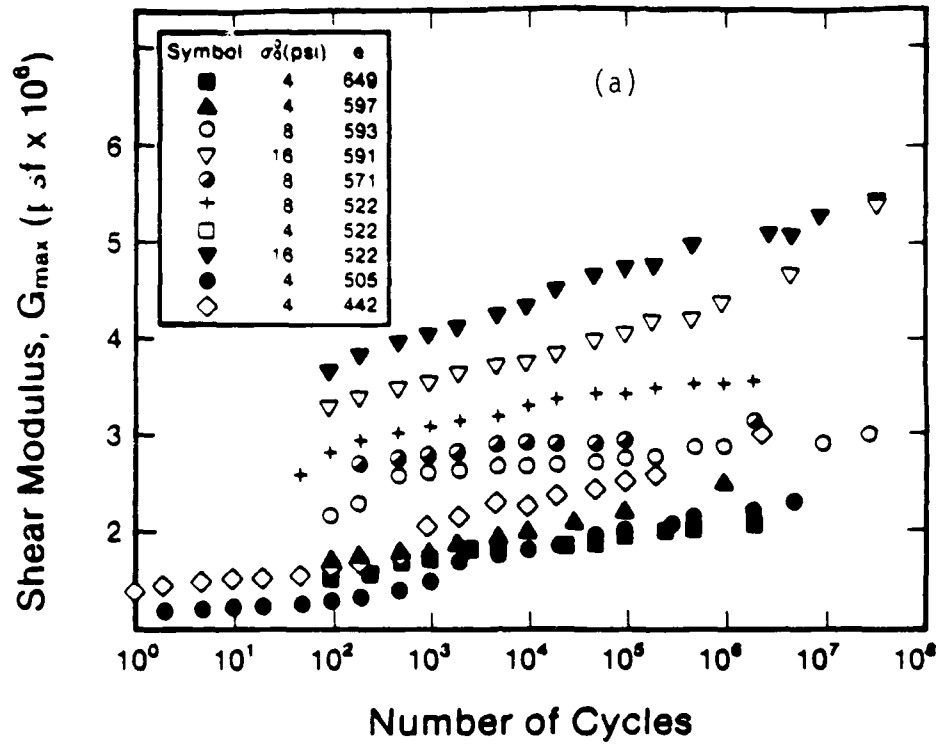


Figure 24. (a) Small Strain Shear Modulus,  $G_{max}$ , and (b) Void Ratio, versus Number of Cycles of Prestrain – Solid Cylindrical Samples (Song and Stokoe 1987).



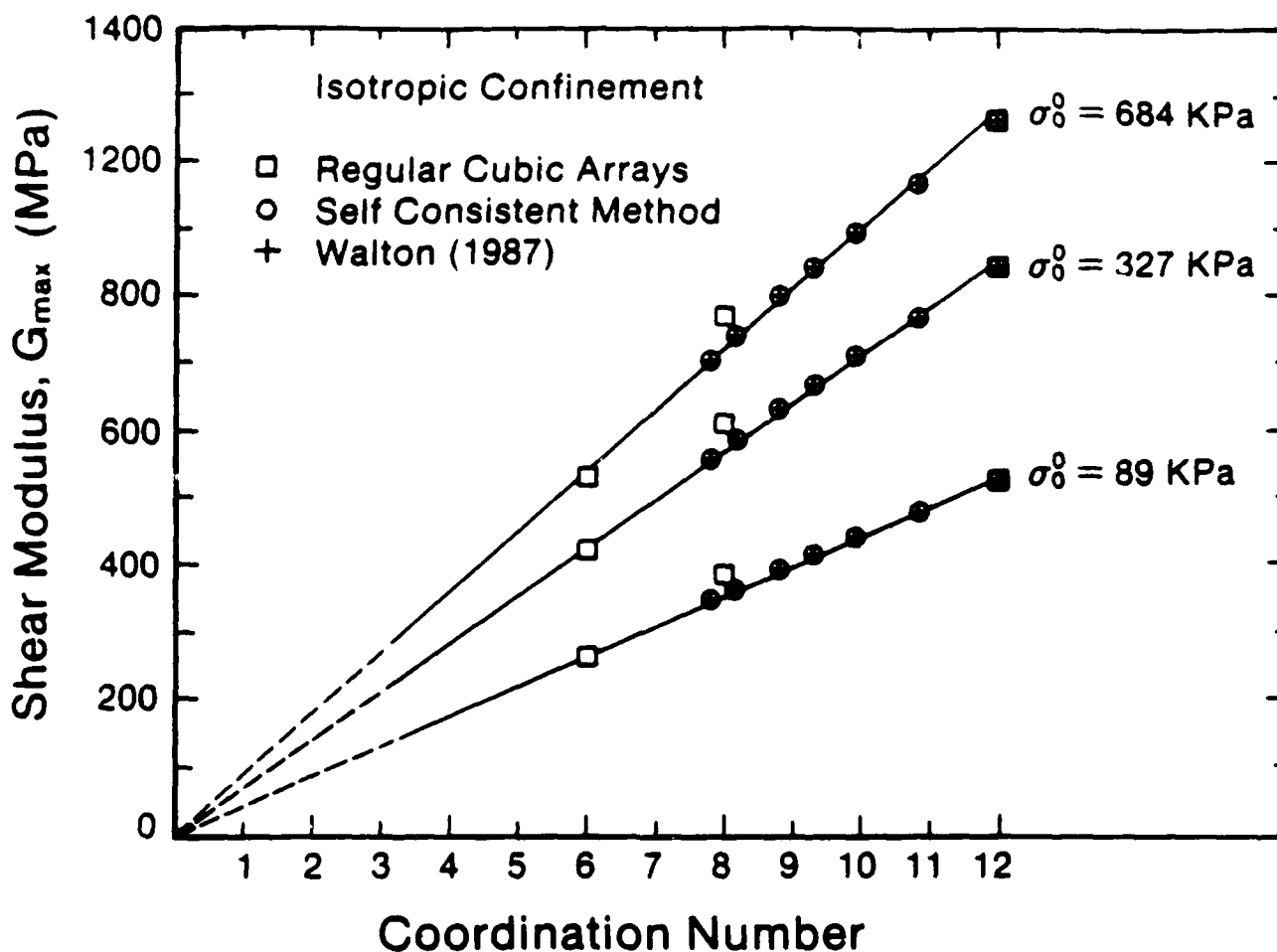


Figure 25. Shear Modulus,  $G_{\max}$ , versus Coordination Number for: (a) Regular Arrays and (b) Random Arrays of a Given Porosity by the Self-Consistent Method and the Analytical Expressions of Walton (1987). All Spheres have been Assigned the Properties of Quartz.

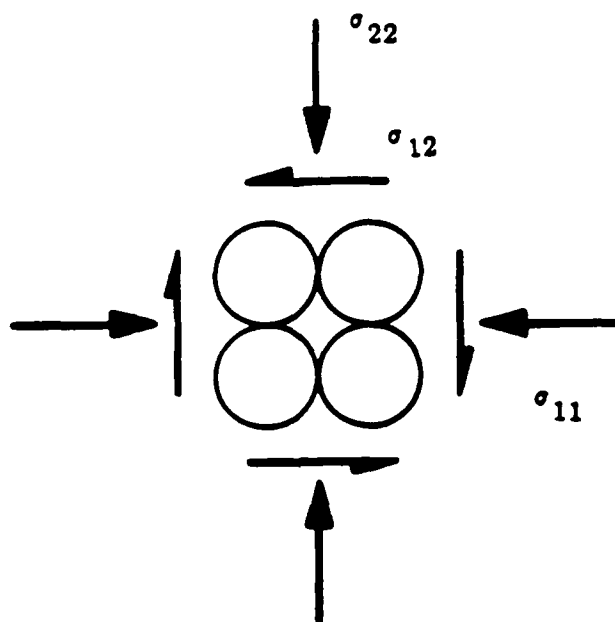


Figure 26. Stress State on a Simple Cubic Array of Identical Spheres.

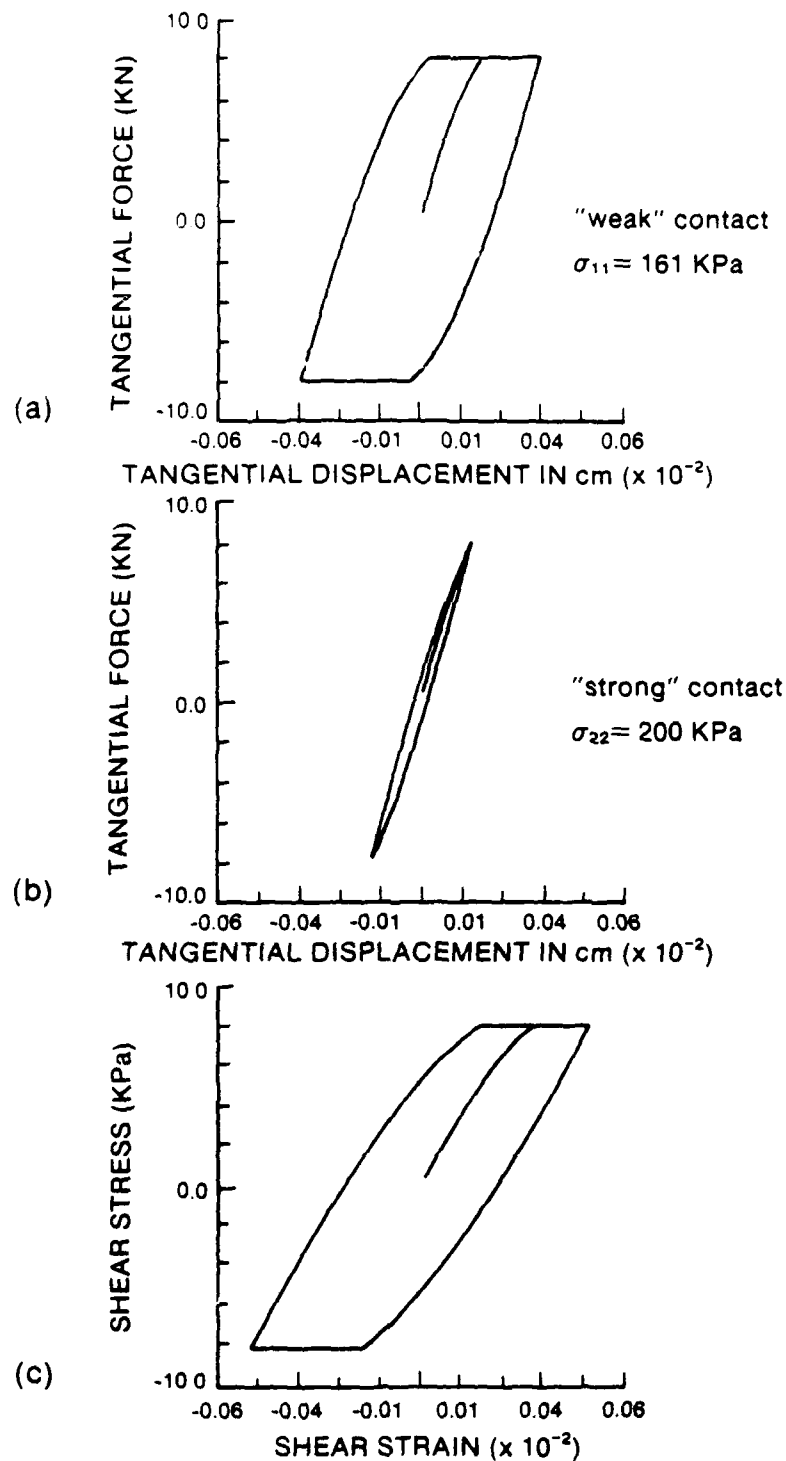


Figure 27. Stress-Strain Behavior, (c), of a simple Cubic Array of Quartz Spheres Subjected to Biaxial Stress,  $\sigma_{11} = 161$ ,  $\sigma_{22} = 200$  KPa, Followed by Pure Shear,  $\sigma_{12}$ , to failure. (a) and (b) Portray the Corresponding Force-Deformation Behavior of the "weak" and "strong" contact, respectively.

E13	E14	E15	E16
60°	50°	30°	40°
E9	E10	E11	E12
20°	80°	70°	20°
E5	E6	E7	E8
80°	70°	10°	30°
E1	E2	E3	E4
10°	50°	60°	20°

medium 1

E13	E14	E15	E16
20°	80°	30°	10°
E9	E10	E11	E12
40°	50°	60°	40°
E5	E6	E7	E8
60°	10°	20°	70°
E1	E2	E3	E4
70°	30°	80°	50°

medium 3

E13	E14	E15	E16
30°	60°	70°	50°
E9	E10	E11	E12
40°	80°	20°	80°
E5	E6	E7	E8
20°	30°	60°	10°
E1	E2	E3	E4
70°	10°	40°	50°

medium 2

10°	50°	30°	40°	70°	80°	60°	20°
20°	70°	50°	10°	30°	50°	70°	60°
30°	40°	60°	70°	10°	60°	50°	30°
10°	20°	80°	50°	40°	30°	40°	80°
80°	30°	40°	70°	80°	70°	60°	50°
60°	10°	20°	60°	40°	50°	10°	40°
20°	40°	30°	80°	50°	20°	80°	70°
30°	60°	20°	10°	70°	10°	20°	80°

medium 4

Figure 28. 16 and 64 Element Media Used in the Simulations.

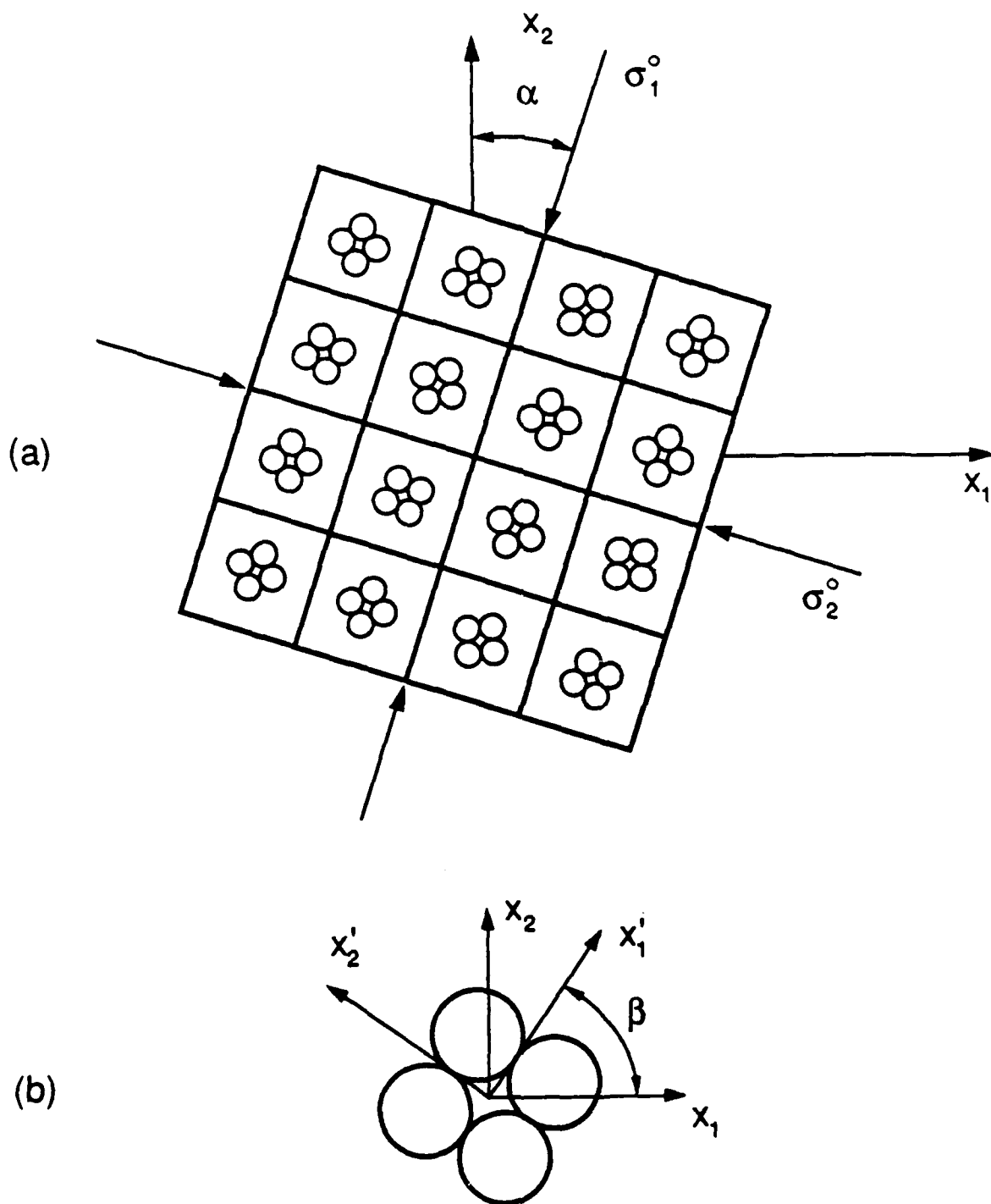


Figure 29. (a) Orientation of the Applied Principal Stresses During Pure Shear Loading with Mean Stress Constant,  $\sigma_m^o = 0.5(\sigma_1^o + \sigma_2^o) = \text{constant}$ , and (b) orientation of an element.

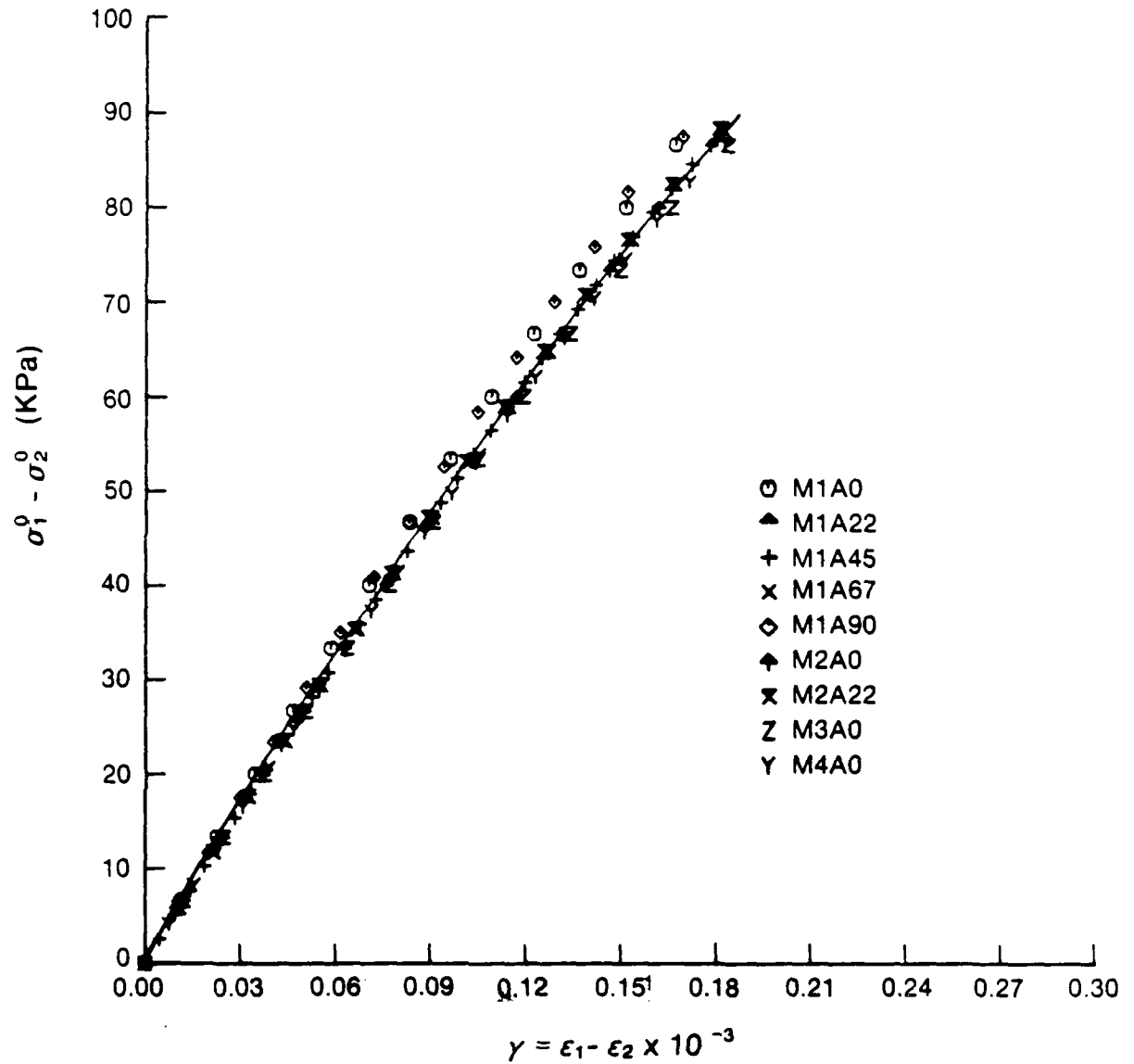


Figure 30. Difference in Applied Principal Stresses,  $\sigma_1^0 - \sigma_2^0$ , versus Shear Strain,  $\gamma = \epsilon_1 - \epsilon_2$ , Calculated for all Media (16 and 64 elements), and for Values of  $\alpha = 0^\circ, 22.5^\circ, 45^\circ, 67.5^\circ$ , and  $90^\circ$  (MX = medium X, AYY = inclination of  $\sigma_1$  is YY degrees).

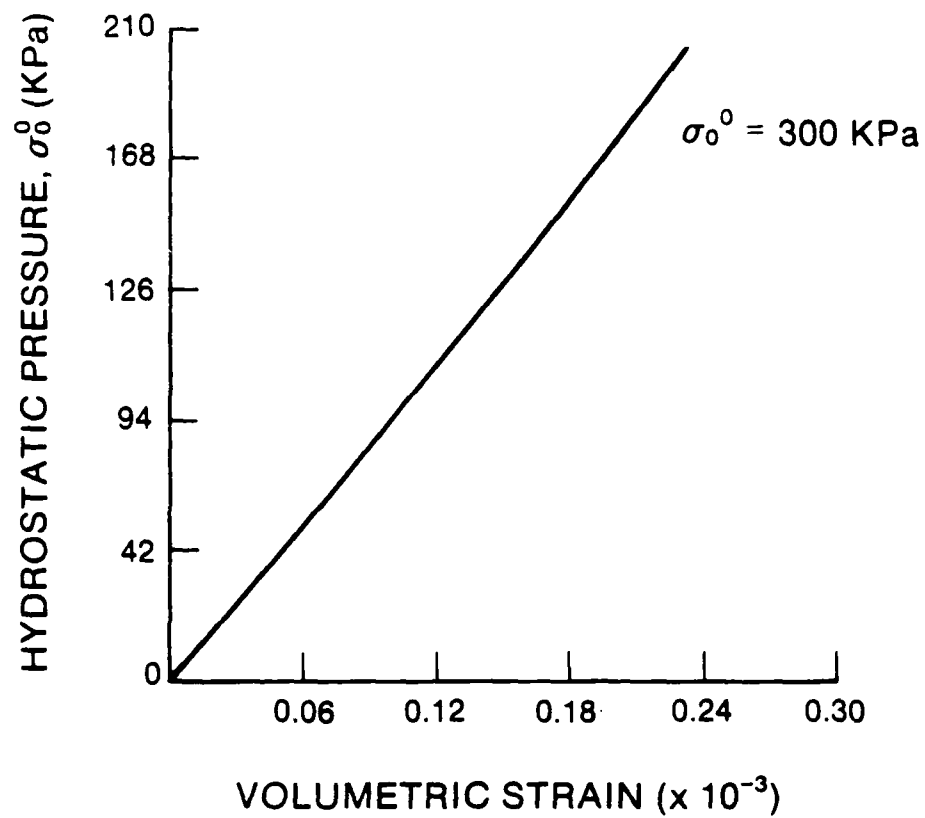


Figure 31. Medium 1: Stress-Strain Behavior for Hydrostatic Compression Loading Starting from  $\sigma_0^0 = 300$  KPa.

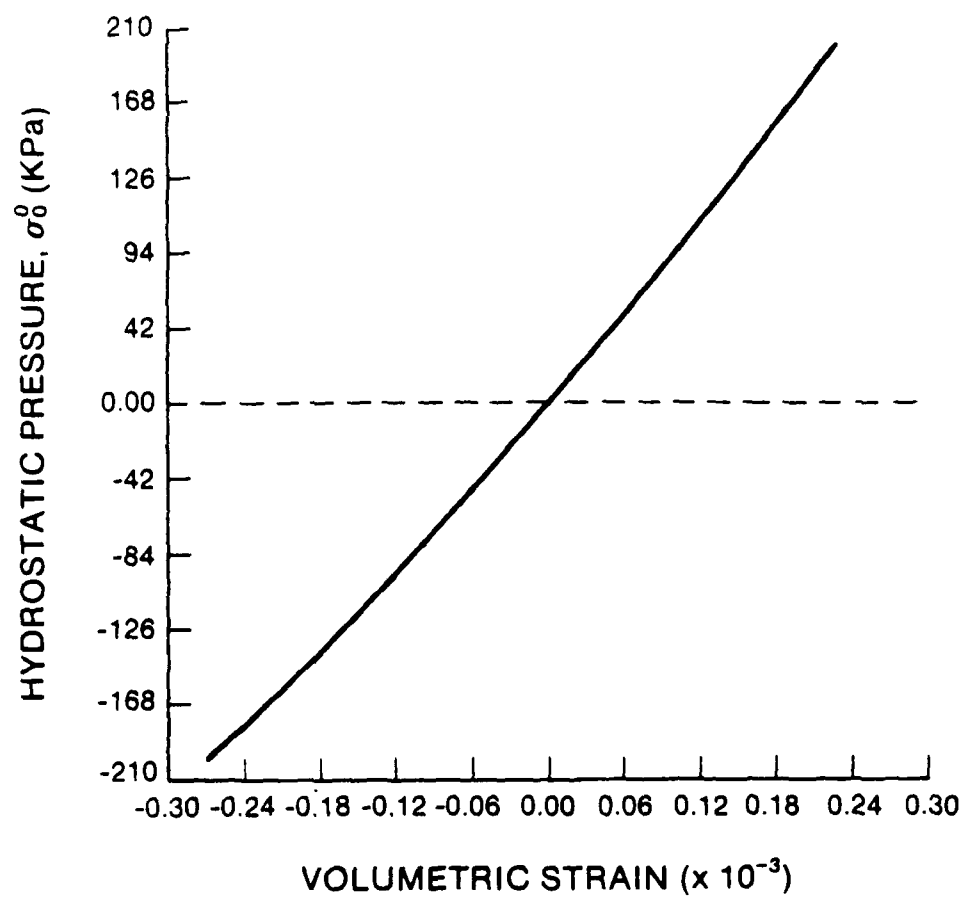


Figure 32. Medium 1: Stress-Strain Behavior for Cyclic Isotropic Loading,  $\sigma_o^o \pm \Delta\sigma_o^o$ , with  $\sigma_o^o = 300$  KPa and  $\Delta\sigma_o^o = 200$  KPa.



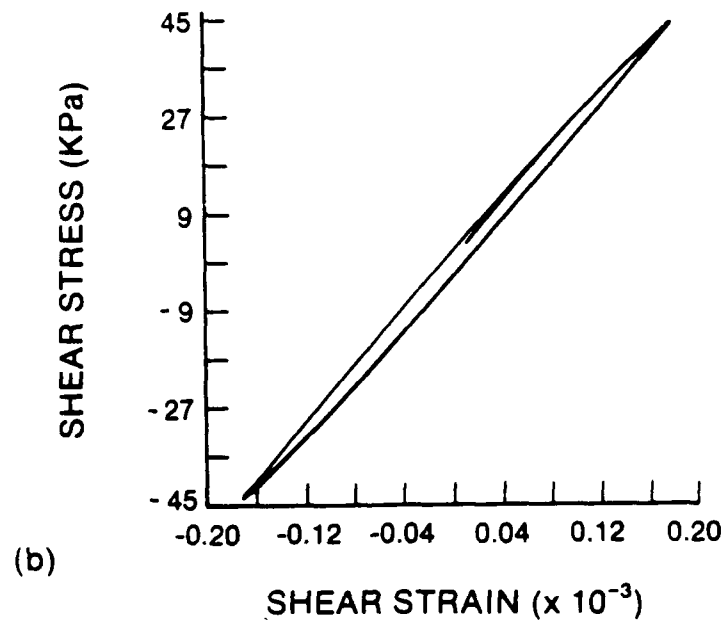
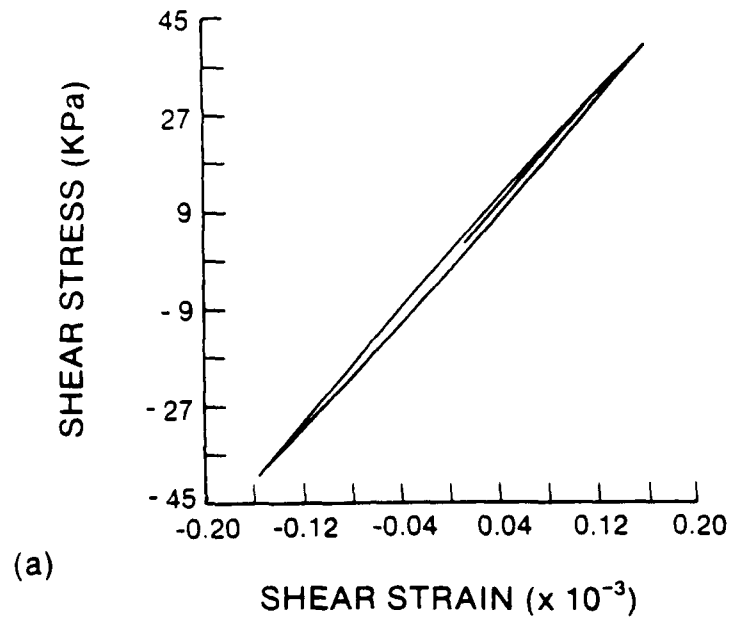


Figure 33. Medium 1: Stress-Strain Behavior for Cyclic Pure Shear Loading Following Isotropic Compression,  $\sigma_0 = 100$  KPa. (a)  $\gamma_c = 40$  KPa and, (b)  $\gamma_c = 43$  KPa.

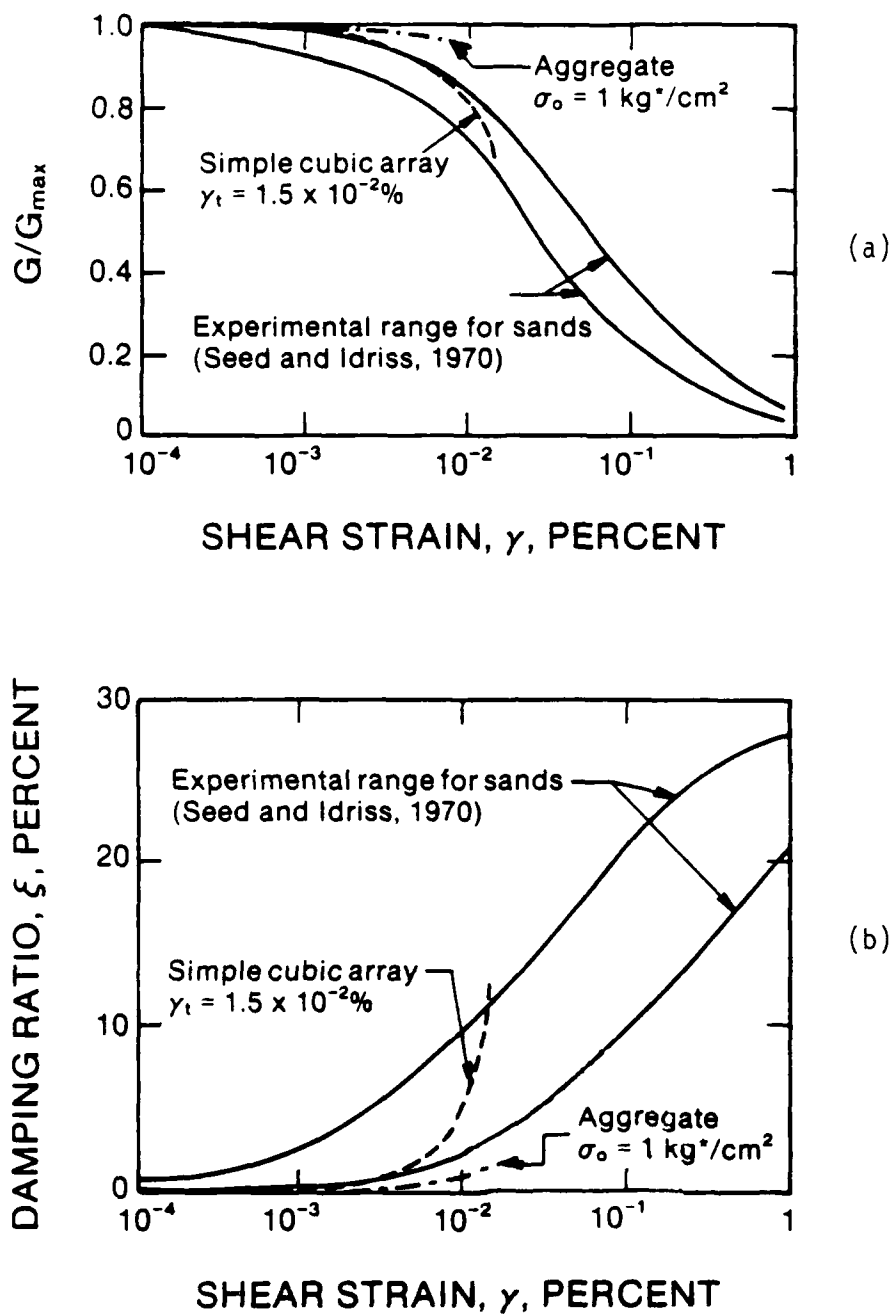


Figure 34. Normalized Shear Modulus,  $G/G_{\max}$ , (a), and Damping ratio  $\xi$ , (b), versus Shear Strain,  $\gamma$ . Comparison Between Values Measured in Sand, the Simulated Aggregate and Simple Cubic Array in Pure Shear.

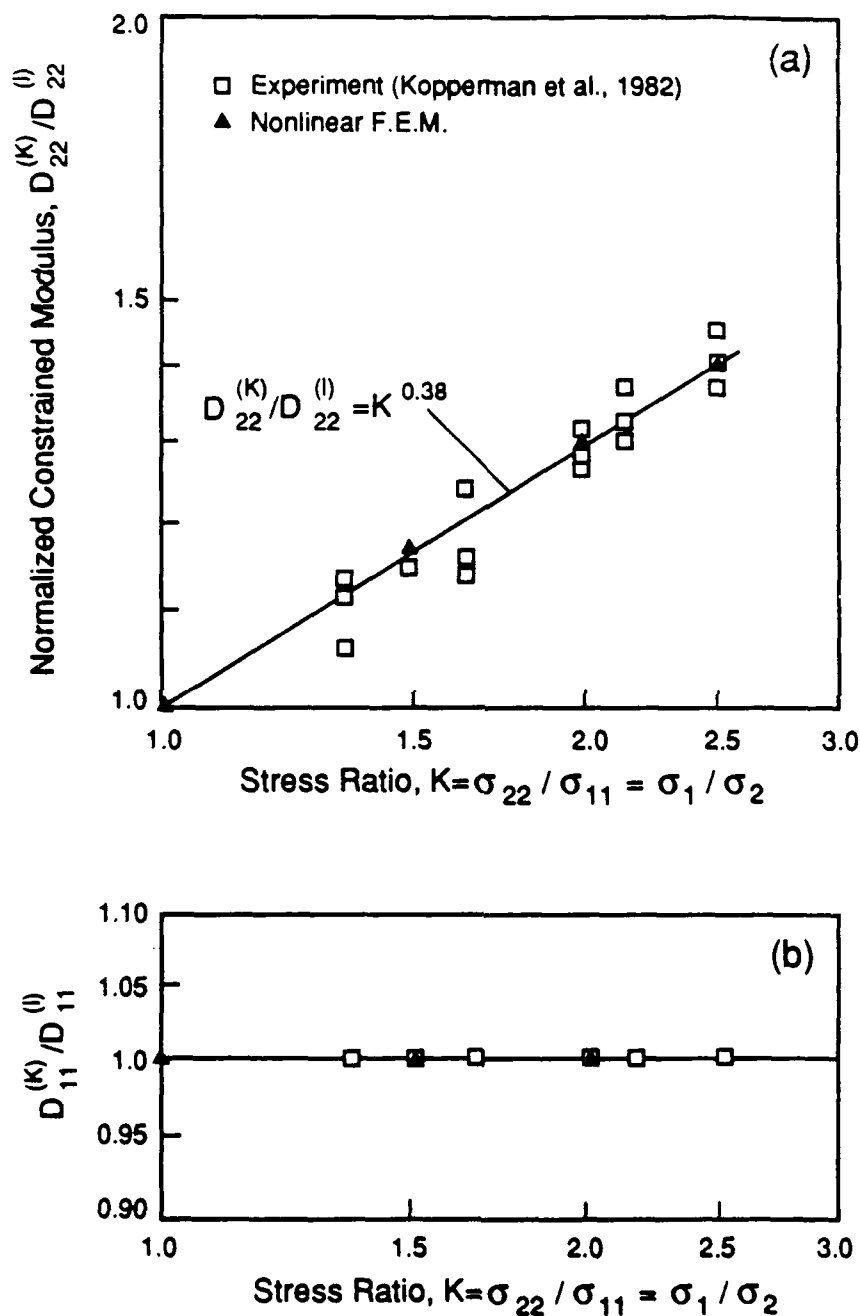


Figure 35. Normalized Constrained Moduli,  $D_{11}^{(K)}/D_{11}^{(I)}$  versus Stress Ratio,  $K = \sigma_1/\sigma_2$ . Comparison Between Analytical and Experimental Results (a) in the Direction of  $\sigma_1$ , and (b) in the Direction of  $\sigma_2$  ( $\sigma_2$  is kept constant).

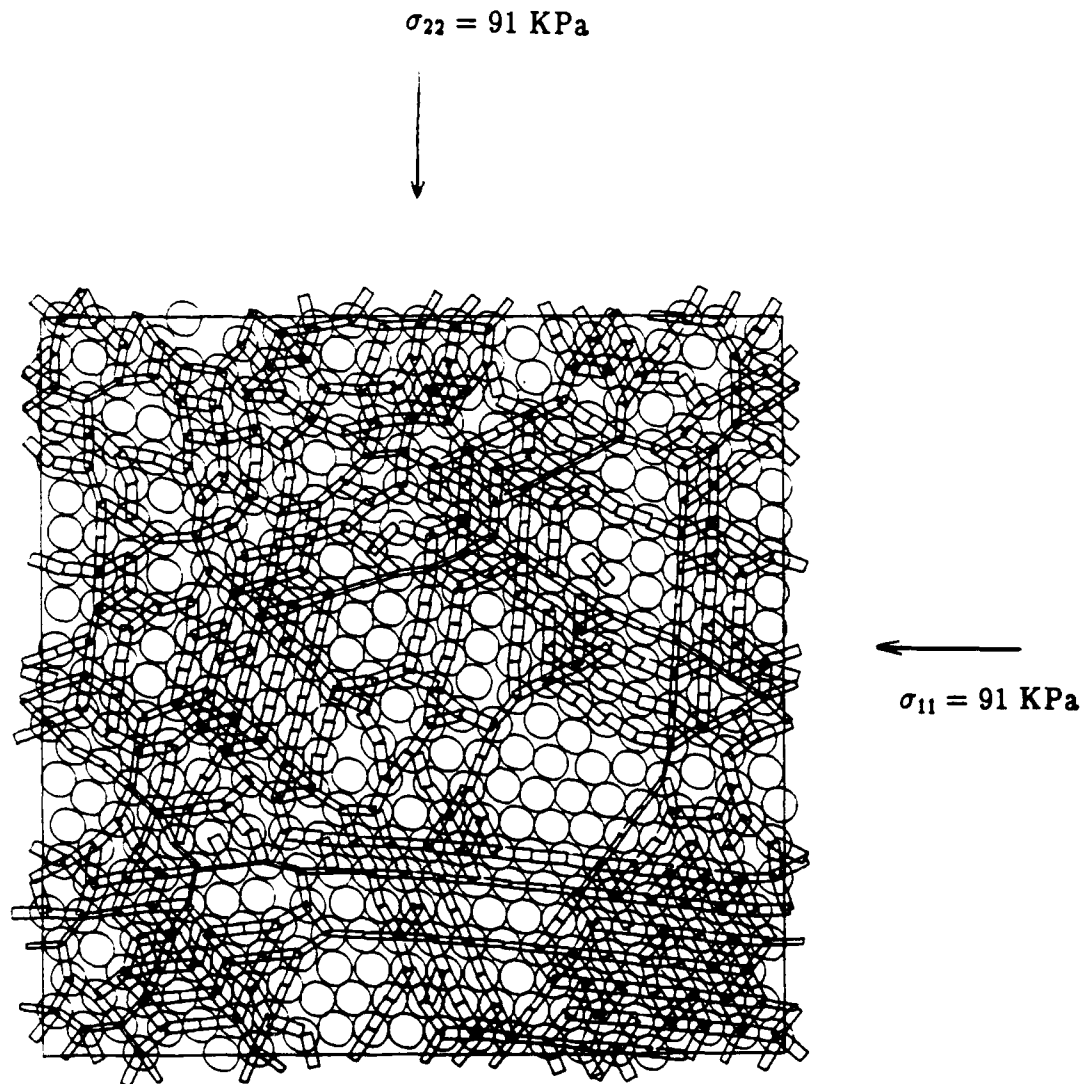
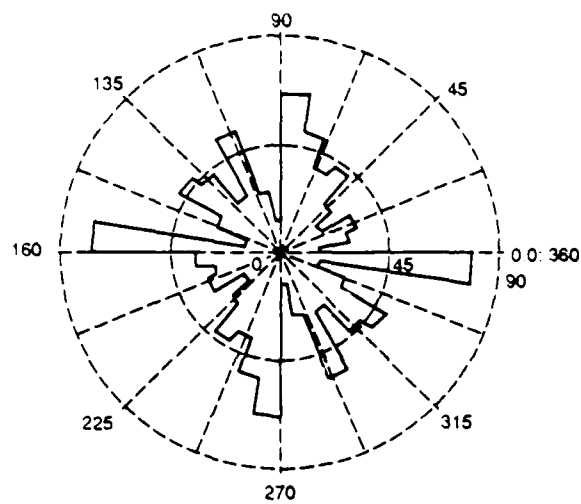
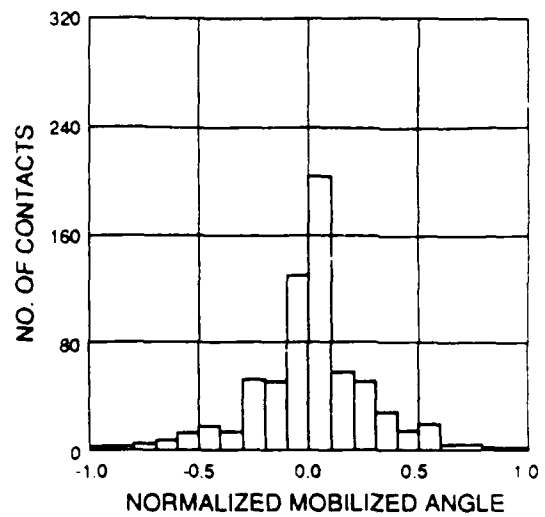


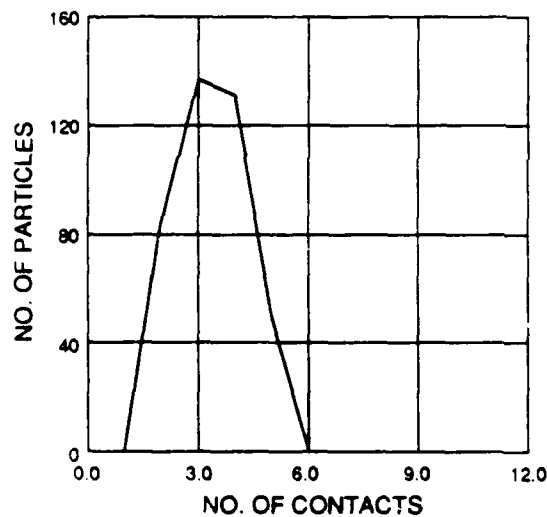
Figure 36. 2-D Random Array of 477 Equal, Elastic, Rough, Quartz Spheres Subjected to Isotropic Compression,  $\sigma = 91 \text{ KPa}$ . Note that this Figure Represents the "Window" with the Representative Random Pattern.



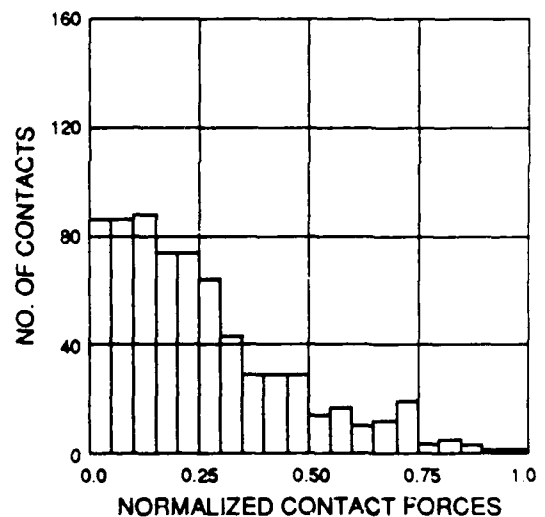
FREQUENCY DISTRIBUTION  
OF CONTACT ANGLE



FREQUENCY DISTRIBUTION  
OF MOBILIZED ANGLE



FREQUENCY DISTRIBUTION  
OF CONTACT PER PARTICLE



FREQUENCY DISTRIBUTION  
OF CONTACT FORCE

Figure 37. Statistical Information Regarding the isotropic Compression at  $\sigma_0 = 91$  KPa of the 477-sphere medium of Figure 36.

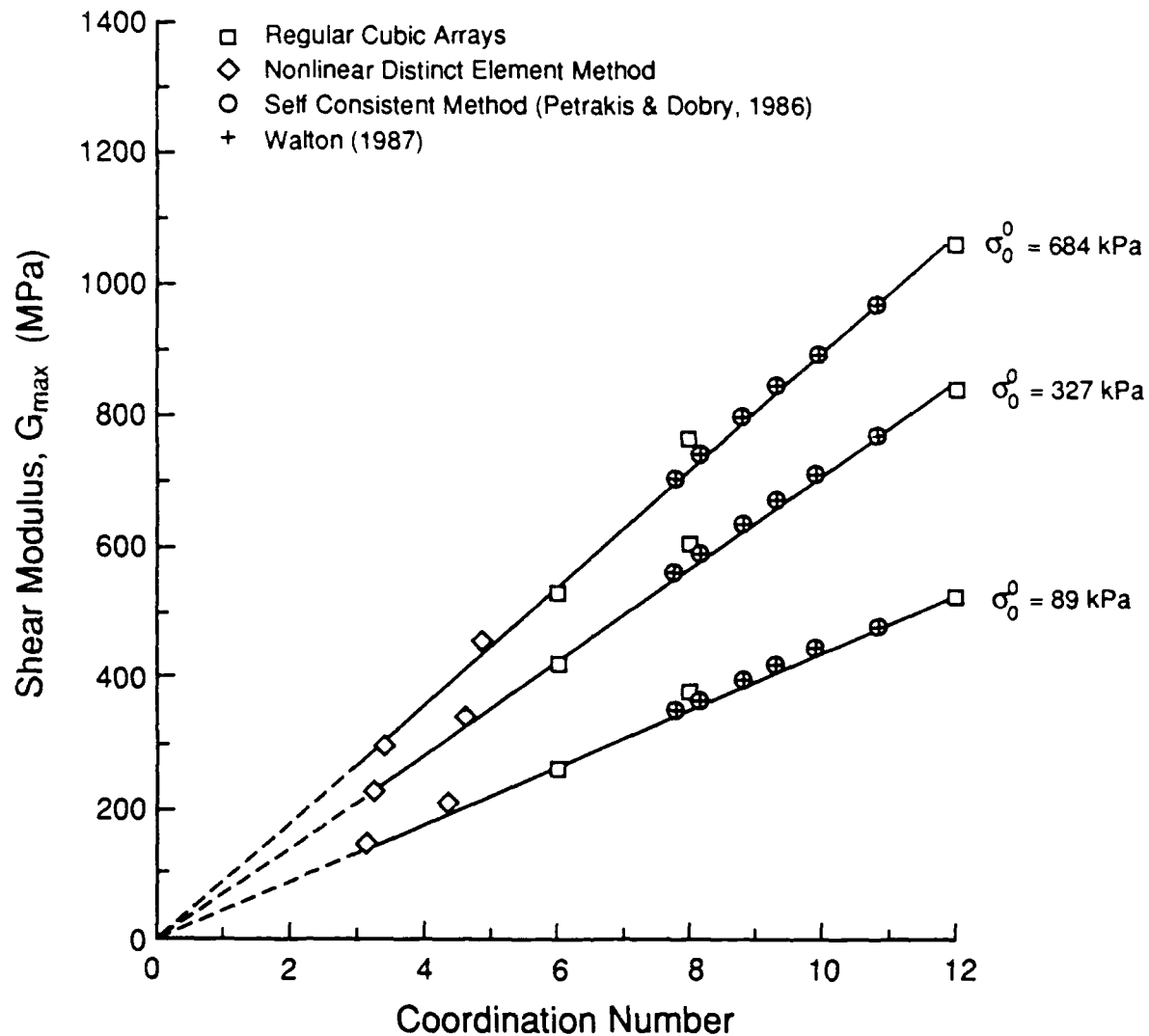


Figure 38. Shear Modulus,  $G_{\max}$ , vs Coordination Number for : i) Two Random Arrays of 477 Equal Spheres, ii) Regular Arrays, and iii) Random Arrays of a given porosity by the Self Consistent Method and the analytical expressions of Walton (1987).

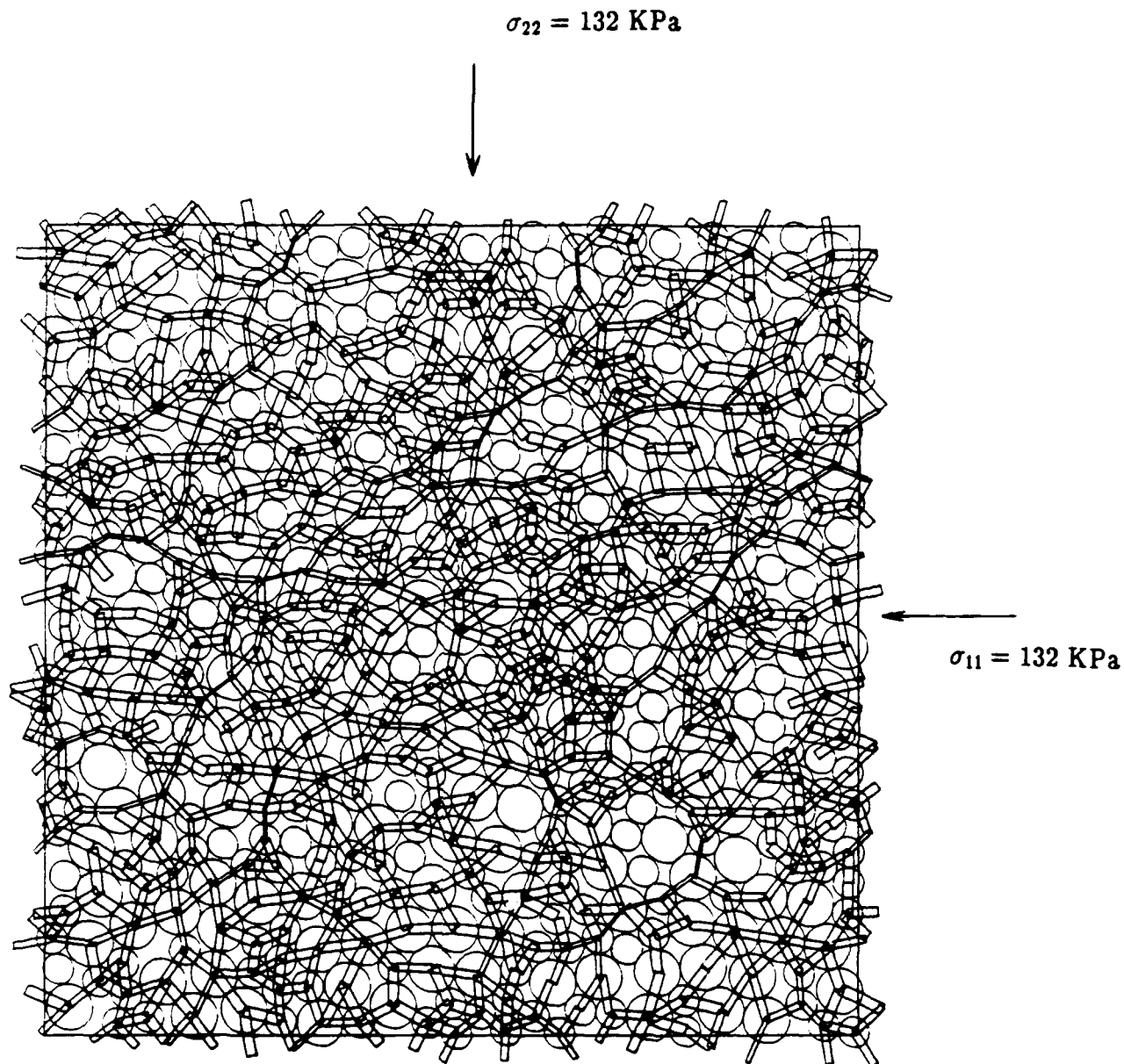
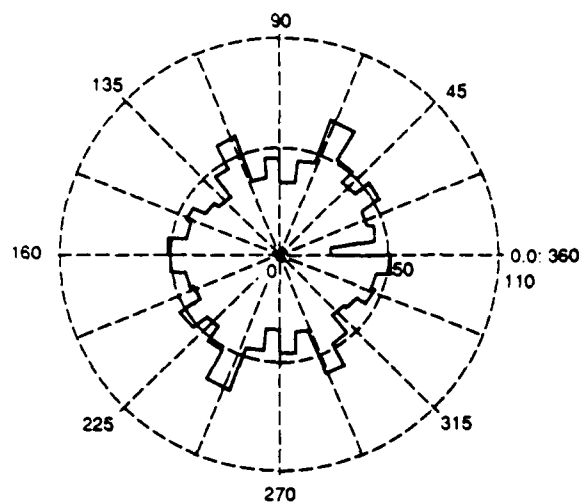
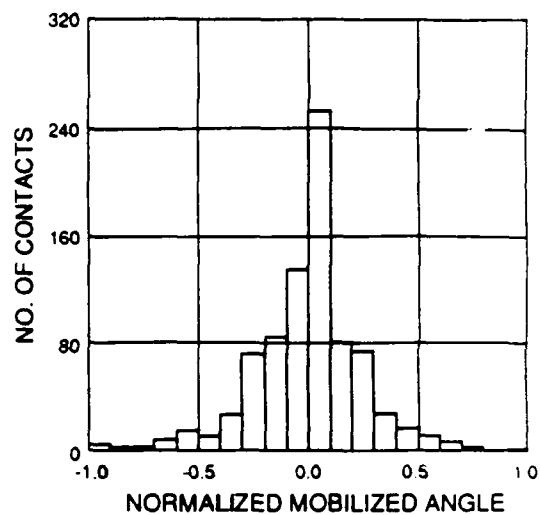


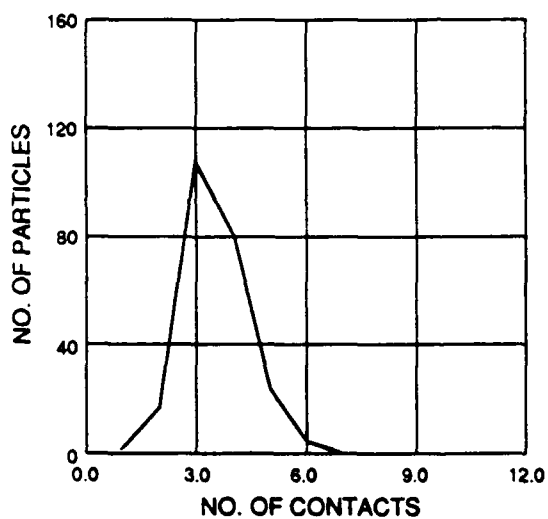
Figure 39. 2-D Random Array of 531 Elastic, Quartz Spheres of Two Radii ( $R_1/R_2 = 1.5$ ) Subjected to Isotropic Compression  $\sigma_0 = 132 \text{ KPa}$ .



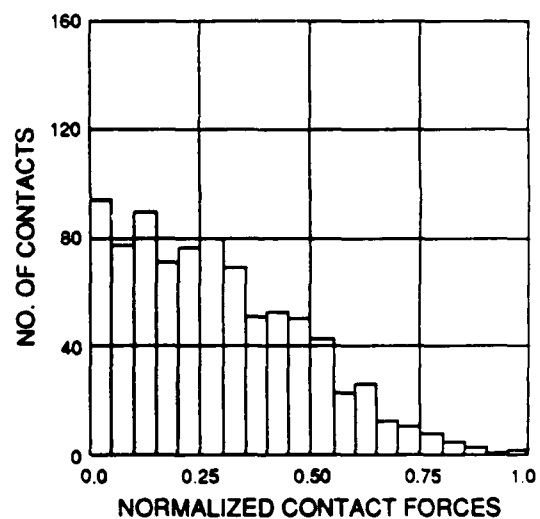
FREQUENCY DISTRIBUTION  
OF CONTACT ANGLE



FREQUENCY DISTRIBUTION  
OF MOBILIZED ANGLE



FREQUENCY DISTRIBUTION  
OF CONTACT PER PARTICLE



FREQUENCY DISTRIBUTION  
OF CONTACT FORCE

Figure 40. Statistical Information for the isotropic loading of Fig. 39.



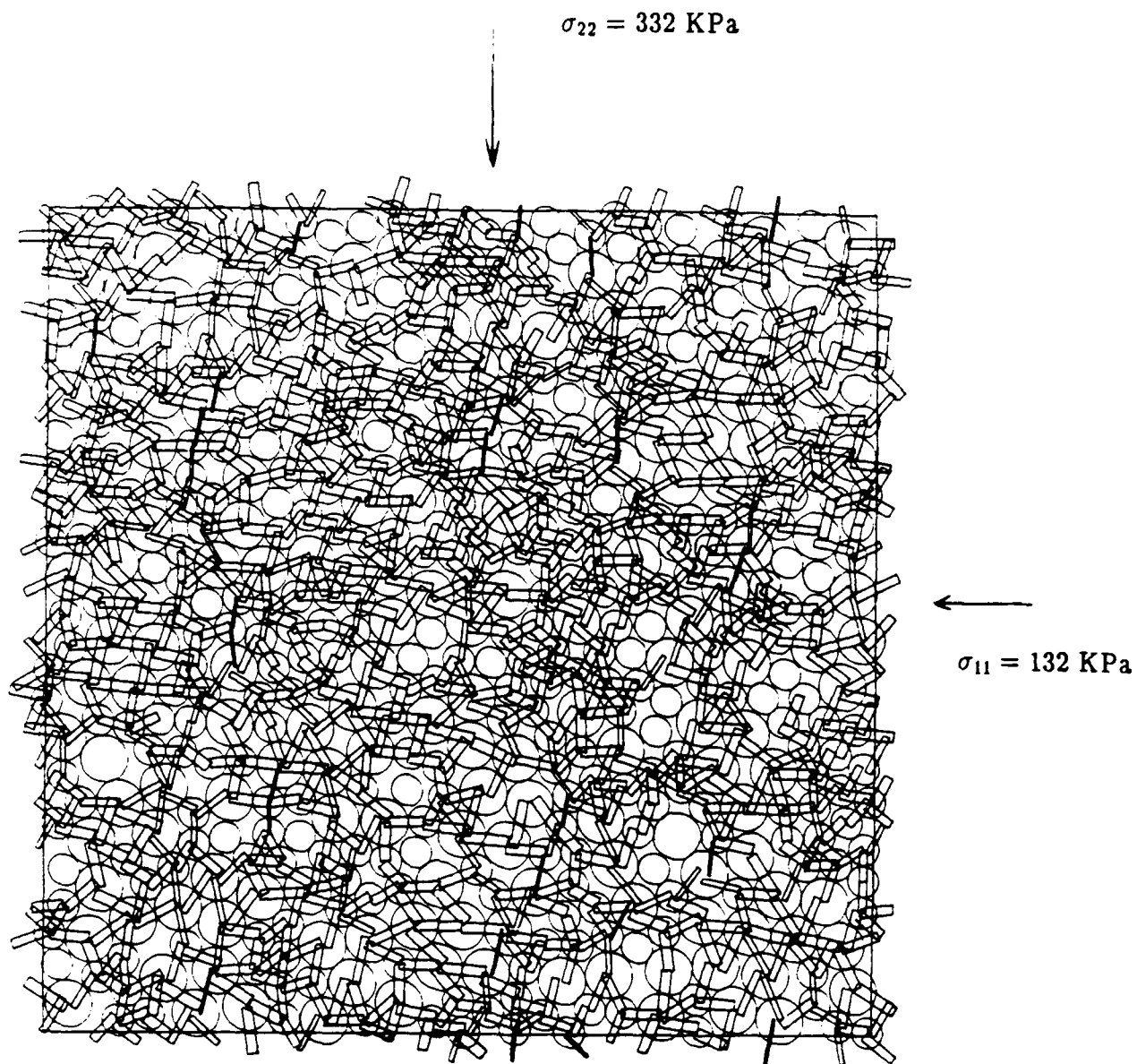
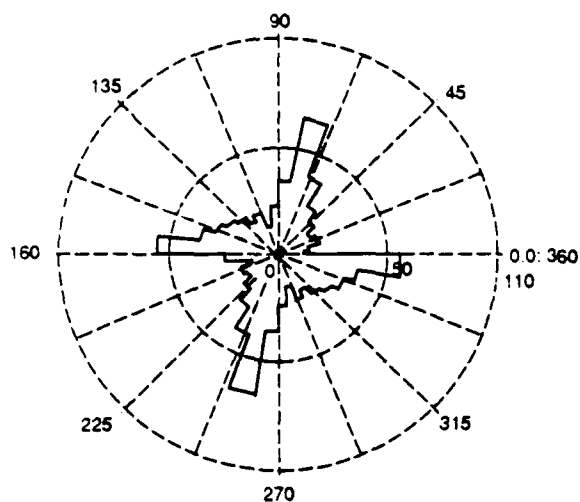
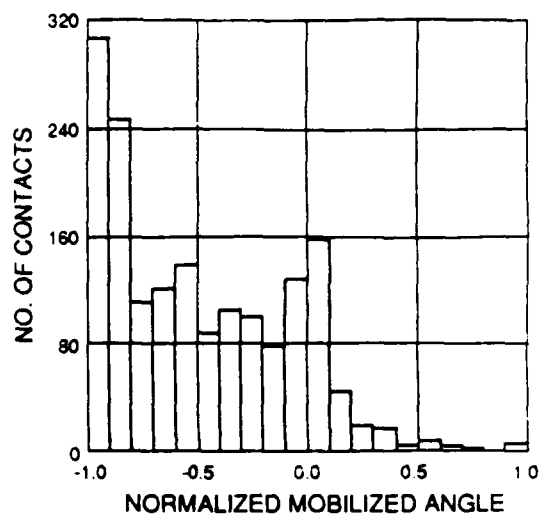


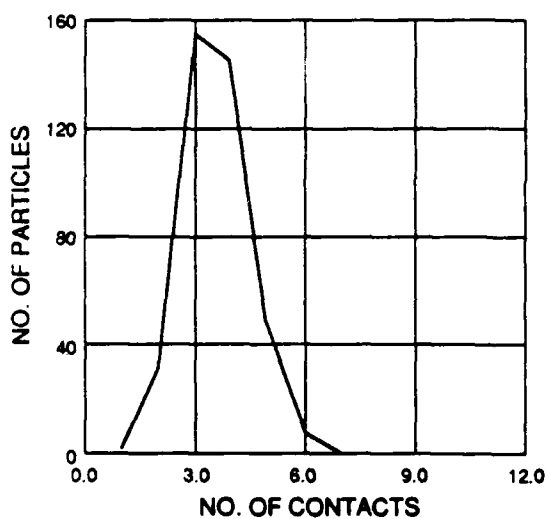
Figure 41. 2-D Random Array of 531 Elastic, Quartz Spheres of Two Radii ( $R_1/R_2 = 1.5$ ) Subjected to Biaxial Compression Loading.



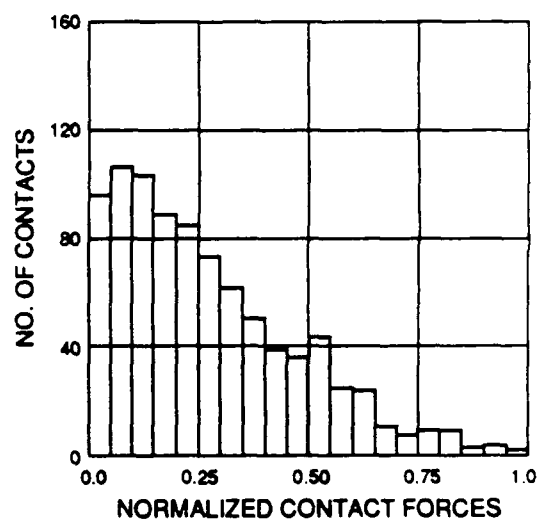
FREQUENCY DISTRIBUTION  
OF CONTACT ANGLE



FREQUENCY DISTRIBUTION  
OF MOBILIZED ANGLE



FREQUENCY DISTRIBUTION  
OF CONTACT PER PARTICLE



FREQUENCY DISTRIBUTION  
OF CONTACT FORCE

Figure 42. Statistical information for the biaxial compression loading in Fig. 41.

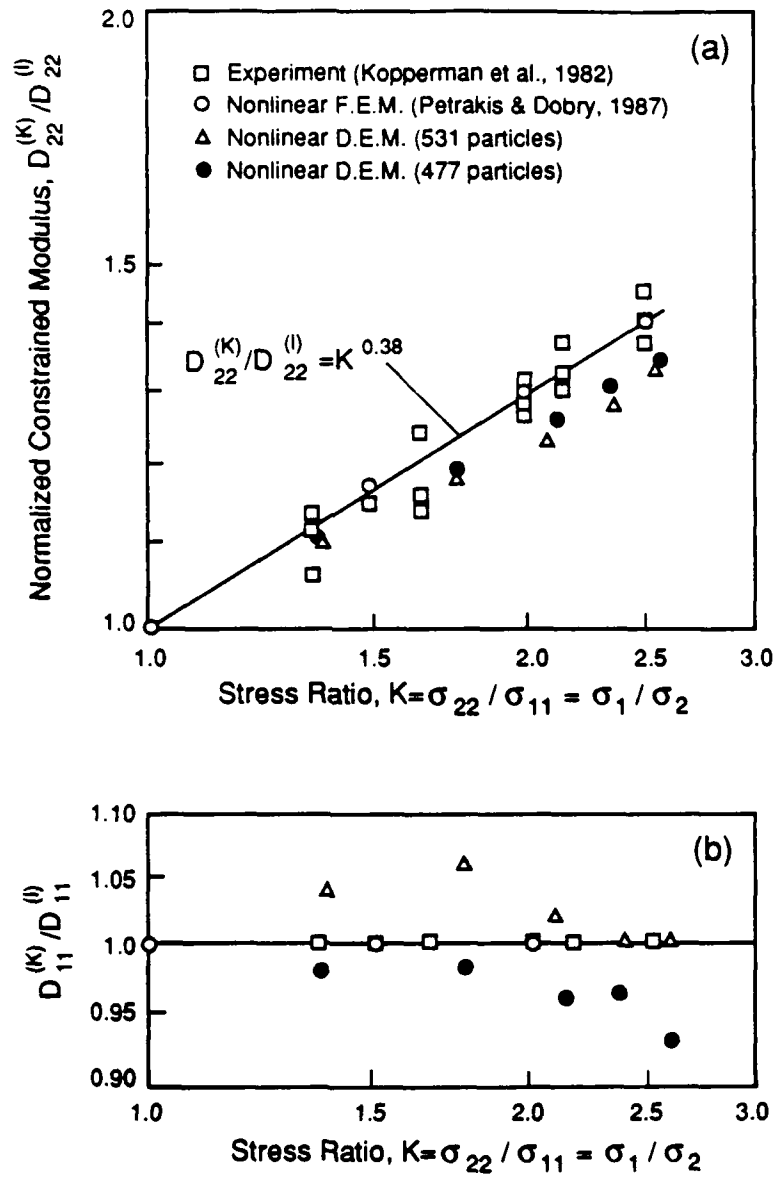


Figure 43. Normalized constrained moduli,  $D_{11}^{(K)} / D_{11}^{(1)}$ , vs stress ratio,  $K = \sigma_1 / \sigma_2$ , for all Distinct Element, Finite Element and Experimental results: (a) in the direction of  $\sigma_1$  and (b) in the direction of  $\sigma_2$  ( $\sigma_2$  is kept constant).

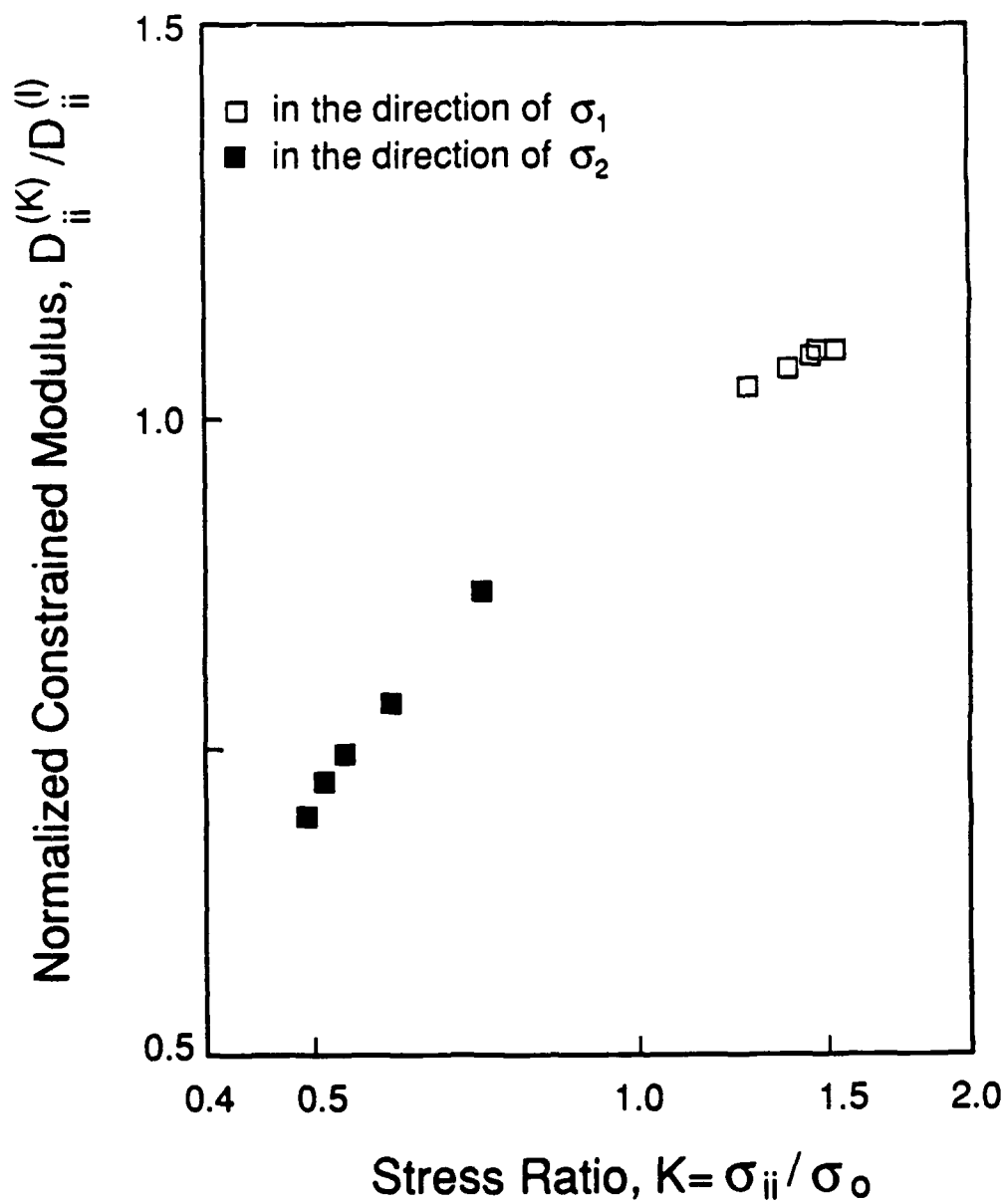


Figure 44. Normalized constrained moduli,  $D_{ii}^{(K)} / D_{ii}^{(1)}$  versus stress ratio,  $K = \sigma_{ii} / \sigma_0$ , for the case of biaxial compression-extension loading with constant mean stress,  $\sigma_0 = 91$  KPa.

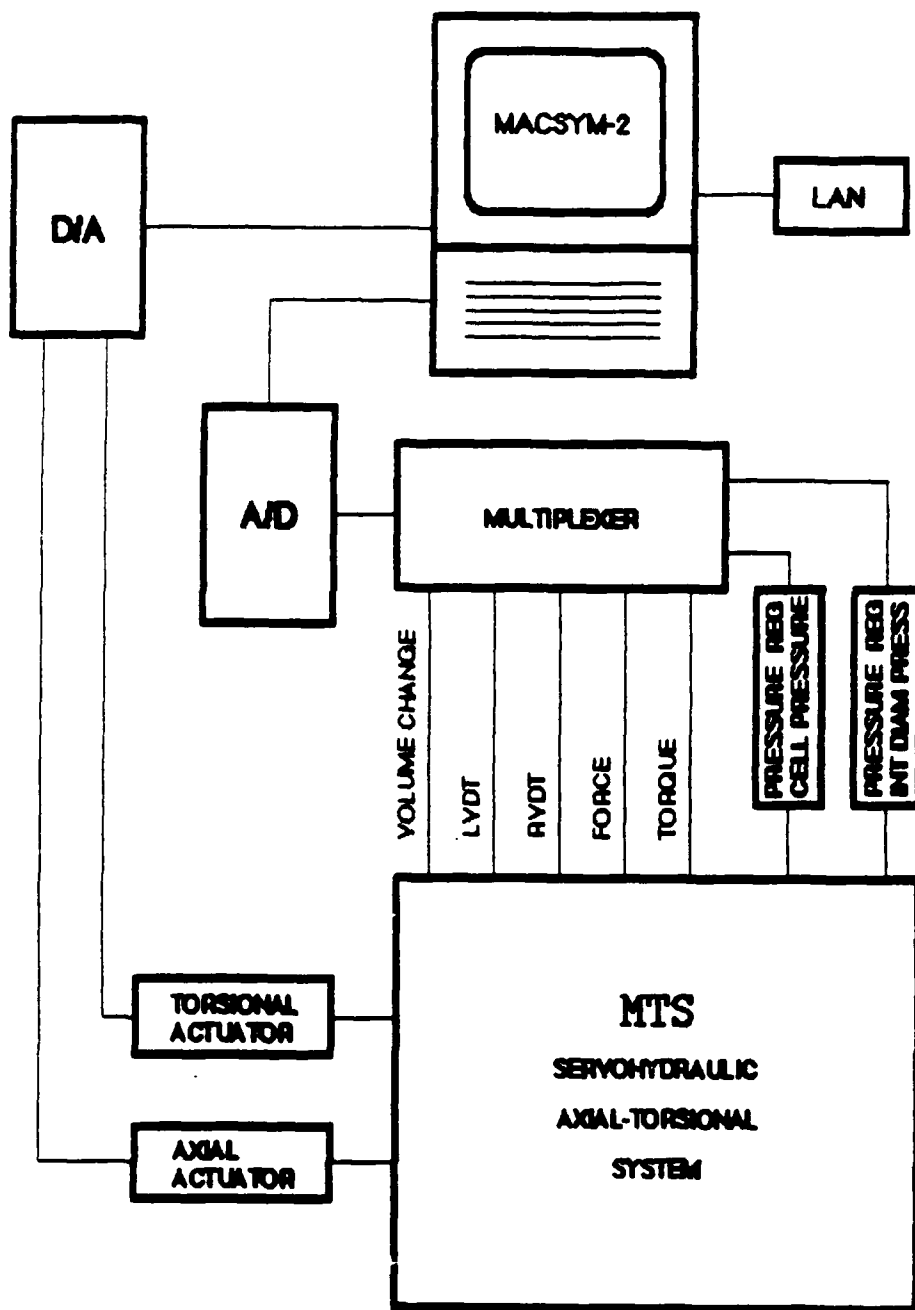


Figure 45. The RPI Soil Mechanics Laboratory MTS Servohydraulic Axial/Torsional and Computer control System Configuration.

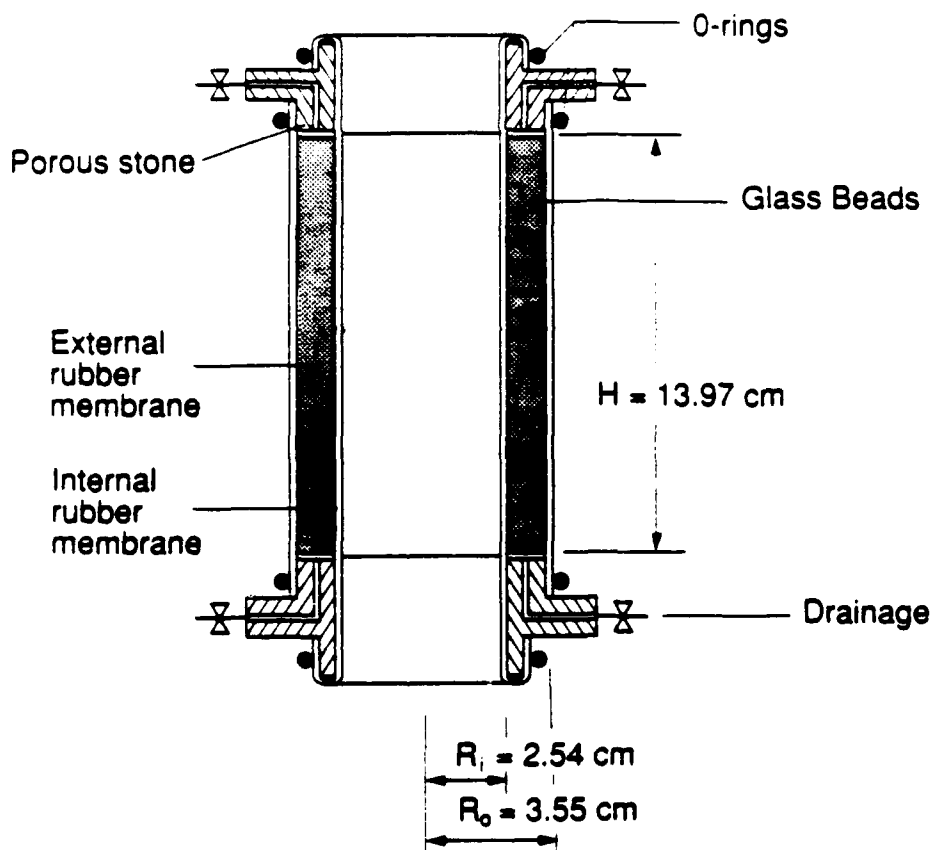


Figure 46. Sketch of Hollow Cylindrical Specimen Used in this Study.

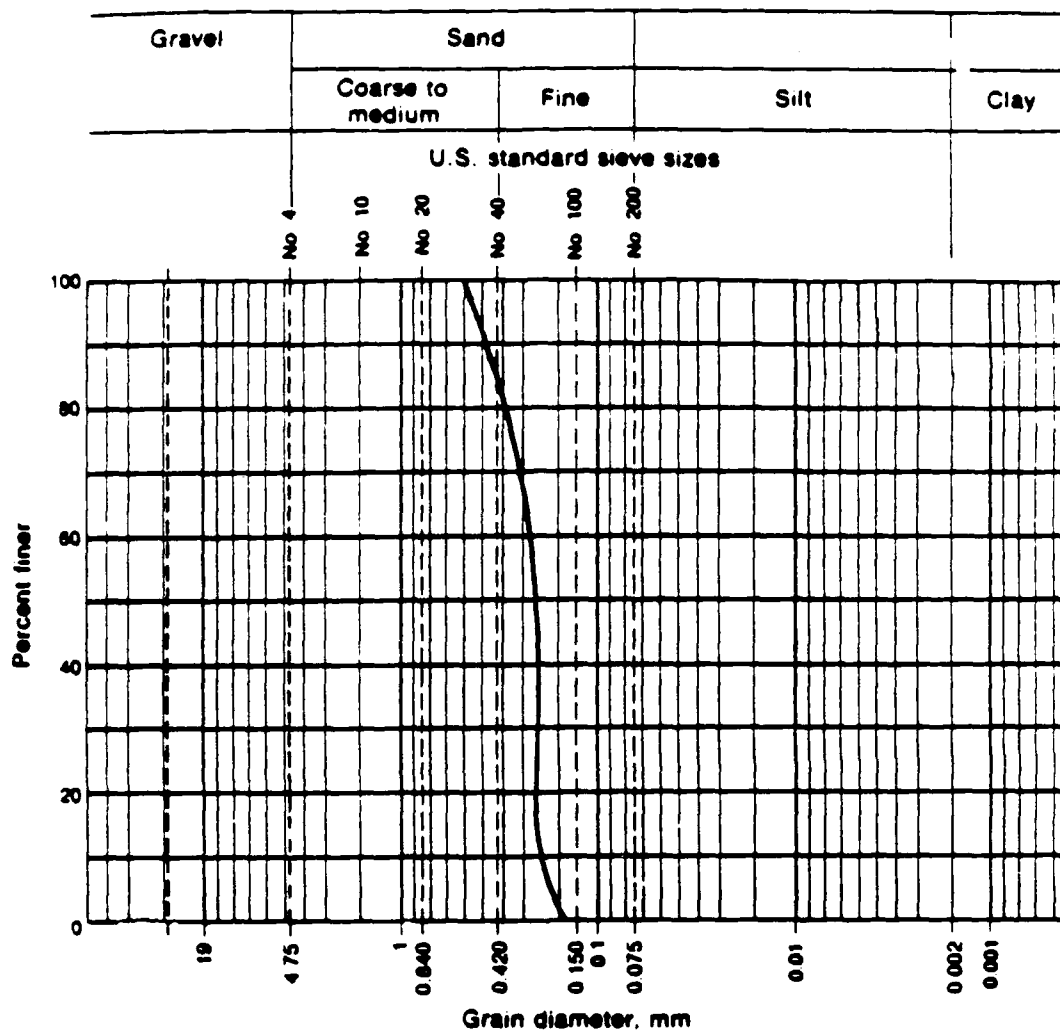


Figure 47. Grain Size Distribution Curve for Mixture of Glass Beads Used in this Study.

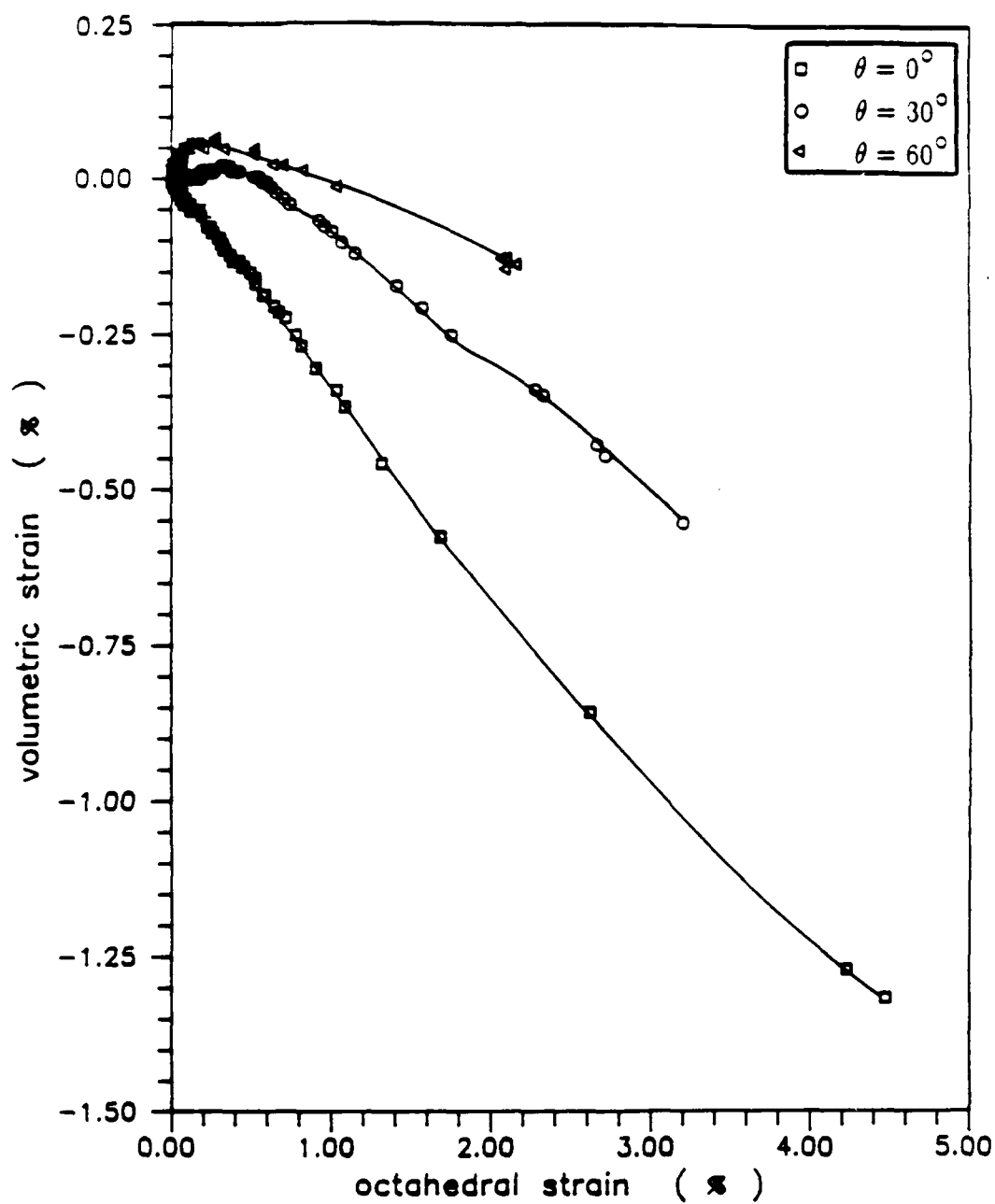


Figure 49. Volumetric Strain versus Octahedral Shear Strain for Monotonic Radial Shear Tests ( $\theta = 0^\circ, 30^\circ, \text{ and } 60^\circ$ ) on Assemblies of Different Sizes of Spheres. ( $\sigma_m \approx 140 \text{ KPa}$ ).



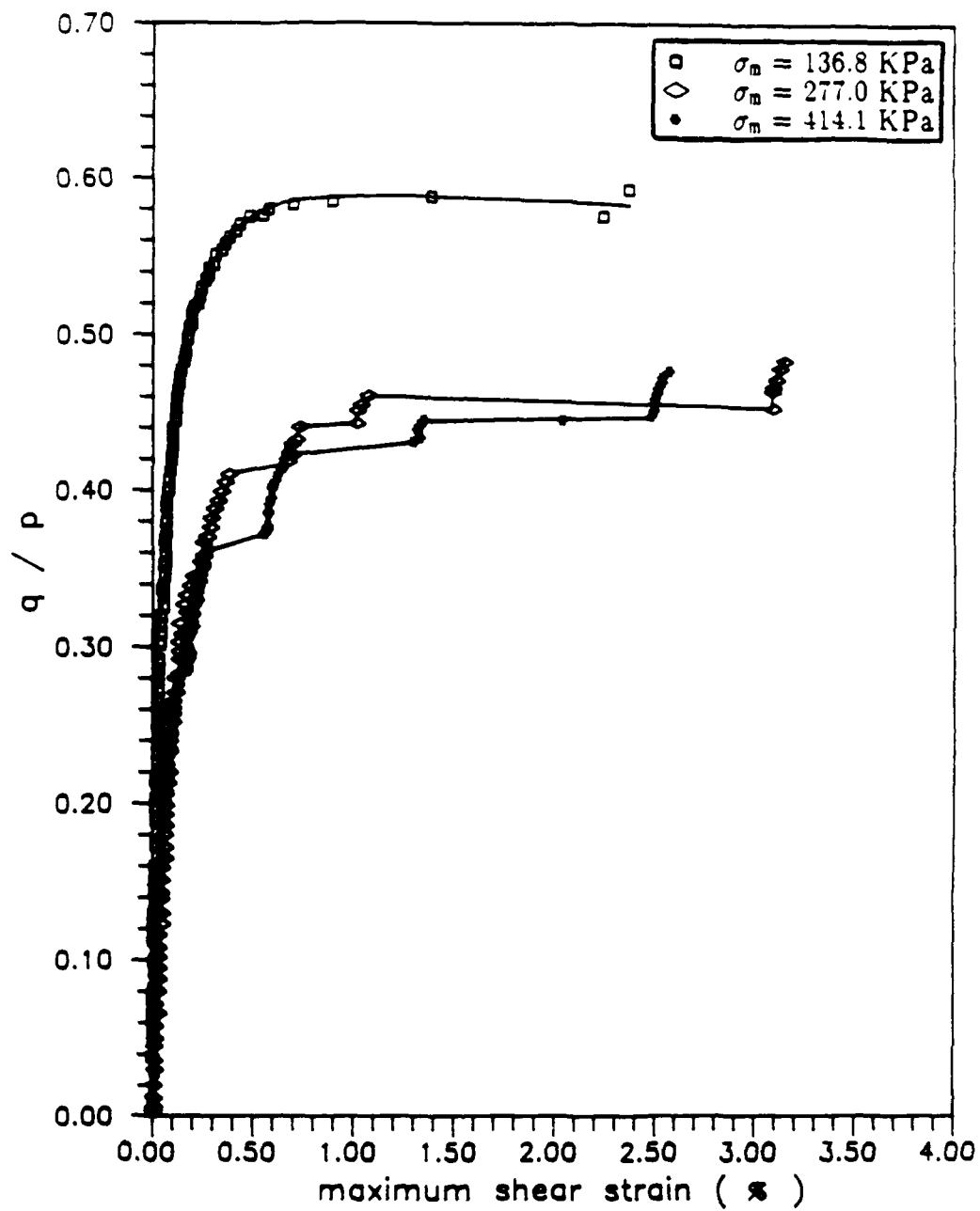


Figure 50.  $q/p$  Ratio versus Maximum Shear Strain for Monotonic Radial Shear Tests Having  $\theta = 0^\circ$ .

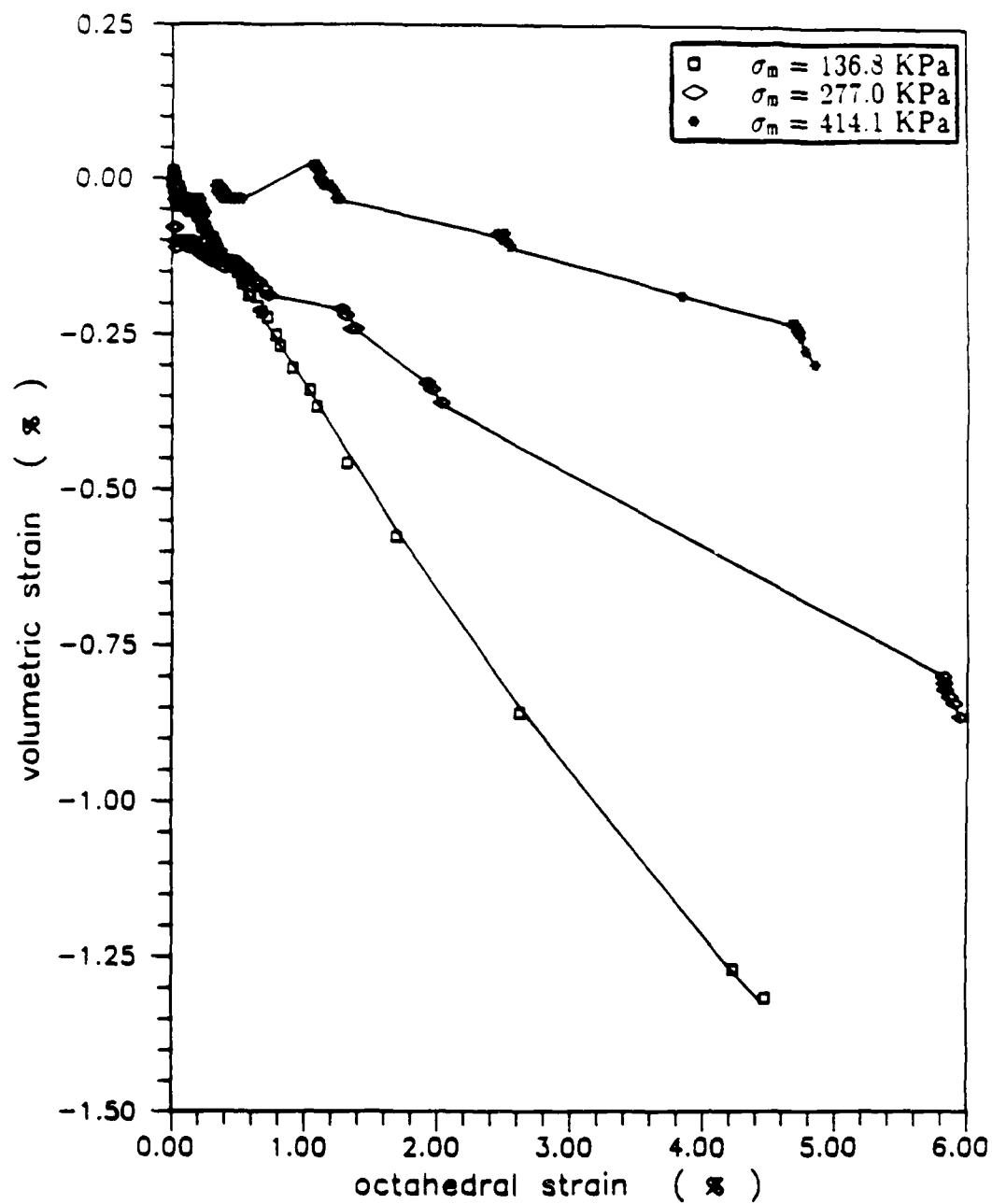


Figure 51. Volumetric Strain versus Octahedral Shear Strain from Monotonic Radial Shear Tests ( $\theta = 0^\circ$ ) on Mixtures of Different Sizes of Glass Beads Consolidated at Different Confining Stresses.

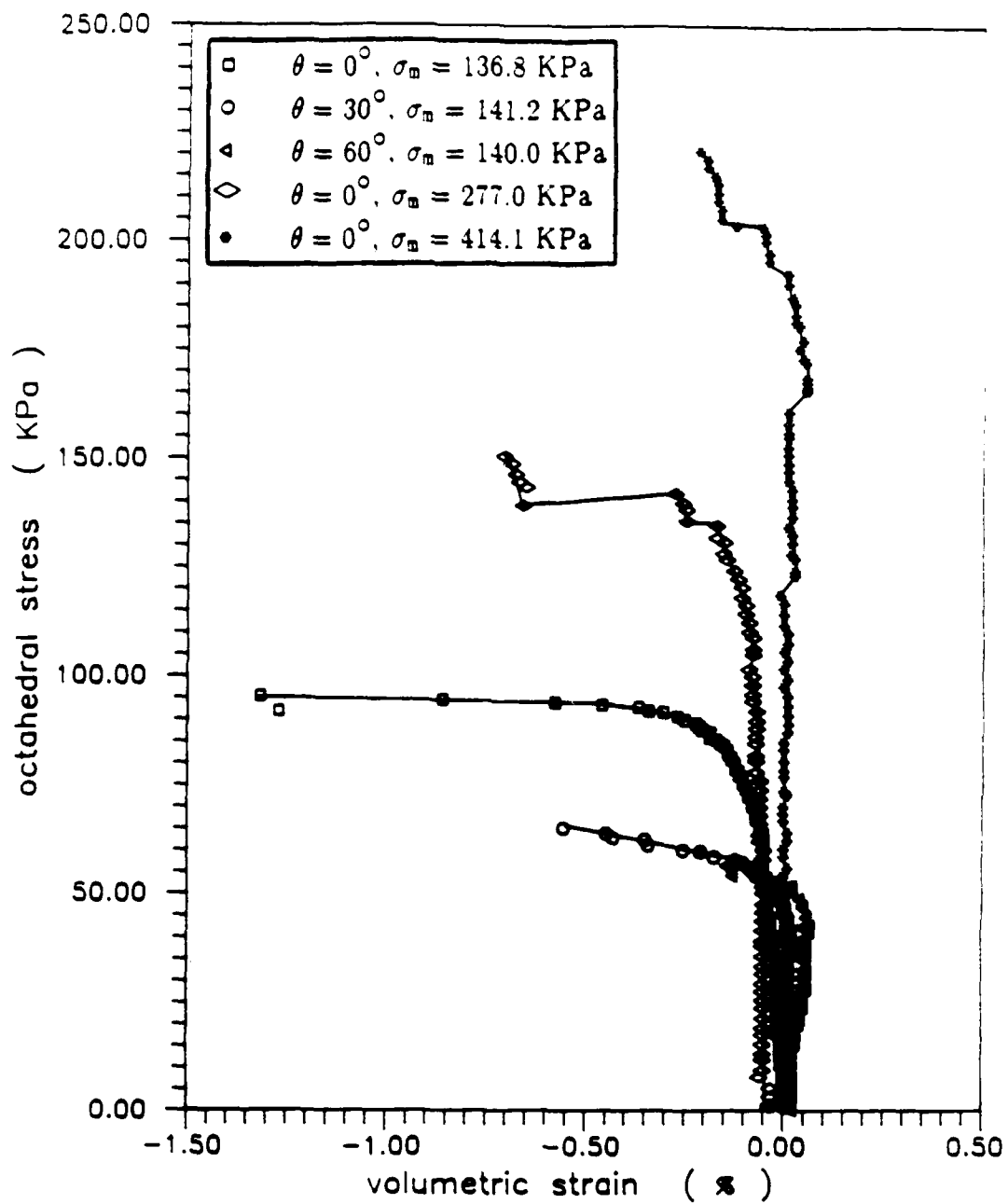


Figure 52. Octahedral Stress versus Volumetric Strain for Monotonic Radial Shear Tests on Assemblies of Different Sizes of Spherical Particles.

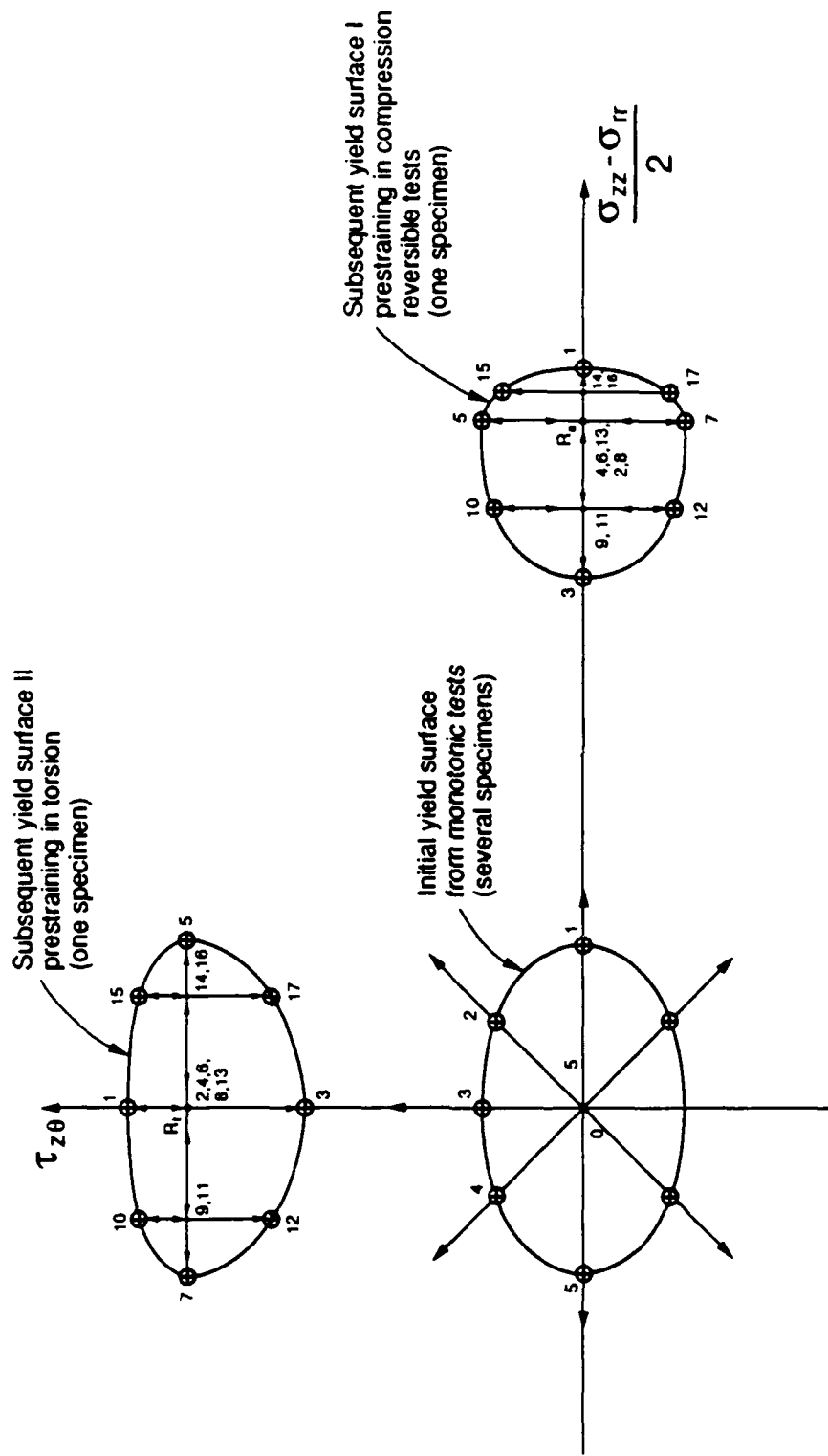


Figure 53. Sequences of Loading for the Determination of the "initial" and "subsequent" Yield Surfaces.

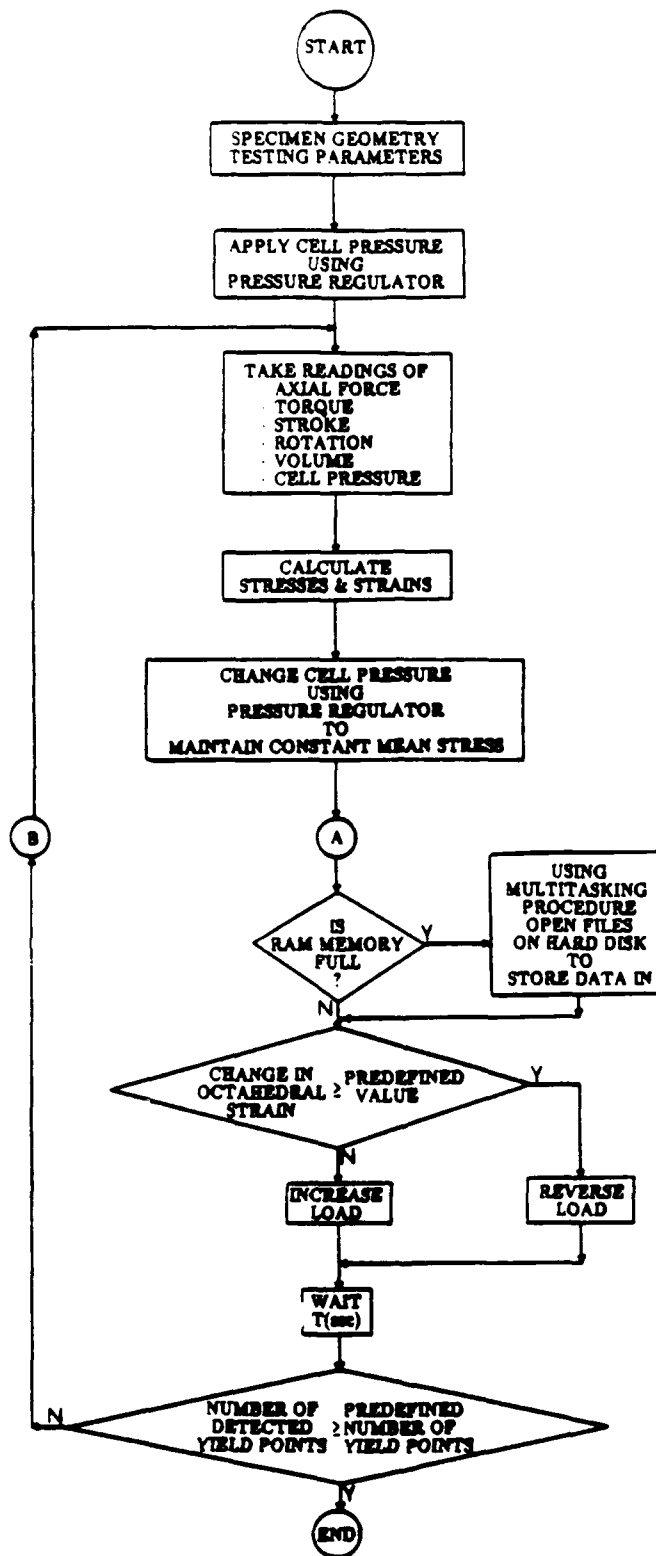


Figure 54. Flowchart of the program controlling the experiments.

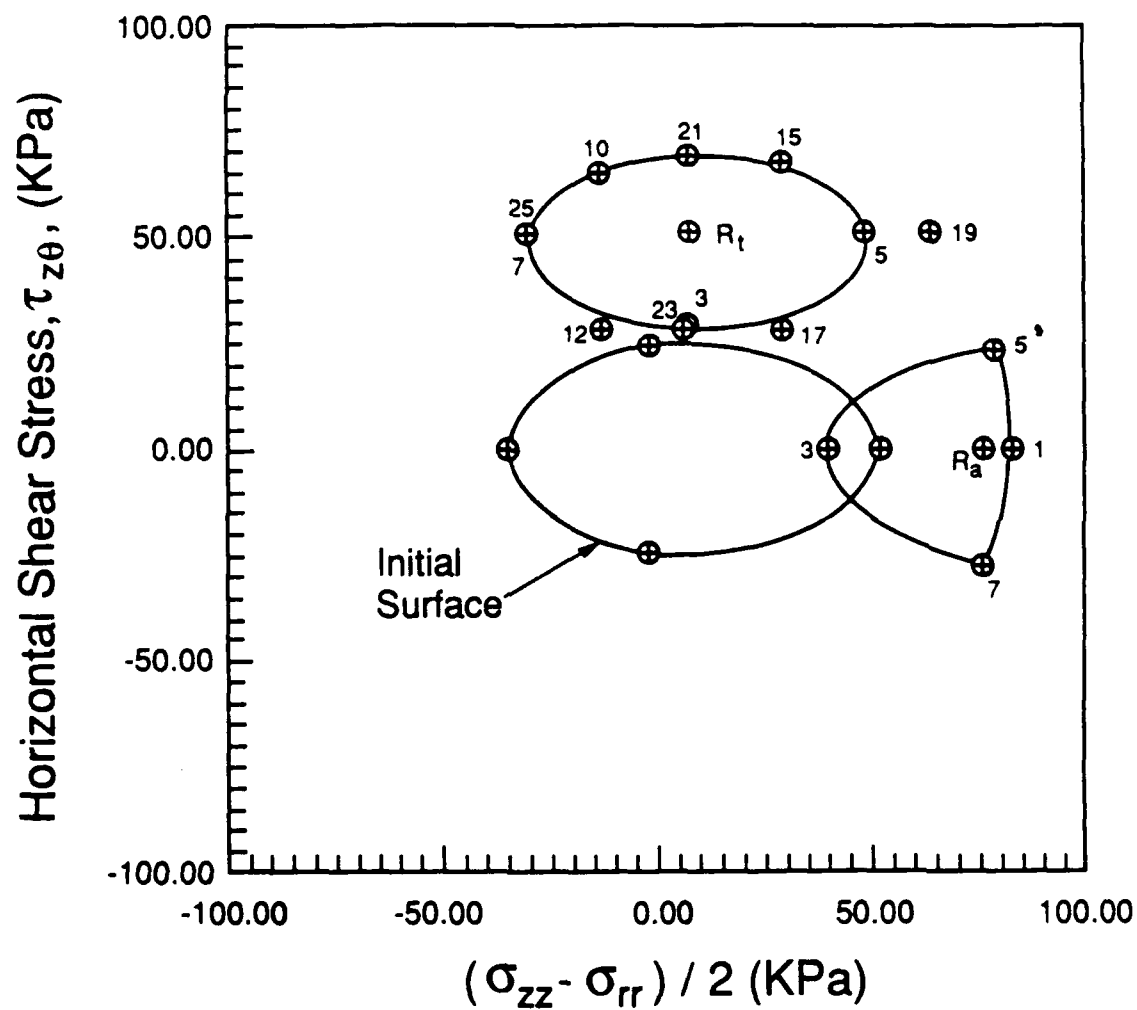


Figure 55. Experimentally Obtained Initial and Subsequent Yield Surfaces in Glass Beads ( $\gamma_{oct} = 0.1\%$ ).

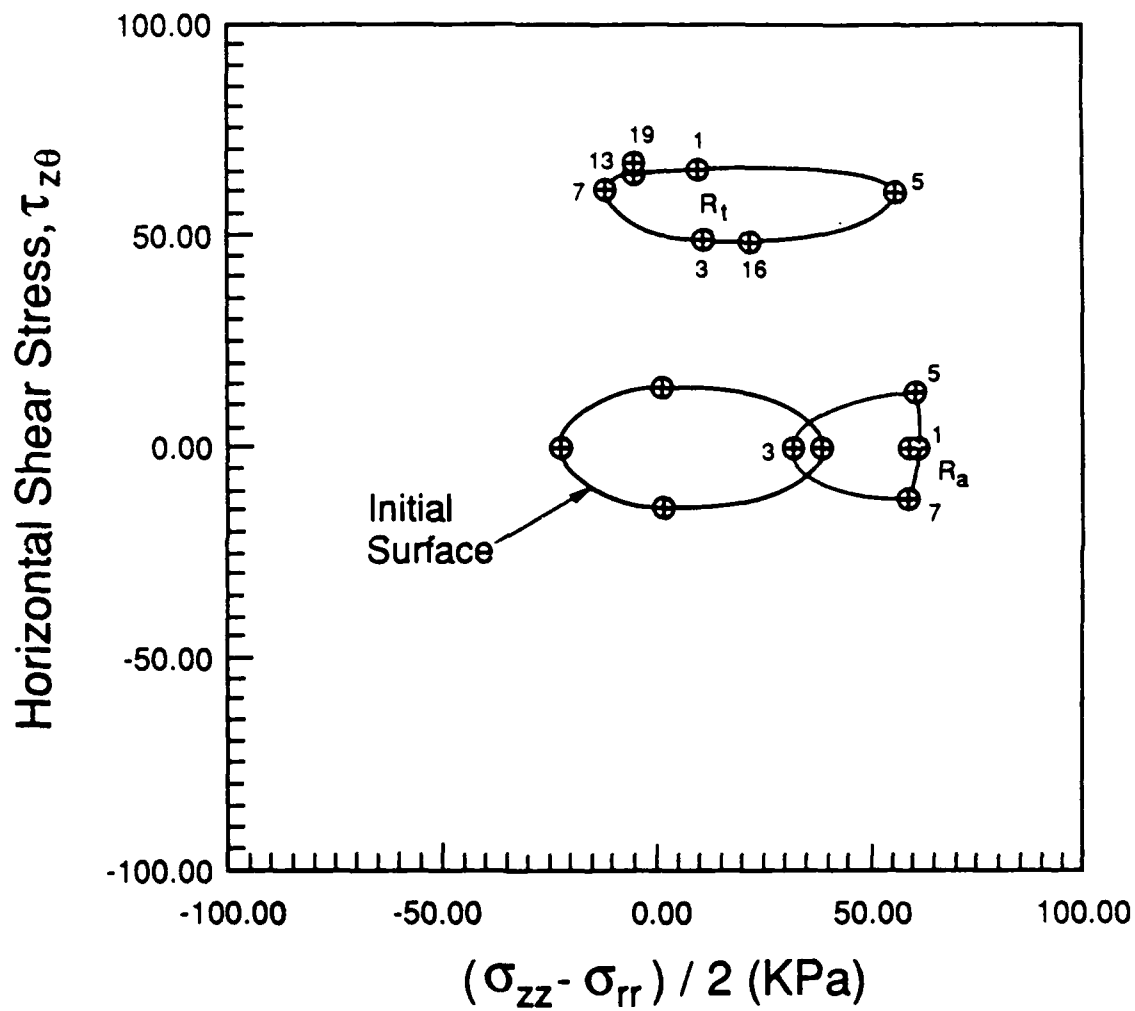


Figure 56. Experimentally Obtained Initial and Subsequent Yield Surfaces in Glass Beads ( $\gamma_{oct} = 0.05\%$ ).

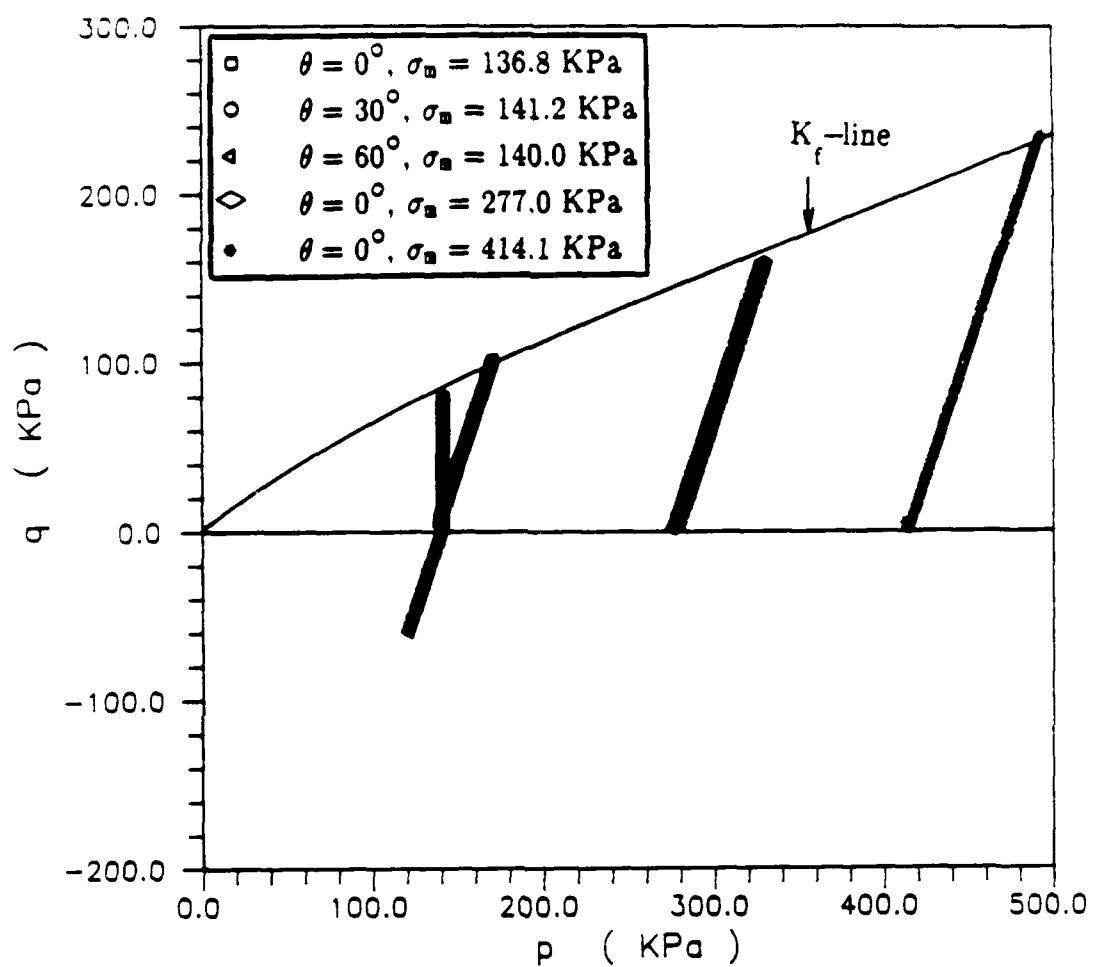


Figure 57. Stress Paths from Monotonic Radial Shear Tests on Glass Beads Plotted on p-q Diagram.



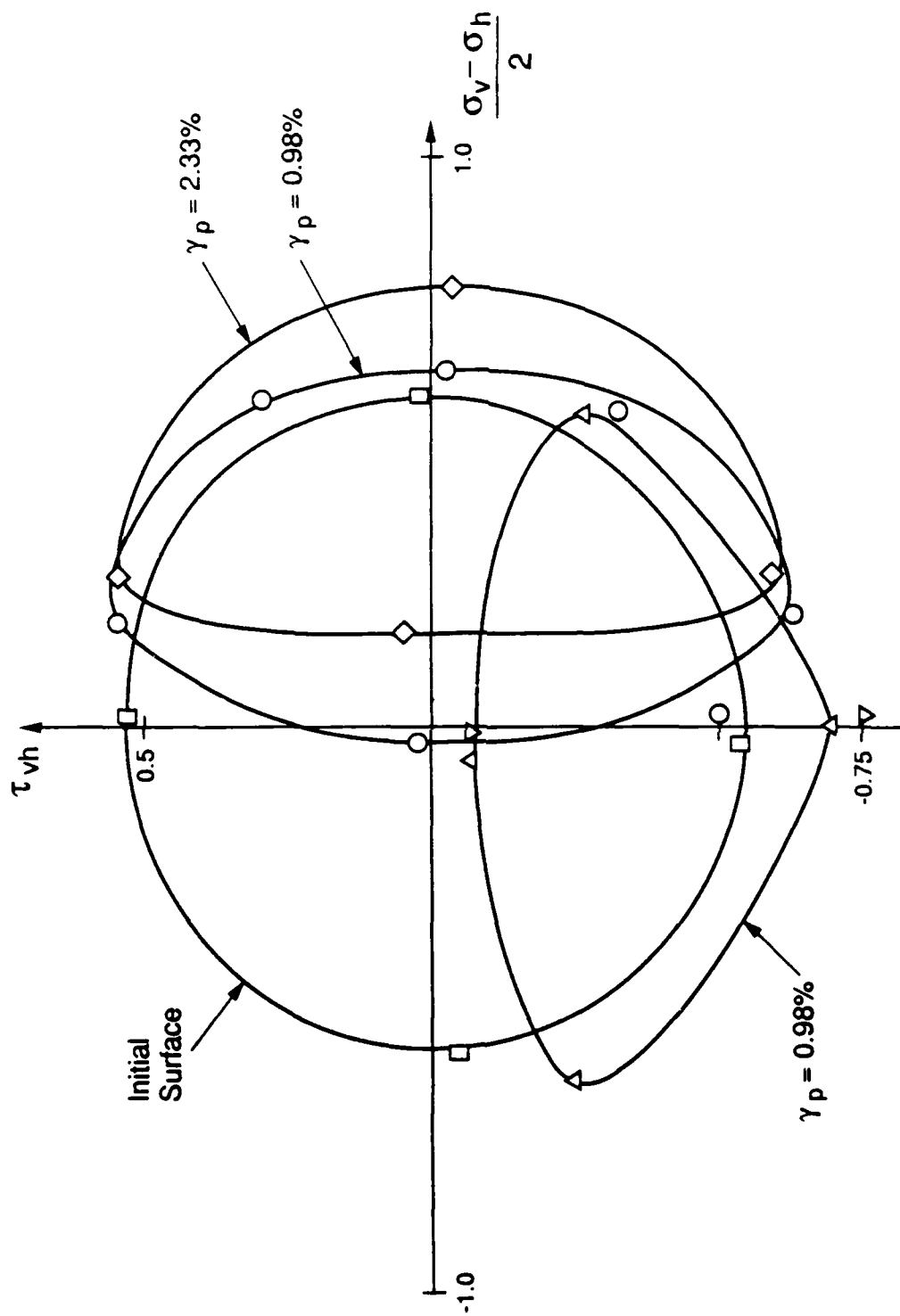


Figure 58. Initial and Subsequent yield surfaces of the 531-Sphere Medium in the  $\tau_{vh}$   $\frac{1}{2}(\sigma_v - \sigma_h)$  Space calculated Using Distinct Element Program CONBAL-2. Yield Surfaces Defined as the Set of all Points with  $\gamma_{oct} = 0.05\%$ .

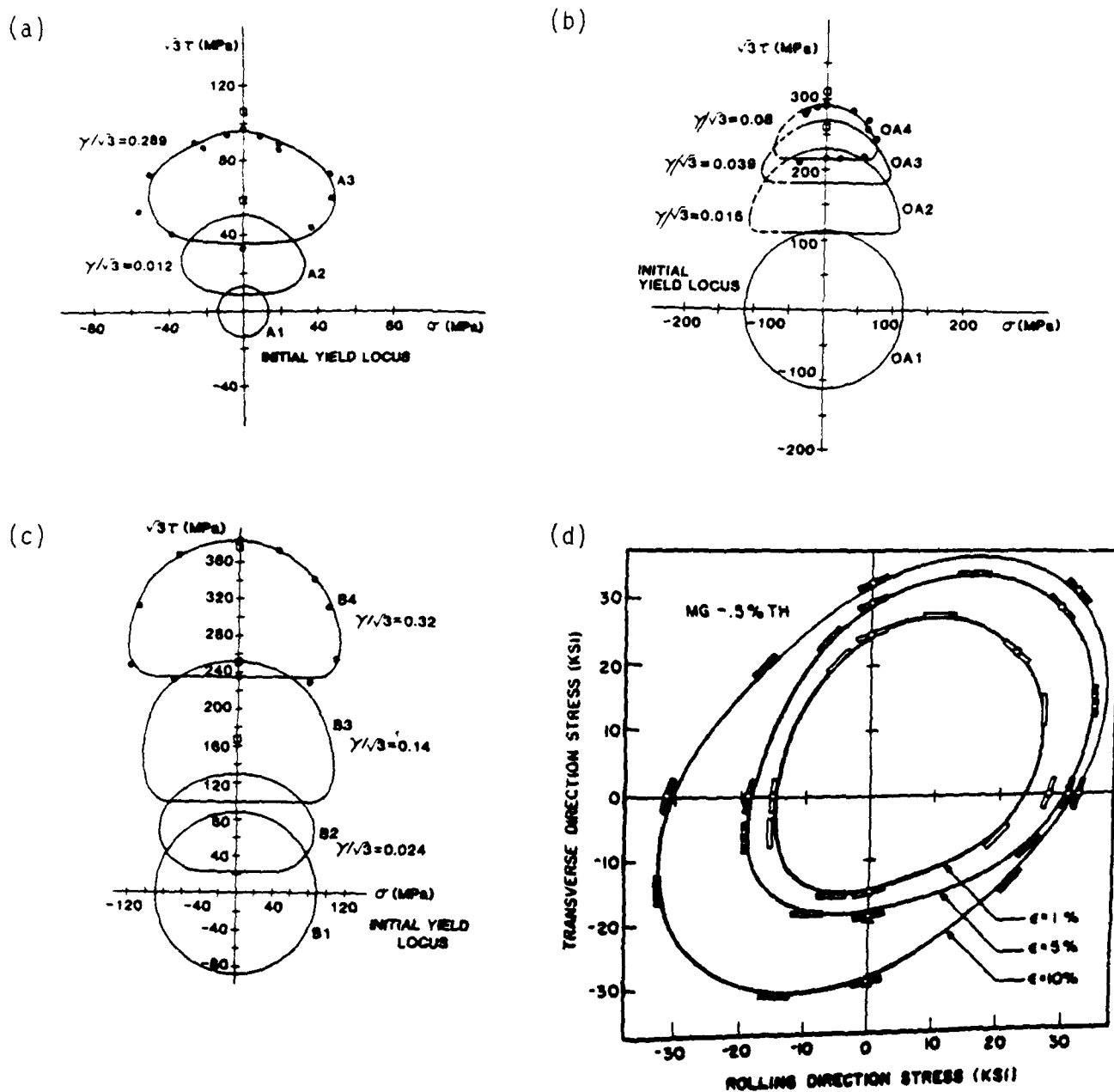


Figure 59. Experimentally Obtained Yield Loci for Engineering Materials after Shear Prestrain (a) 1100-0 Aluminum, (b) Overaged 2024-T7 Aluminum Alloy (Helling et al. 1986), (c) 70:30 Brass, and (d) Textured Magnesium (Kelley and Hosford 1968).

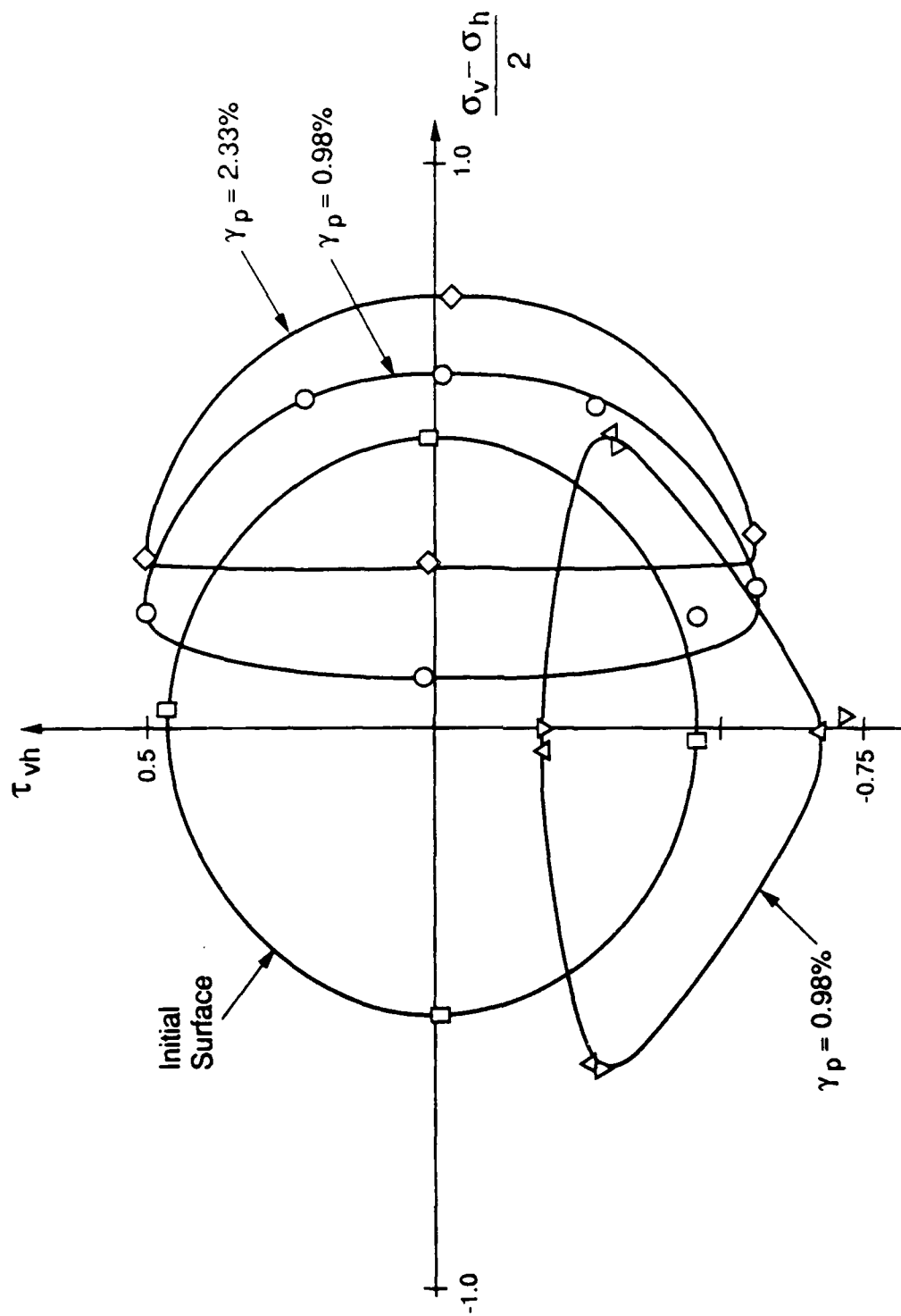


Figure 60. Initial and Subsequent Yield Surfaces of the 531-Sphere Medium in the  $\tau_{vh}$   $1/2 (\sigma_v - \sigma_h)$  Space calculated Using Distinct Element Program CONBAL-2. Yield Surfaces Defined as the Locus of all Points with  $\gamma_{oct} = 0.05\%$ .

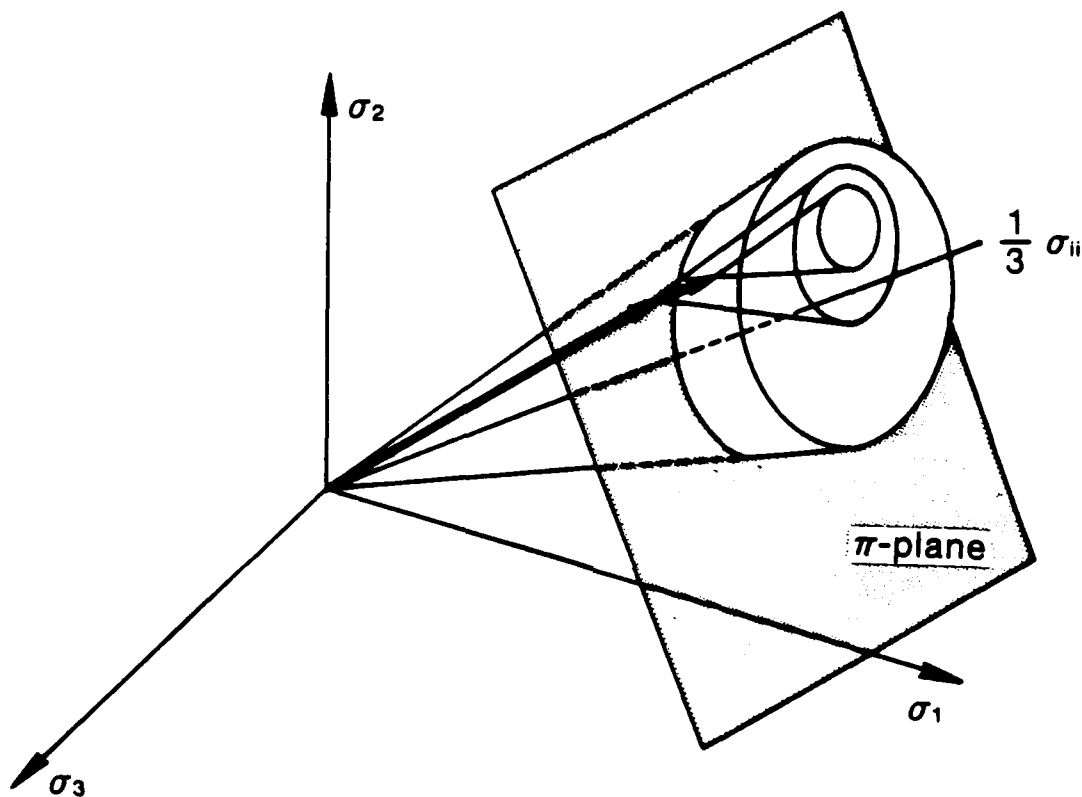


Figure 61. Conical Yield Surfaces and Current  $\pi$ -plane for Constitutive Law of Granular Soil of Eqs. 1-7. Position of Yield Cones Correspond to Loading from O to A followed by Stress increment AB. Point B is on the  $\pi$ -plane. The Value of  $p$  at the Apex of Any Cone (e.g., A, B) is  $p_i$ .

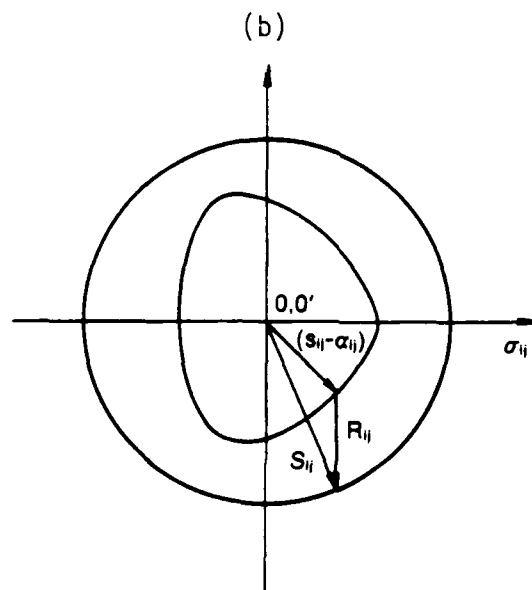
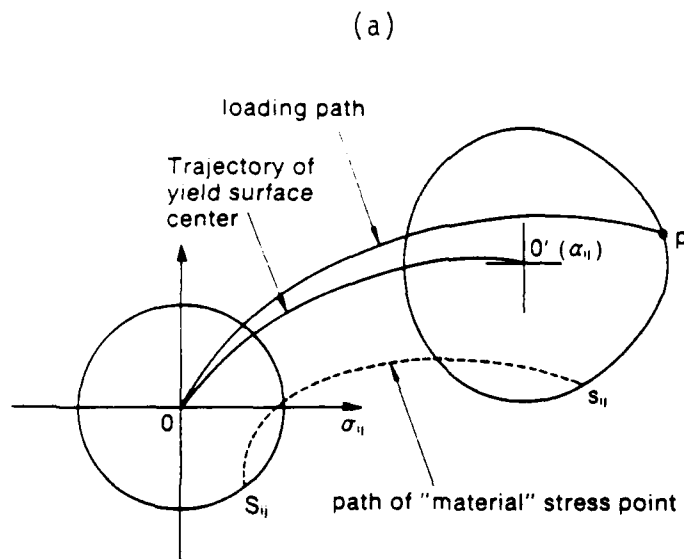


Figure 62. Schematic Representation of (a) Translation and (b) Distortion of a Yield Surface (Yen 1979).

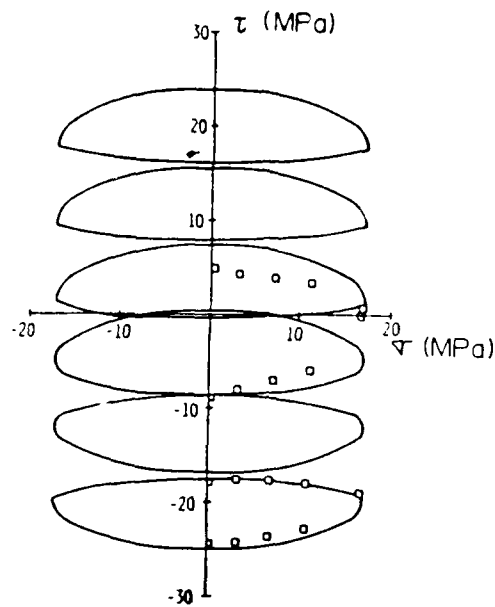


Figure 63. Predicted and Measured Yield Surfaces in Aluminum (Yen and Eisenberg 1987).

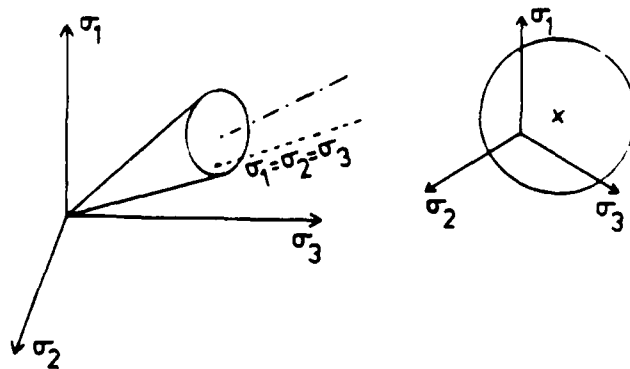


Figure 64. Yield Surface in principal Stress Space. Note the Rotation of the Surface Around its Apex (Prevost 1985).

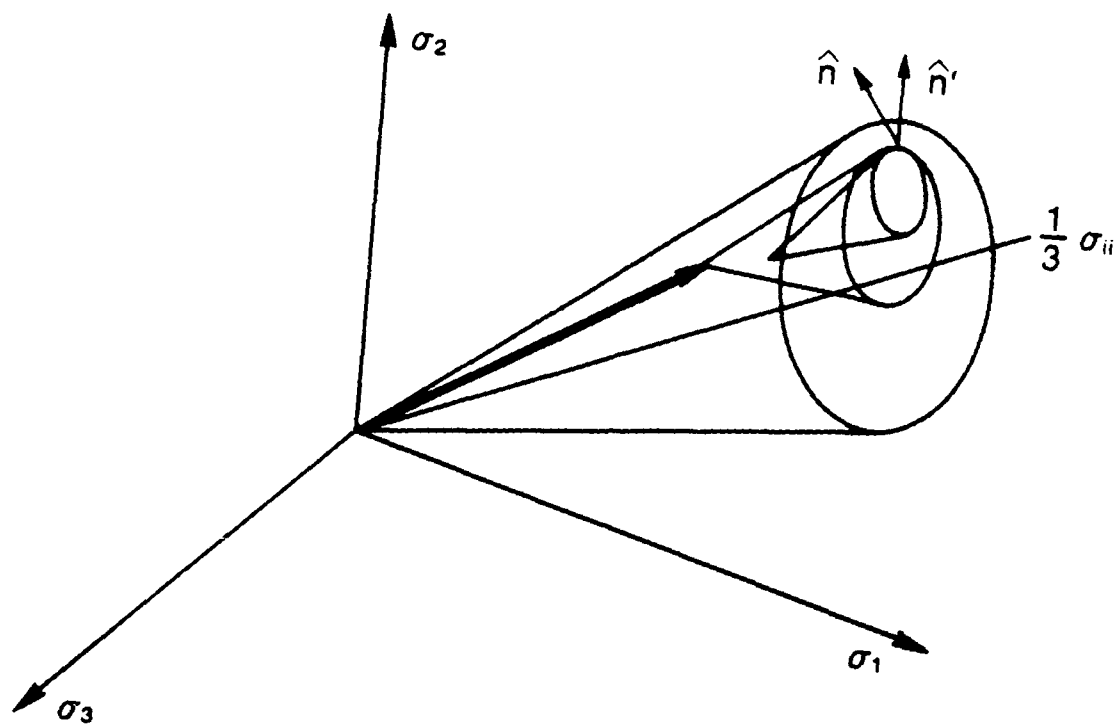


Figure 65. Proposed Modification of the Hardening Rule to Allow Limited Rotation Around the Yield Surface Apex in Order to Account for Dilation.